IoT Transmission Technologies for Distributed Measurement Systems in Critical Environments

Giacomo Peruzzi

Ph. D. Thesis

University of Siena

IoT Transmission Technologies for Distributed Measurement Systems in Critical Environments

Giacomo Peruzzi

Advisor: Prof. Ada Fort
Co-Advisor: Prof. Alessandro Pozzebon

PhD Thesis

UNIVERSITY OF SIENA
DEPARTMENT OF INFORMATION ENGINEERING AND MATHEMATICS

PhD PROGRAM IN INFORMATION ENGINEERING AND SCIENCE

XXXV CYCLE

Disciplinary Scientific Sector ING-INF/07

IoT Transmission Technologies for Distributed Measurement Systems in Critical Environments

Giacomo Peruzzi,

June, 2023.

A digital version of the thesis can be available upon request from the Author:
peruzzi@diism.unisi.it.

Contents

List of Figures

List of Tables

List of Acronyms

16-QAM 16 Quadrature Amplitude Modulation.

3GPP 3^{rd} Generation Partnership Project.

AG2UG Aboveground-to-Underground.

AI Artificial Intelligence.

ALOHA Additive Links On-line Hawaii Area.

API Application Program Interface.

ASK Amplitude Shift Keying.

AW2UW Abovewater-to-Underwater.

BD Bulk Density.

BPSK Binary Phase-Shift Keying.

CR Coding Rate.

CSS Chirp Spread Spectrum.

D-BPSK Differential BPSK.

EC-GSM-IoT Extended Coverage Global System for Mobile IoT.

eDRX Extended Discontinuous Reception.

eNodeB evolved Node B.

FDMA Frequency Division Multiple Access.

FEC Forward Error Correction.

GFSK Gaussian Frequency Shift Keying.

GMSK Gaussian Minimum Shift Keying.

GPRS General Packet Radio Service.

GPS Global Positioning System.

GSM Global System for Mobile.

IIoT Industrial Internet of Things.

IoT Internet of Things.

IoUT Internet of Underground Things.

ISM Industrial, Scientific and Medical.

ITU International Telecommunication Union.

JPEG Joint Photographic Experts Group.

LEO Low Earth Orbit.

LoRa Long Range.

LoRaWAN LoRa Wide Area Network.

LoS Line of Sight.

LPWAN Low Power Wide Area Network.

LTE Long Term Evolution.

LTE-M LTE Machine Type Communication.

M2M Machine to Machine.

MAC Media Access Control.

MBSDM Mineralogy-Based Soil Dielectric Model.

ML Machine Learning.

MQTT Message Queue Telemetry Transport.

NB-IoT Narrow Band IoT.

OFDMA Orthogonal FDMA.

OMS Open Metering Systems.

OQPSK Offset Quadrature Phase-Shift Keying.

PCB Printed Circuit Board.

PL Packet Loss.

PMF Probability Mass Function.

PRB Physical Resource Block.

PSK Phase-Shift Keying.

QoS Quality of Service.

QPSK Quadrature Phase-Shift Keying.

RFTDMA Random Frequency and TDMA.

RPMA Random Phase Multiple Access.

RRC Radio Resource Control.

RSSI Received Signal Strength Indicator.

SC-FDMA Single Carrier FDMA.

SE Shielding Effectiveness.

SF Spreading Factor.

SG Specific Gravity.

SMA SubMiniature version A.

SNR Signal-to-Noise Ratio.

SPI Serial Peripheral Interface.

TDMA Time Division Multiple Access.

ToA Time on Air.

TSMA Telegram Splitting Multiple Access.

UG2AG Underground-to-Aboveground.

UG2UG Underground-to-Underground.

USART Universal Synchronous and Asynchronous Receiver-Transmitter.

UW2AW Underwater-to-Abovewater.

UW2UW Underwater-to-Underwater.

VSU Video Surveillance Unit.

VWC Volumetric Water Content.

WSN Wireless Sensor Network.

WUSN Wireless Underground Sensor Network.

Introduction

Distributed measurement systems are spread in the most diverse application scenarios, and Internet of Things (IoT) transmission equipment is usually the enabling technologies for such measurement systems that need to feature wireless connectivity to ensure pervasiveness. Because wireless measurement systems have been deployed for the last years even in critical environments, assessing transmission technologies performances in such contexts is fundamental. Indeed, they are the most challenging ones for wireless data transmission due to their intrinsic attenuation capabilities.

In particular, several scenarios in which measurement systems can be deployed will be analysed in detail. Firstly, marine contexts will be treated by taking into account above-the-sea wireless links. Such setting can be experienced in whichever application requiring remote monitoring of facilities and assets that are offshore installed. Some instances are offshore sea farming plants, or remote video monitoring systems installed on seamark buoys. Secondly, wireless communications taking place from the underground to the aboveground will be covered. This scenario is typical of precision agriculture applications, where the accurate measurement of underground physical parameters is needed to be remotely sent so to optimise crops and yields reducing the wastefulness of fundamental resources (e.g., irrigation water). Thirdly, wireless communications occurring from the underwater to the abovewater will be addressed. For example, such situation is inevitable for all those infrastructures monitoring conservation status of underwater species like algae, seaweeds and reef. Then, wireless links happening traversing metal surfaces and structures will be tackled. Specifically, such context is commonly encountered in asset tracking and monitoring (e.g., containers), or in smart metering applications (e.g., utility meters). Lastly, sundry harsh environments that are typical of industrial monitoring (e.g., vibrating machineries, harsh temperature and humidity rooms, corrosive atmospheres) will be tested to validate pervasive measurement infrastructures even in such

contexts that are usually experienced in Industrial Internet of Things (IIoT) applications. The performances of wireless measurement systems in such scenarios will be tested by sorting out ad-hoc measurement campaigns. Finally, IoT measurement infrastructures respectively deployed in above-the-sea and underground-to-aboveground settings will be described so to provide real applications in which such facilities can be effectively installed. Nonetheless, the aforementioned application scenarios are only some amid their sundry variety. Indeed, nowadays distributed pervasive measurement systems have to be thought in a broad way, resulting in countless instances: predictive maintenance, smart healthcare, smart cities, environmental monitoring, industrial monitoring, or smart agriculture.

This Thesis aims at showing distributed measurement systems in critical environments so to set up pervasive monitoring infrastructures that are enabled by IoT transmission technologies. At first, they are presented, and then the harsh environments are introduced, along with the relative theoretical analysis modelling path loss in such conditions. It must be underlined that this Thesis aims neither at finding better path loss models with respect to the existing ones, nor at improving them. Indeed, path loss models are exploited as they are, in order to derive estimates of losses so to understand the effectiveness of the deployed infrastructure. In fact, some transmission tests in those contexts are described, along with providing examples of these types of applications in the field, showing the measurement infrastructures and the relative critical environments serving as deployment sites. The scientific relevance of this Thesis is evident since, at the moment, the literature lacks a comparative study like this, showing both transmission performances in critical environments, and the deployment of real IoT distributed wireless measurement systems in such contexts.

This Thesis is drawn up as follows. Chapter 1 reviews the most adopted IoT transmission technologies for pervasive measurement systems. Chapter 2 shows the general adopted methodology for measuring performances related to the tests described throughout the whole dissertation. Chapters 3, 4, 5, 6, and 7 respectively report tests and results, along with the relative path loss model (if any), set up in turn in above-the-sea environments, underground-to-aboveground links, underwater-to-abovewater links, through-metal links, and in industrial harsh environments. Chapter 8 presents examples of IoT measurement infrastructures deployed in above-the-sea and underground-to-aboveground settings. Finally, Chapter 9 highlights conclusions and summarises the most relevant results.

For the sake of readability, and with the aim of helping the reader in mapping the topics of this Thesis, Figure 1 shows the Thesis graphical abstract.

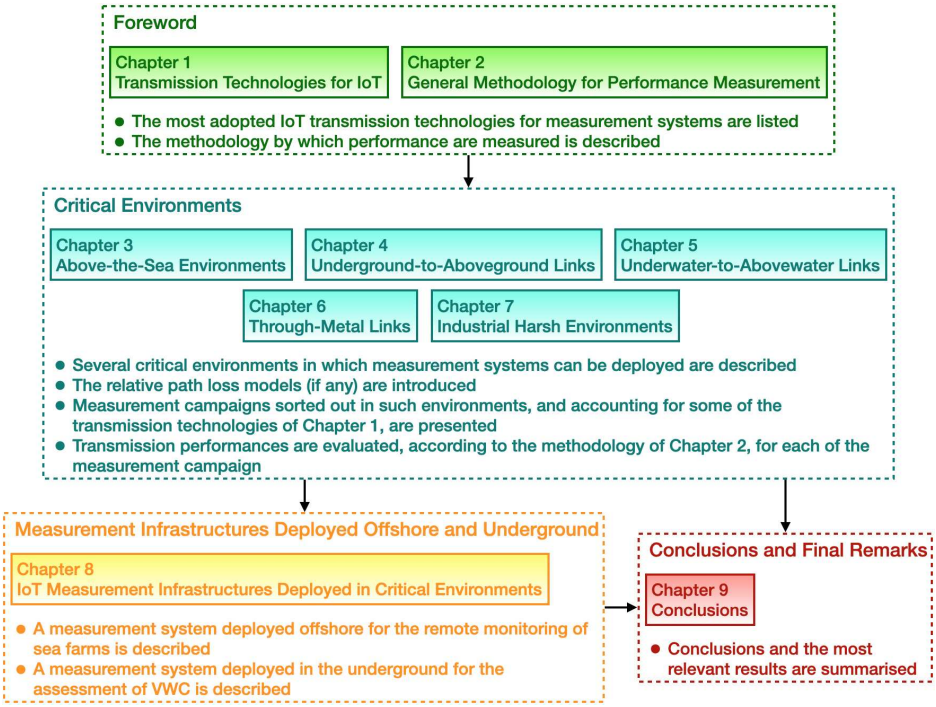

Figure 1: Thesis graphical abstract.

Chapter 1

Transmission Technologies for IoT

Distributed measurement systems for pervasive remote monitoring infrastructures require to set Wireless Sensor Networks (WSNs) whose nodes are properly enabled with connectivity. Moreover, whenever harsh environments are considered, such feature needs to be as low-power as possible so to extend the nodes battery lifetime, especially whenever energy harvesting systems are concerned [1, 2]. Indeed, the critical nature of the deployment sites implicitly entails that maintenance, and human interventions in general, is hardly feasible, or nearly impossible. In light of this, sensor nodes must be equipped with transceivers exploiting modulations and protocols belonging to the so-called Low Power Wide Area Network (LPWAN), at least in most of the times. The big picture of IoT currently proposes several LPWAN communication technologies, that can be broadly divided into three categories: cellular, meaning that they exploit licensed frequency bands to transmit; non-cellular, meaning that they exploit unlicensed frequency bands to transmit, usually belonging to the Industrial, Scientific and Medical (ISM) bands; and satellite, meaning that they transmit data towards satellites, usually Low Earth Orbit (LEO) ones, orbiting around the Earth that serve as data forwarders to the closest ground station.

The technologies making use of the spectrum belonging to the unlicensed ISM bands have carrier frequencies which are regional depending, implying that hardware devices must be thoroughly chosen bearing in mind the place in which the network will be deployed. Moreover, for such technologies some of the standards are free whilst some may require subscription fees. For instance, cellular technologies entail the subscription of data plans, meaning that running costs related to the deployment of a distributed measurement system inevitably raise, especially if wireless sensor nodes are given such connectivity. Finally, satellite IoT has been experiencing a big momentum, in spite of the fact that such technology is at its early days, and many solutions and applications are currently being developed. Although coverage and ubiquitous connectivity are ensured, satellite technologies still have the major drawback of costs for both the hardware, the network infrastructure, and the data plan, hinting at the fact that there is still room for improvement. Concerning network infrastructures, cellular standards offer these facilities to users, while only some of the non-cellular ones do. Indeed, most of the

Table 1.1: Summary of the IoT transmission technologies described in Chapter 1.

Cellular	Non-Cellular	Satellite
LTE-M	Sigfox	Lacuna
NB-IoT	Ingenu	Fossa
EC-GSM-IoT	Weightless	Astrocast
	LoRa/LoRaWAN	Swarm
	MIoTy	

times, developers must account for the network infrastructures (e.g., gateways, back-end servers, cloud frameworks, etc.) whenever non-cellular standards are adopted. Last but not least, power consumption must be analysed owing to the fact sensor nodes are generally installed in a deploy-and-forget fashion due to the harsh environments they are placed in. As anticipated, satellite IoT standards are the most energy demanding because transmissions have to cover hundreds of km in order to reach the satellites. Then, the majority of cellular technologies are considerably energy hungry because of synchronisation and network joining phases prior to transmissions that nodes must accomplish. However, some account for simplified paging procedures. For instance, Narrow Band IoT (NB-IoT) foresees the Extended Discontinuous Reception (eDRX) mode, which allows transceivers to enter in deep sleep between paging temporal windows, thus optimising power consumption. On the other hand, the bulk of non-cellular standards is low-power, thanks to the reduced overhead during transmissions and to the fact that some of them access the media according to the Additive Links On-line Hawaii Area (ALOHA) method. Eventually, Table 1.1 summarises the IoT transmission technologies introduced in this Chapter, where the listed cellular technologies are the only ones falling in the field of interest of this Thesis, meaning that Table 1.1 is not fully exhaustive.

1.1 Cellular Technologies

These technologies were developed exploiting the existing cellular standards upon which they rely on. For this reason, they inherit their principal characteristics such as bandwidth and coverage range. As it was said, due to the fact that they transmit by making use of licensed bands, it is necessary to pay a subscription thus encumbering on running costs. All of the cellular technologies were released by the 3^{rd} Generation Partnership Project (3GPP). A list of the principal cellular IoT technologies is given below, while they can be compared in Table 1.2 [3, 4, 5, 6].

Table 1.2: IoT cellular technologies comparison.

	LTE-M	**NB-IoT**	**EC-GSM-IoT**
Frequency Band	LTE bands	LTE subset bands	GPRS bands
Data-rate	$1 - 7$ Mbps	250 kbps	$70 - 240$ kbps
Channel Bandwidth	$1 - 5$ MHz	180 kHz	200 kHz
Message Payload	≤ 256 B	≤ 1600 B	Not known
Coverage Range	Same as LTE	$\simeq 1$ km (urban) $\simeq 10$ km (rural)	Same as GPRS

1.1.1 LTE-M

LTE Machine Type Communication (LTE-M) operates, focusing on Machine to Machine (M2M) communication and IoT, by using the cellular Long Term Evolution (LTE) standard. Hence, it is fully compatible with actual cellular networks because it is directly derived by standard LTE. Indeed, telecom companies do not necessitate any additional device to be installed since they just have to update the firmware running on their base stations to the newer versions. Because of this, there exist some telecom providers that have already started activating such services making some experiments. For instance, in Canada a monitoring system for vineyards based on LTE-M has been set up for some years [7]. Some other application scenarios in which measurement infrastructures are enabled by LTE-M are air quality monitoring [8], high speed railways monitoring [9] or oceanic wave height measurement [10]. In comparison with standard LTE, it offers optimised sleep modes from the point of view of consumption resulting in higher power budgets. Amid the cellular LPWAN technologies, LTE-M has the highest data-rate. However, it requires the broader channel band. It exploits the 16 Quadrature Amplitude Modulation (16-QAM) and, for what concerns the channel access, it makes use of two methods stemming from the Frequency Division Multiple Access (FDMA): Single Carrier FDMA (SC-FDMA) for uplinks and Orthogonal FDMA (OFDMA) for downlinks.

1.1.2 NB-IoT

NB-IoT was released by the 3GPP within release 13 so to provide a standard for massive IoT contexts. Notwithstanding that NB-IoT and LTE-M come from the same organisation, they differ for several aspects. First of all, NB-IoT has lower data-rate and narrower bandwidth than LTE-M. Secondly, NB-IoT does not necessarily work within LTE bands: it is designed to operate in a subset of LTE bands or even in the unexploited Global System for Mobile (GSM) bands. Even though it has lagged behind LTE-M, more

and more telecom firms are investing on it at the moment. It has been notably used especially in Europe where it is finding its application scenarios (e.g., asset tracking). NB-IoT standard specifications aver that it requires less power than LTE-M. This is a double-edged sword though: low-power features are always a good characteristic wherever sensor nodes relying on batteries are employed, but it also means having a worse penetration capability through obstacles. Concerning the physical layer, it may exploit both the Quadrature Phase-Shift Keying (QPSK) modulation and the Binary Phase-Shift Keying (BPSK) modulation [11]. For what matters the methods for accessing the channel, it shares all of them with LTE-M. In particular, channel access is implemented by scheduling techniques upon Physical Resource Blocks (PRBs) [12]: it is made of twelve 15 kHz sub-carriers of 7 temporal symbols. Specifically, two medium access methods are exploited: SC-FDMA for uplinks and OFDMA for downlinks. NB-IoT operates within licensed bands: particularly in Italy, such bands are the twenty (i.e., 860 MHz) and the eight (i.e., 900 MHz). Owing to the legacy from LTE, NB-IoT makes use of LTE base stations, which are named evolved Node B (eNodeB), operating according to three different functioning schema [13]: standalone, resulting in a bandwidth of 200 kHz; within LTE band, occupying a bandwidth of 180 kHz; within LTE guard band, requiring a bandwidth of 180 kHz. NB-IoT has a complex protocol architecture which comprises a user plane and a control plan, each of which has its own protocol stack and logic entities. In particular, the control plan plays a fundamental role controlling the connection between the end devices and the eNodeB implementing either the Radio Resource Control (RRC) protocol and the handover. Some instances of application scenarios in which measurement infrastructures are enabled by NB-IoT are asset tracking [14], Wireless Underground Sensor Network (WUSN) [15] and water metering systems [16] in precision agriculture contexts, brine level measurement systems [17], soil moisture measurement infrastructures [18].

1.1.3 EC-GSM-IoT

Extended Coverage Global System for Mobile IoT (EC-GSM-IoT) is an evolution of the General Packet Radio Service (GPRS) technology towards IoT. Unlike the previous standards, it operates within the GPRS spectrum having comparable data-rate and bandwidth with NB-IoT. EC-GSM-IoT could also run on GSM networks provided that the software implementing the protocol is upgraded to a GSM compatible version, due to the fact that both techonologies share most of the hardware. It exploits either the Gaussian Minimum Shift Keying (GMSK) and the 8-ary Phase-Shift Keying (PSK) modulations, and the Time Division Multiple Access (TDMA) and the FDMA methods to access the communication channel. Anyway, amidst the cellular techonologies, EC-GSM-IoT appears to be the one

having the least impulse, finding usage in massive IoT as an alternative to NB-IoT [19, 20, 21].

1.2 Non-Cellular Technologies

These technologies make use of the spectrum belonging to the unlicensed ISM bands. Each of them has its own modulation scheme and method for accessing the media. A list of the principal non-cellular IoT technologies is given below, while they can be compared in Table 1.3.

Table 1.3: IoT non-cellular technologies comparison.

	Sigfox	**Ingenu**	**Weightless**	**LoRa LoRaWAN**	**MIoTy**	**Wireless M-Bus**
Frequency Band	868 MHz (EU) 902 MHz (US) 920 MHz (AU)	2.4 GHz	Any sub-GHz ISM Band	433 MHz (CN) 868 MHz (EU) 915 MHz (US)	868 MHz (EU) 915 MHz (US)	169 MHz 433 MHz 868 MHz
Data-rate	100 bps	624 kbps 156 kbps	$20 - 100$ kbps	$0.3 - 50$ kbps	512 bps	2.4 kbps 19.2 kbps
Channel Bandwidth	100 Hz	1 MHz	12.5 kHz	125 kHz 250 kHz 500 kHz	200 kHz	12.5 kHz 50 kHz
Message Payload	$\leq$ 12 B	$\leq$ 10 kB	$\leq$ 48 B	$\leq$ 255 B	$\leq$ 192 B	$\leq$ 245 B
Coverage Range	$\simeq$ 40 km	$\simeq$ 45 km	$\simeq$ 2 km	$\simeq$ 5 km (urban) $\simeq$ 15 km (rural)	$\simeq$ 20 km	$\simeq$ 2 km

1.2.1 Sigfox

Sigfox is a French company founded more than 10 years ago and Sigfox networks are presently operating all over the world. Commonly with other IoT technologies, also Sigfox networks work within the sub-GHz spectrum, which is the set of all those operating frequencies less than 1 GHz. Users have to pay a subscription which offers different plans. The network topology is a star one enabling both uplinks and downlinks. Sigfox is characterised by a small size payload (i.e., maximum 12 B) that turns to be a major drawback, and a limited number of possible transmitting packets per day, depending on the subscription plan. Sigfox also offers a network infrastructure and a cloud service to retrieve, and possibly analyse, the transmitted data. In doing so, users have only to concern about the sensor nodes since all the network side is in charge of Sigfox itself. It operates within ISM bands, ranging from 868 MHz to 920 MHz depending on the region,

requiring very narrow band (i.e., only 100 Hz) and providing very low data-rates (i.e., only 100 bps). Sigfox takes advantage of the BPSK modulation and of the Random Frequency and TDMA (RFTDMA) to access the channel. Sigfox was exploited for measurement systems in the domains of asset tracking [22], environmental monitoring [23], or coastal water monitoring [24].

1.2.2 Ingenu

At its release, more than a decade ago, Ingenu was an innovative technology in the LPWAN scenery. It utilises ISM bands having higher frequencies than Sigfox. Indeed, it operates at 2.4 GHz that is the same frequency of WiFi or Bluetooth. The advantage of this band is that it is globally available as unlicensed one, so that developers do not have to consider in what regions their products will be deployed, differently from Sigfox. Moreover, 2.4 GHz band offers broader bandwidth than sub-GHz ISM bands. Along with the Differential BPSK (D-BPSK) modulation, the core of Ingenu LPWAN is its proprietary and patented technology: the Random Phase Multiple Access (RPMA). It is both a physical and Media Access Control (MAC) layer especially developed by Ingenu to satisfy the requirements of an LPWAN: extended battery lifetime, robustness towards interference, wide coverage and high capacity since a single LPWAN access point may cover up to 450 km^2 and may handle up to 530000 messages per hour. RPMA is also capable to address, among many other features, bi-directional communication and broadcast transmission. Ingenu has built the first wireless Machine Network: the largest IoT network in the world dedicated to connectivity for machines, that has been set up in more than 30 cities (most of them in the US). Moreover, similarly to Sigfox, Ingenu provides all the network infrastructure.

1.2.3 Weightless

Weightless comprises a set of wireless standards for LPWANs conceived for exchanging data between sensor nodes and base stations. It has been managed by the English Weightless Special Interest Group since 2012 [25]. At its early days, three standards were released (i.e., Weightless-P, Weightless-N, Weightless-W): two of them were deprecated in favour of the remaining one. Weightless-N provided only for uplinks, hence it was a mono-directional communication standard. Weightless-W was intended to operate within the unused frequencies belonging to the TV bands (i.e., $470 - 790$ MHz). Weightless-P is the only surviving standard, indeed it is simply named as Weightless, since it is bi-directional, it needs a narrow band to run and it exploits all the frequencies belonging to the ISM unlicensed sub-GHz bands (i.e., 169 MHz, 433 MHz, 470 MHz, 780 MHz,

868 MHz, 915 MHz and 923 MHz). In addition, Weightless is also an open standard that makes use of both the GMSK and the Offset Quadrature Phase-Shift Keying (OQPSK) modulations and of the TDMA to access the communication channel. Weightless is currently employed for smart parking systems [26]. Despite this, there seems to be a lack of hardware for implementing Weightless in order to be widely adopted by developers worldwide.

1.2.4 LoRa Modulation and LoRaWAN Protocol

Long Range (LoRa) modulation is a patented digital wireless communication standard developed in 2012 and owned by the American company Semtech. It is based on the Chirp Spread Spectrum (CSS) modulation and exploits the ALOHA method to access the communication channel (i.e., transmission may occur at any time). Nowadays it is managed and controlled by the LoRa Alliance [27] which is a consortium made up by over 500 companies dealing both with hardware and software. Such an institution also released the LoRa Wide Area Network (LoRaWAN) standard (i.e., a communication protocol referring to the MAC layer which is based onto the LoRa modulation). In contrast with the proprietary nature of the modulation from which Semtech receives royalties from chip vendors that sell LoRa modules, LoRaWAN specification is openly available. LoRaWAN is not the only network built on top of the LoRa modulation. Indeed, Link Labs has developed a competing LoRa based LPWAN called Symphony Link.

As its name hints, LoRa is a long range wireless communication technology that is able to reach coverage ranges up to few kilometers in urban areas and up to tens in rural environments. However, concerning this aspect, it has to be said that by achieving optimal trade-offs between the modulation parameters (e.g., data-rate or carrier frequency), very long transmission distances may be experienced proving high reliability and efficiency. It is the case of [28, 29] where some hundreds of kilometers were covered during particular tests. However, it has to be underlined that none of the referenced items are scientific works inasmuch they are only reports of those tests. Therefore, they are not fully validated from a scientific point of view.

Analogously as it is for other LPWAN techonologies, LoRa too is thought to be exploited in single-hop communications within star topology networks. Regardless of this fact, there exists a recent study that shows the feasibility of a multi-hop network by means of this modulation [30].

Unlike SigFox, users adopting this technique will have to account for additional networking components like gateways and servers. For both the network components, one could resort to either off-the-shelf solutions or to do-it-yourself solutions.

Measurement systems relying on LoRa modulation and LoRaWAN protocol are

countless. Indeed, LoRa is the most adopted enabling technology in the field of remote measurements due to its robustness towards interference, the long coverage range, and the low-cost of transceivers. Moreover, because of the open source paradigm of the LoRaWAN protocol, hybrid networks including more than such standard can be designed [31]. For the sake of completeness, some instances are reported ranging in the most diverse application scenarios: smart waste management systems in smart cities [32, 33, 34], vehicular networks [35, 36], video monitoring systems [37, 38], smart healthcare [39, 40], environmental monitoring [41, 42], industrial monitoring [43, 44], precision agriculture [45, 46], or smart metering [47, 48]. As it will be seen throughout this Thesis, LoRa modulation and LoRaWAN protocol are the most tested technologies. This choice was motivated owing to their boundless and massive usage. Therefore, it sounded reasonable to assess the relative performances in all of those scenarios in which robust and long range connectivity can find natural exploitation: harsh environments. Nonetheless, within suitable application scenarios other technologies were tested as well to provide comparisons.

1.2.5 MIoTy

MIoTy is one of the newest available LPWAN protocols operating in the sub-GHz ISM bands that was originally devised for industrial monitoring. MIoTy represents one of the most effective and robust wireless technologies in the market due to its method for accessing the media: the telegram splitting, or better known as Telegram Splitting Multiple Access (TSMA), which is a patented technology developed by Fraunhofer IIS. This technique splits the message into multiple sub-packets, to be transmitted several times (i.e., introducing redundancies) by resorting to both frequency diversity and time diversity schemes after having applied error correction codes, so to enhance robustness towards interference and limit data loss. Indeed, because of the shorter Time on Air (ToA) of the sub-packets with respect to other LPWANs, the probability of collision with other messages is extremely low, thus making MIoTy suitable to operate in crowded spectra like the one belonging to sub-GHz ISM bands. Moreover, the inability of recovering the full message at the receiver side is minimised thanks to TSMA allowing the loss of a considerable amount of sub-packets. MIoTy allows for a data-rate up to 512 bit/s, a maximum payload size of 192 B, and a coverage range up to 20 km. Moreover, it requires 200 kHz bandwidth for both uplinks and downlinks. An interesting feature is that it is designed so to support sensor nodes mobility, because it is capable of ensuring connection for moving transceivers up to 120 km/h. Likewise LoRaWAN, MIoTy is run by the MIoTy alliance [49], a consortium of hardware and software developers and designers. Finally, due to the fact it was only recently issued, the literature currently lacks of works dealing

with MIoTy enabling measurement systems.

1.2.6 Wireless M-Bus

The wireless M-Bus (Meter Bus) is a European standard for remote smart metering purposes released by the Open Metering Systems (OMS) group. Originally, it was issued as a standard for remote readout of heat meters, and then it was also exploited for measuring several utilities (e.g., water, gas). Then, in recent years, it was also exploited for enabling IoT infrastructures. The relative transceivers require low energy owning to the protocol entailing a limited overhead. Initially, transmissions could take place in 433 MHz, or 868 MHz ISM sub-GHz bands. Subsequently, the availability of 169 MHz for such standard enabled longer transmission range due to the inherently lower path losses. The standard was designed to be robust, power efficient allowing for long coverage ranges, since it intrinsically operates in harsh environments due to the fact that utility meters are typically installed in hardly reachable spots (e.g., below ground level, in remote basements, sheds, or culverts). It supports several dialects and modes that are exploited in automatic and remote meter reading applications, which are directly managed by utility companies and driven by their specific requirements. As the name hints, the standard supports a wireless bus in which the sensor nodes, usually installed on utility meters, uplink data (according to an encryption and authentication scheme) towards a concentrator by making use of the Gaussian Frequency Shift Keying (GFSK) modulation. Finally, depending on the selected dialect, the standard allows for a maximum data-rate of either 2.4 kbps or 19.2 kbps, and of a channel bandwidth of either 12.5 kHz or 50 kHz.

1.3 Satellite Technologies

These standards are the newest ones belonging to the framework of IoT communication technologies. Some of them have features currently under development, some are more tested and adopted, but all of them are gaining momentum and attracting the attention of both the industries and the academia. On the one hand, the biggest advantage is that global connectivity is ensured; on the other hand, the major drawbacks are that sensor nodes need to have a clear view of the sky to successfully transmit data to satellites, translating into the reduction of the application scenarios (they cannot work, for instance, underground). In addition, another downside is that such technologies are not suitable for low latency applications, because satellite constellations are in continuous expansion, meaning that at the moment some temporal coverage lacks occur, albeit they are bound to diminish and disappear as soon as the number of deployed satellites will be sufficiently

high. Currently, the literature has barely no works focusing on pervasive measurement systems exploiting satellite IoT standards. One motivation is that they appeared in the market relatively recently. Nonetheless, a list of the principal satellite IoT technologies is given below to provide a complete overview of the topic of transmission technologies for IoT, but a deeper technical comparison cannot be done since all of the specifications have not been disclosed yet for each of the technologies.

1.3.1 Lacuna

Lacuna was one of the first IoT satellite technologies available in the market. It makes use of LEO CubeSats acting as data forwarders, exploiting LoRa links to receive packets from sensor nodes and to convey them to the closest ground station. Indeed, Lacuna succeeded in performing LoRa connectivity towards the sky. However, in this context LoRa modulation is exploited in licensed frequency bands, meaning that users have to subscribe a data plan. In particular, sensor nodes transmit data to satellites, and they store such information as long as a network ground station is visible during their orbiting. Then, the ground station makes available such data to the users by resorting to the Internet connection.

1.3.2 Fossa

LoRa modulation for satellite transmissions is also exploited by Fossa. Conversely with respect to Lacuna, Fosse makes use of LoRa links in unlicensed ISM bands, making the solution less reliable but more low-cost because no data plans need to be subscribed by the users. The working principle is the same as Lacuna, meaning that sensor nodes send data towards satellites, that store the incoming packets as soon as a ground station is visible. Then, they convey such information to the ground stations that make it available to the users. For what concerns satellites, also Fossa deployed its own constellation of LEO CubeSats. In addition, Fossa gives the opportunity to users to set up their own dedicated infrastructures, starting from sensor nodes, up to satellites and ground stations, to offer the maximum flexibility.

1.3.3 Astrocast

Astrocast is another alternative in the framework of satellite IoT technologies that set up its own constellation of LEO CubeSats. It operates in licensed spectrum exploiting carrier frequencies in between 1 GHz and 2 GHz, therefore users have to subscribe a data plan which includes the usage of Astrocast back-end infrastructure dealing with the running of

the whole network. Regarding the network working scheme, it resembles to the ones of the competitors. Indeed, even Astrocast satellites act as data forwarders storing data in their internal memory to relay it to the closest ground station, that coveys such data to the users by means of the dedicated back-end.

1.3.4 Swarm

Swarm network currently counts up to more than 170 LEO CubeSat satellites, but the constellation is bound to be expanded soon. This implies that, for a given geographic position, a constant coverage over time cannot be ensured. Indeed, satellites broadcast beacon signals that are received by transceivers. Then, they start sending all the messages they internally stored in advance. Specifically, for what concerns coverage, the farther from the equator, the more constant over time. In particular, almost no lack of coverage is experienced at the Poles. Concerning the transceiver, it is a modem named Swarm Tile, that sends information exploiting the Swarm satellite network, transmitting data exploiting the $137 - 138$ MHz band in downlink (although this feature is reserved for commercial purposes only) and the $148 - 150$ MHz band in uplink. Together with connectivity, the module is also provided with Global Positioning System (GPS) localisation features, allowing the acquisition and the transmission of the sensor node position in an integrated manner. Data packets, whose maximum payload is up to 192 B, can be sent only in a limited number depending on the subscribed data plan. Once again, the working scheme of the technology is the same that comparable standards follow: satellites store incoming messages from modems, and then they forward data to the closest ground station as soon as it is visible. Finally, the ground station coveys such information to the users via the Internet. Concerning the adoption of Swarm technology within the literature, it was exploited for setting up a monitoring and tracking infrastructure for athletes performing sport in extreme and remote environments [50], and for realising an interface to be adopted in marine contexts to enable satellite communication from offshore facilities [51].

Chapter 2

General Methodology for Performance Measurement

In the following Chapters, many measurement campaigns sorted out within critical and harsh environments will be presented. Their aim is mainly to assess the performances of distributed measurement infrastructures deployed in such contexts. In particular, for some test setups performances will be evaluated as path losses due to the relative media at hand, while for some others they will be assessed by making use of reception parameters (e.g., Received Signal Strength Indicator (RSSI), Signal-to-Noise Ratio (SNR)) for the whole wireless channel. However, both the methods are grounded on the measurement of RSSIs, and these should be properly sampled by exploiting a spectrum analyser. Indeed, by making reference to Figure 2.1, a wireless measurement system is usually characterised by sensor nodes, which sample and wirelessly transmit whatever physical quantity on the basis of the system requirements, and receivers, which demodulate and forward the incoming signals. The latter ones are typically able to measure the relative RSSIs and SNRs for the received packets. Without losing generality, let us consider in the following only the RSSIs provided by the receivers. Sensor nodes transmit data at a given transmitter power output, namely P_{TX}, that is attenuated both by the intrinsic effect of the propagation media (regardless of its harsh characteristics), and by miscellaneous losses accounting for sundry circumstances (e.g., polarisation mismatch between the transmitter and receiver antennas). Let us call the sum of all the losses as L, so to logarithmically express the received power, namely P_{RX}, as $P_{RX} = P_{TX} - L$.

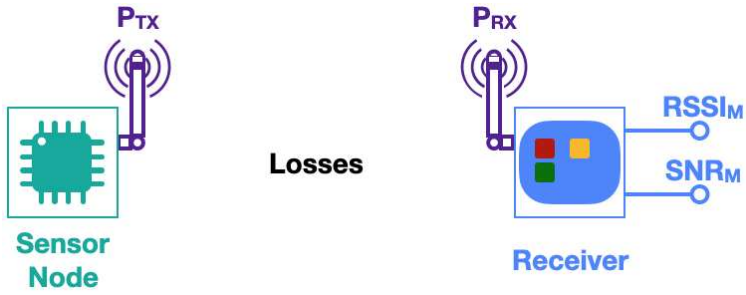

Figure 2.1: Wireless measurement system block scheme. P_{TX} stands for the transmitter power output, P_{RX} stands for the received power, while $RSSI_M$ and SNR_M respectively stand for the measured RSSI and SNR given by the receiver.

At the same time, P_{RX} would be the power a spectrum analyser would measure if it would be employed. However, in real application scenarios hosting a wireless measurement infrastructure, receivers are not spectrum analysers, but they are rather gateways since they receive wireless signals that they demodulate and, in most of the cases, forward data to a remote cloud. On the contrary, spectrum analysers are not generally conceived to act as data receivers. In addition, and especially for wireless links taking place in harsh environments, the received packets are likely to have an associated power under the noise floor of spectrum analysers, thus making them unsuitable. On the other hand, receivers are given with proper electronics capable of rejecting noise adding up throughout transmission (thus improving sensitivity), along with demodulators and filters. In particular, reception metrics they extract, namely the measured RSSI $RSSI_M$, and measured SNR SNR_M, are sampled at the end of the receivers and demodulators, therefore raising discrepancies with P_{RX}. In particular, the adopted gateways for the tests described in the following Chapters provided 1 dB and 0.1 dB as resolution respectively for RSSIs and SNRs. In light of this, and owing to the fact that receivers are actually employed in wireless measurement infrastructures, in the following measurement campaigns spectrum analysers will not be employed to comply with real measurement setups deployed in the field. Moreover, this justifies potential incongruities between the results of the following measurement campaigns, in terms of received power, and the estimates given by the corresponding theoretical model on path loss within the propagation media at hand.

In order to assess whether resorting to receivers as measurement instruments is reasonable, some tests were carried out in laboratory by exploiting as reference the LoRa modulation and the LoRaWAN protocol, although the results can be extended to whichever transmission technology. In particular, tests aiming at assessing the effect of

packets payload length on RSSI, the accuracy of LoRaWAN gateways in measuring RSSI, and the effect of modulation on RSSI were carried out.

2.1 Effect of Payload Length on RSSI

The aim of these tests was to evaluate whether the payload length affects RSSI values. Therefore, six payload lengths (i.e., 10 B, 20 B, 30 B, 40 B, 50 B and 60 B) were tested in laboratory by broadcasting 300 packets and by making use of a LoRaWAN transmitter exploiting $P_{TX} = 14$ dBm. The LoRaWAN gateway was placed 3 m apart from the node, in a free space condition, and it was employed to measure RSSI. Table 2.1 summarises the test settings.

Table 2.1: Summary of the settings related to the test assessing the effect of payload length on RSSI.

Transmission Technology	**P_{TX}**	**SF**	**CR**	**Payload**	**# Packets**	**Distance**
LoRaWAN	14 dBm	7	4/5	10 B, 20 B, 30 B, 40 B, 50 B, 60 B	300 for each payload	3.00 m

Figure 2.2 shows the results of such tests. First of all, no packet losses were experienced. Secondly, mean RSSIs underwent variations due to payload length which, in turn, could have caused variations in path losses. However, these divergences do not follow a proportional trend in comparison with payload length (e.g., the bigger the length, the lower the RSSI). Moreover, it is reasonable that the motivation for the variations can be ascribed to statistical fluctuations. In addition, the environmental condition usually has some kind of influence on LoRaWAN transmission that leads to nonlinear results. Indeed, such phenomenon will be experienced in the measurements presented in the following Chapters. Nonetheless, this is not significant for the effectiveness of the measurement infrastructures, and it is not related to the payload length (as it is shown in this Section). Anyway, their extent is really limited (i.e., 8 dB) thus having a very little significance on path loss estimates.

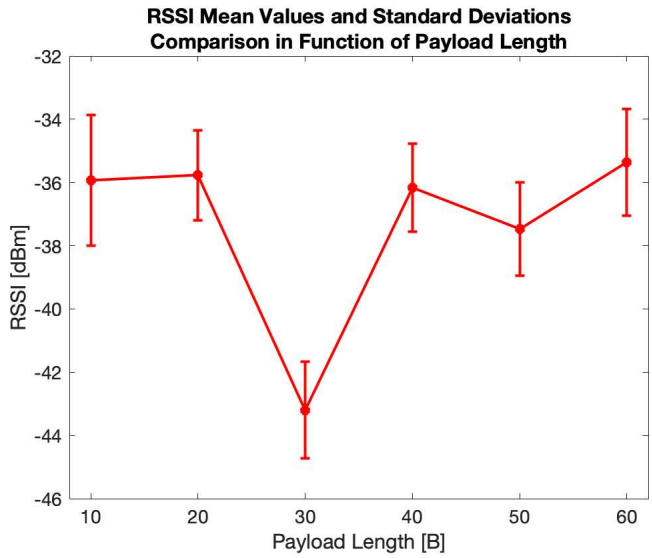

Figure 2.2: RSSI mean values and standard deviations as a function of payload length.

2.2 LoRaWAN Gateway RSSI Measurement Accuracy and Effect of Modulation on RSSI

LoRaWAN gateways are usually exploited for their primary feature (i.e., receiving, demodulating and forwarding LoRaWAN packets to a remote cloud) since they are not proper measurement instruments. However, assessing their RSSI measurement accuracy is fundamental for the following experiments. Such goal was achieved by means of laboratory tests during which a LoRaWAN sensor node was put $3.00\,\text{m}$ apart from a LoRaWAN gateway, and $3.00\,\text{m}$ apart from a spectrum analyser (i.e., the Rigol DSA815) at the same time. Such distance was selected since it was the longest allowing for the avoidance of obstacles between the transmitter and the receivers, as well as the avoidance of obstacles in the surroundings of such devices. The three devices were equipped with as many identical antennas, while the LoRaWAN sensor node performed 300 transmissions by exploiting $P_{TX} = 14\,\text{dBm}$, and a $10\,\text{B}$ payload. Finally, the RSSI values provided by both the spectrum analyser and the LoRaWAN gateway were sampled and stored for each of the transmissions.

Investigating the effect of modulation on RSSI is important as well. Therefore, such dependency was studied by resorting to laboratory tests during which a signal

generator (i.e., the Rohde & Schwartz SMH 845.4002.52) was exploited to broadcast unmodulated signals (i.e., sine waves) and the Rigol spectrum analyser was employed as receiver. The bandwidth of the spectrum analyser was set at 2 MHz, in the $867 - 869$ MHz band and centred at 868 MHz. Indeed, in almost each of the measurement campaigns presented in the following Chapters, eight different channels were exploited for LoRaWAN transmissions (i.e., 867.1 MHz, 867.3 MHz, 867.5 MHz, 867.7 MHz, 867.9 MHz, 868.1 MHz, 868.3 MHz, and 868.5 MHz): such band allowed to acquire the related RSSIs to each transmission. A 30 kHz resolution bandwidth was adopted, which entailed a sweep time of 10 ms. In order to acquire all the data, continuous sweep mode was selected, exploiting LabVIEW for data acquisition and storage, and MATLAB for post processing. The two devices were equipped with two identical antennas and they were put 3.00 m apart. First of all, the signal generator was used to generate a sine wave having the frequency of 868 MHz (i.e., a common frequency for LoRaWAN uplinks), and a power output of 14 dBm was exploited. The RSSI measured by the spectrum analyser was sampled and recorded. Secondly, the signal generator was exploited to sweep the $862 - 875$ MHz ISM band with a granularity of 100 kHz and by making use of 14 dBm as power output. For each of the frequencies, the generator broadcast a sine wave having the frequency at hand, and the relative RSSI measured by the spectrum analyser was sampled and stored. Finally, in order to understand the effect of modulation on RSSIs, the results from the test employing just a single sine wave at 868 MHz and the ones sweeping the aforesaid ISM band were compared with the mean RSSI values, measured by the spectrum analyser, relative to the tests that aimed to assess the accuracy of the RSSI measurements of the LoRaWAN gateway. Table 2.2 summarises the test settings.

Table 2.2: Summary of the settings related to the test assessing the RSSI measurement accuracy of LoRaWAN gateways, and the effect of modulation on RSSI.

Transmission Technology	$\mathbf{P}_{TX}$	**SF**	**CR**	**Payload**	**# Packets**	**Distance**
LoRaWAN	14 dBm	7	4/5	10 B	300	3.00 m
No Modulation	14 dBm	–	–	–	300	3.00 m

Concerning the LoRaWAN gateway RSSI measurement accuracy, tests showed that mean RSSI values from the gateway differed from the ones of the spectrum analyser 3.6 dB thus pointing out the reliability of the gateway readings. Such result is visible by the comparison in Figure 2.3a by taking into account the blue bar and the orange bar: the former one represents the mean RSSI values from the gateway, while the latter one represents the mean RSSI values from the spectrum analyser. Moreover, tests also

showed that modulation has barely no effect on RSSIs. Indeed, the RSSI of the sine wave at 868 MHz (which can be seen in Figure 2.3c), measured with the spectrum analyser, differed from the one of the LoRaWAN signals, measured with the spectrum analyser, 0.4 dB. This result is reported in Figure 2.3a by considering the orange bar and the yellow bar: the former one represents the mean RSSI values from the spectrum analyser related to LoRaWAN signals, while the latter one represents the RSSI value from the spectrum analyser related to the 868 MHz sine wave. Moreover, the mean RSSI values, measured with the spectrum analyser, of the sine waves having increasing frequency within the $862 - 875$ MHz ISM band differed from the RSSI value of the LoRaWAN signals, measured with the spectrum analyser, 0.1 dB. This can be noticed in Figure 2.3a by looking at the orange bar and the purple bar: the former one represents the mean RSSI values from the spectrum analyser related to LoRaWAN signals, while the latter one represents RSSI value from the spectrum analyser related to the sine waves sweeping within the aforesaid ISM band. In addition, the difference between the maximum mean RSSI value trend of the sine waves having increasing frequency and the minimum RSSI value of the same sine waves is of 1.2 dB (see Figure 2.3b). Therefore, each of these tests confirmed the limited effect of modulation on RSSI values. A final remark on modulations can be drawn. Of course, they do play their roles in order to enhance transmission performances. However, they mainly impact on robustness towards interference as well as receiver sensitivity. Besides, the latter one is defined by the hardware forming the devices and hence it is usually known a priori. Nevertheless, with the same modulation and technology, what makes a huge difference amid links taking place within free space and within critical contexts is the attenuation due to the latter ones which notably causes communication disruption. Therefore, by resorting to the aforementioned results, modulations impact on path loss and packet loss could be considered as of a minor extent since for each of the testing setup mean path losses discrepancies were always within a few dB interval, while packet losses remained constant.

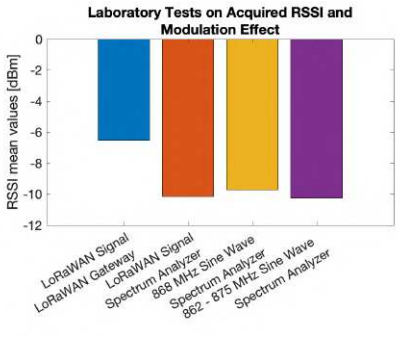

(a)

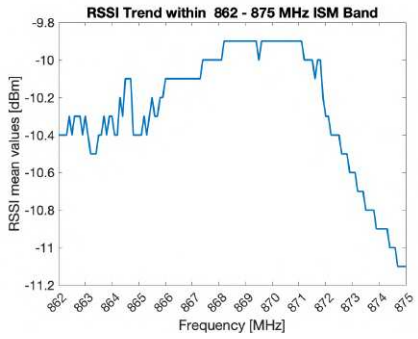

(b)

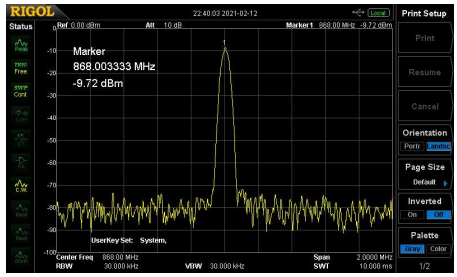

(c)

Figure 2.3: Laboratory tests results on LoRaWAN gateway RSSI measurement accuracy and on the effect of modulation on RSSI: (a) RSSI mean values comparison amid LoRaWAN gateway measurements (in blue), spectrum analyser receiving LoRaWAN signals (in orange), spectrum analyser receiving a sine wave at 868 MHz and spectrum analyser receiving sine waves having frequencies sweeping within the $862 - 875$ MHz ISM band; (b) RSSI mean values trend within the $862 - 875$ MHz ISM band; (c) spectrum analyser snapshot of the received sine wave at 868 MHz.

Chapter 3

Above-the-Sea Environments

Monitoring offshore assets, plants, and facilities require the establishment of a remote measurement infrastructure capable to cover several kms by means of wireless above-the-sea links. Such setting is intrinsically harsh because of the fact that the sea is a huge salty water basin, acting as a massive ground plane. Moreover, owing to the long-length links, it can be highly likely that receivers and transmitters are not in Line of Sight (LoS). This condition may be due to the distance from the horizon of the transmitters, owing to the Earth curvature.

3.1 Path Loss Model

The quality of wireless transmissions is mainly conditioned by two key factors: LoS between the transmitter and the receiver, and enough link margin at the receiver side. The former ensures the best propagation thus enlarging the probability of a successful communication. Such chances are furthermore enhanced if the prolate ellipsoidal volume wrapping the direct LoS path between the transmitter and the receiver (i.e., the first Fresnel zone) is free from obstacles. On the other hand, enough link margin at the receiver side is fundamental for the feasibility of the transmission. In other words, it is mandatory in order to achieve the transmission that the RSSI of the received signal is higher than the receiver sensitivity. This requirement is assessed by evaluating the link budget of the communication.

The link budget equation accounts for all of the losses and gains from the transmitter to the receiver along the communication channel. Hence, the simplest link budget equation, logarithmically expressed, is a superposition of terms as

$$P_{RX} = P_{TX} + G_A - L \tag{3.1}$$

where P_{RX} and P_{TX} are in turn the received power and the transmitter power output both expressed in dBm, G_A represents the antennas gains on either the sides of the communication channel expressed in dBi, and L stands for all the losses the channel is

affected by expressed in dB. Therefore, the aforesaid link margin L_m is calculated as

$$L_m = P_{RX} - S_{RX} \tag{3.2}$$

where S_{RX} is the receiver sensitivity expressed in dBm.

For the sake of completeness, it has to be also underlined that there exists another crucial requirement that has to be usually guaranteed in order to fulfil a satisfactory transmission: the SNR limit. In general, apart from achieving enough link margin, a signal whose power is bigger than the one of the noise that was added on it during its transmission has to be received. Such a condition entails a positive SNR provided that it is logarithmically expressed or, alternatively, greater than 1 if the SNR is linearly expressed.

Coming back to link budget, a more detailed equation, though still simplified, can be derived by making reference to Figure 3.1 which displays a block diagram of a communication channel:

$$P_{RX} = P_{TX} + G_{TX} - L_{TX} - L_{FS} - L_M + G_{RX} - L_{RX}. \tag{3.3}$$

Figure 3.1: Gains, in blue, and losses, in yellow, of a communication channel to be accounted within link budget equation.

In Equation 3.3, P_{TX} and P_{RX} are the same of Equation 3.1, G_{TX} and G_{RX} respectively are the gains of the transmitting and receiving antennas expressed in dBi, while L_{TX} and L_{RX} are the losses due to cables and connectors at transmitter and receiver sides, respectively. L_{FS} is the path loss, and it is normally named as free space loss. Finally, L_M represents miscellaneous losses due to a manifold of potential causes (e.g., antennas polarisation mismatch, obstructions within the first Fresnel zone and so forth). Both the latter two losses are expressed in dB.

L_{FS} in LoS propagation is the attenuation between the two antennas (i.e., the transmitting and the receiving ones) due to the distance between the extrema of the transmission link, considering that such a gap, better if the entire first Fresnel zone taken into account, is free from obstacles. Such a loss can be expressed via different equations in function of the units of measurement in which its composing terms are specified. The standard formula is

$$L_{FS} = \left(\frac{4\pi df}{c}\right)^2 \tag{3.4}$$

where d is the distance in m between the transmitter and the receiver, while f is the carrier frequency in Hz. On the other hand, a commonly adopted version is

$$L_{FS} = 32.45 + 20log_{10}(D) + 20log_{10}(f) \tag{3.5}$$

where D is the distance between the transmitter and the receiver expressed in km and f is the transmission carrier frequency expressed in MHz.

The Fresnel zone is an infinite series of confocal prolate ellipsoidal three-dimensional regions enveloping the direct LoS path between the transmitting and the receiving antennas. It is employed in propagation theory to evaluate losses due to reflection and diffraction between the endpoints of the wireless link. Such zones are usually called F_i with $i \in \mathbb{N}^+$ where F_1 is the smallest one. Regularly, a slight abuse of notation is committed since also the maximum radius relative to the i^{th} zone is marked as F_i.

In order to grasp the practical meaning of the Fresnel zone, it has to be recalled that radio frequency waves propagate not only directly along the LoS path, but also in an off-axis fashion. This phenomenon entails reflections which in turn imply a phase variation on the reflected signal. Unfortunately, though, if such unwanted and often unpredictable changes of phase amount to $(2k+1)\pi$ with $k \in \mathbb{N}$, then the direct and reflected signals cancel out at the receiver side since they have opposite phases. On the other hand, if the change of phase is equal to $2k\pi$ with $k \in \mathbb{N}$ then the two signals will enhance each other at the receiver side due to the fact that they are perfectly in phase. However, reflections should be avoided since phase changing ordinarily leads to destructive interference and signal weakening.

A more rigorous definition is that the n^{th} Fresnel zone is the locus of points belonging to the three-dimensional space such that a two-segment transmitted reflected signal, that deflects off a point on such a surface, will have a phase change equal to $(i+1)\pi$ with respect to the signal propagated along the direct LoS path. Those zones are ellipsoids whose foci are the transmitter and the receiver antennas. In other words, even numbered Fresnel zones cause a phase change of π, thus damaging wave propagation, whilst odd numbered ones produce a phase change of 2π, wherefore intensifying the broadcast. Hence, despite an intuitive belief, LoS between transmitter and receiver is not theoretically sufficient to assure adequate wireless transmissions. Indeed, due to the complex nature of radio propagation, obstructions within the first Fresnel zone should be shunned since they can cause significant signal weakening consequently vanishing the enhancing effect of such a zone. Sadly, though, it is almost unfeasible to obtain a completely empty F_1 so at least $60\,\%$ clearance should be achieved [52].

Figure 3.2 reports an example of the first Fresnel zone: D is the distance between the transmitter and the receiver (i.e., the direct LoS path) while F_1 is the maximum radius of the zone which occurs at $\frac{D}{2}$. There exist formulas that evaluate F_1 depending on the units

of measure in which its terms are expressed. If D is specified in km and the transmission frequency f is defined in GHz, then F_1 is calculated in m as

$$F_1 = 8.656\sqrt{\frac{D}{f}}. \tag{3.6}$$

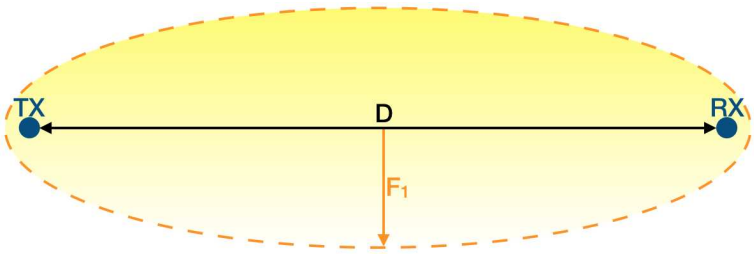

Figure 3.2: First Fresnel zone example.

So far it was pointed out that achieving the direct LoS from the transmitter and the receiver along with a significant clearance of the first Fresnel zone is considerably beneficial to increase the chances of adequate wireless transmissions. For what matters the direct LoS, it is obtained by checking whether or not the receiving antenna is beyond the horizon with respect to the transmitting one. Fresnel zone clearance has to be assured not only by avoiding obstacles like buildings or mountains, but also by accounting for the Earth curvature especially for long transmission distances. Both of these issues may be faced by overhead installing the antennas.

The direct LoS assessment considering the distance of the horizon from the transmitting antenna may be simply performed by making use of the Pythagorean theorem. Let approximate the Earth as a perfect sphere, having radius $R = 6371\,\text{km}$, with no terrain irregularities: such hypothesis is a suitable approximation when links take place above-the-sea. Moreover, suppose that the transmitting antenna is mounted at an altitude h_{TX} above sea level (see Figure 3.3 bearing in mind that it is not in scale since its purpose is merely qualitative). Then, the distance from the horizon D_h expressed in m, provided that either R and h_{TX} are so, is

$$D_h = \sqrt{(R + h_{TX})^2 - R^2} = \sqrt{h_{TX}^2 + 2Rh_{TX}}. \tag{3.7}$$

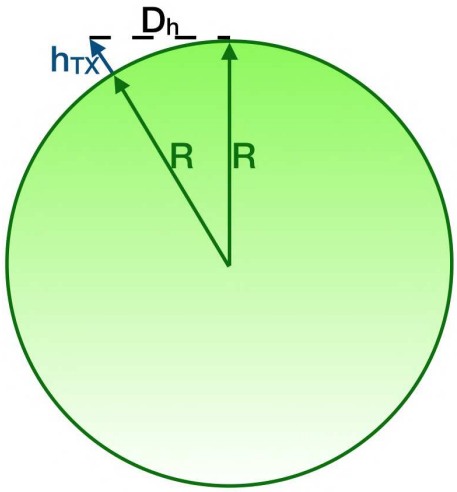

Figure 3.3: Evaluation of the distance from the horizon.

Earth curvature should be taken into consideration whenever long distance links (i.e., more than few kilometers) are designed. In particular, the bulge amid the two endpoints could obstruct the first Fresnel zone. The maximum Earth bulge height H expressed in m, which is experienced in the midpoint of the link (see Figure 3.4 bearing in mind that it is not in scale since its purpose is merely qualitative), is computed as

$$H = \frac{1000D^2}{8kR} = \frac{125D^2}{\frac{4}{3}R} = \frac{375D^2}{4R} \tag{3.8}$$

where D is the distance between the endpoints expressed in km, R is the Earth radius and k is a factor which accounts for the bending effect on radio waves caused by the declining of atmospheric pressure. Practically, this phenomenon implies an enlargement of the Earth radius by factor k. Actually, k also depends on weather conditions, but it is averagely equal to $4/3$.

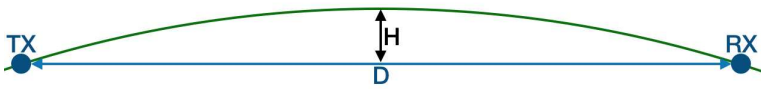

Figure 3.4: Example of the height of the Earth bulge in transmission links.

3.2 Measurement Setup

A wireless infrastructure was set up in order to test above-the-sea links. Specifically, this research topic covered the monitoring tasks related to an offshore sea farming plant. Due to the application scenario, and to the adopted methodology, such tests aimed at assessing performances by relying on measuring reception parameters like RSSI and SNR. In other words, the whole path loss was considered instead of the mere effect ascribed to the presence of the sea.

A prototype of a LoRaWAN network infrastructure was fully developed for enabling data collection from offshore sensor nodes. The network prototype (see Figure 3.5) includes:

- **Sensor Nodes**, that are offshore installed, which are in charge of collecting data and wirelessly transmit them towards land via encrypted LoRa packets exploiting a frequency hopping scheme as LoRaWAN protocol prescribes;
- **Gateways**, behaving as packet forwarders, which are responsible for the demodulation of the signals and for the forwarding of the received information to remote servers by making use of the Message Queue Telemetry Transport (MQTT) protocol. Moreover, gateways are capable of measuring RSSIs and SNRs for each received packet;
- **Network Server**, that deals with the incoming packets by processing and storing them in order to extract any useful data;
- **Application Server**, which makes data available to users via a graphic interface.

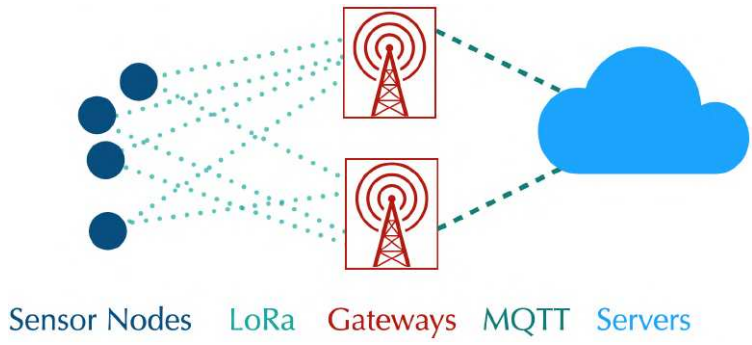

Figure 3.5: Block diagram of the prototype of the LoRaWAN network infrastructure.

The tests in this application scenarios were sorted out in two short-term measurement campaigns.

3.2.1 First Short-Term Measurement Campaign

For such tests, just a temporary installation of a network prototype was accomplished. A sensor node was set up simulating its future deployment on a seamark buoy. Therefore, its antenna was placed on top of a telescopic pole having a maximum height of $3.50\,\mathrm{m}$, and in particular two different heights for the transmitting antenna were tested in order to check the feasibility of the link simulating a worst case scenario. Hence, it was at an altitude $h_{TX_1} = 3.50\,\mathrm{m}$, and then at an altitude $h_{TX_2} = 2.10\,\mathrm{m}$ above sea level. Moreover, the sensor node with the pole supporting the antenna was set up on board of a boat. Figure 3.6 displays the antenna installed on the pole lying on the floor of the boat and the view reaching the offshore measurements spot.

(a) (b)

Figure 3.6: Offshore setup for the short-term measurement campaigns: (a) offshore end node antenna and its pole; (b) view approaching the tests spot.

In order to enhance the strength of the wireless link, a directional Yagi-Uda antenna

having a gain $G_{TX} = 9$ dBi was selected, and it was connected to a B-L072Z-LRWAN1 discovery kit board produced by STMicroelectronics via a 4.00 m long coaxial cable whose overall loss, $L_{TX} = 2.10$ dB, was measured by means of a vector network analyser. For this short-term measurement campaign, the discovery kit board plays the role of the sensor node, transmitting a 51 B-long test string. Eight different channels belonging to the 868 MHz ISM band were exploited to conduct the transmission tests so as to establish a frequency diversity scheme. Therefore, the B-L072Z-LRWAN1 discovery kit board performs a frequency hopping in a pseudo-random fashion for each transmission, by switching amid the channels having the following carrier frequencies: 867.1 MHz, 867.3 MHz, 867.5 MHz, 867.7 MHz, 867.9 MHz, 868.1 MHz, 868.3 MHz, and 868.5 MHz. Moreover, several packets were transmitted, by employing six different Spreading Factors (SFs) (i.e., $7, 8, \ldots, 12$), and by exploiting a Coding Rate (CR) of $4/5$ and a bandwidth of 125 kHz.

For these tests in above-the-sea settings, two gateways were ashore installed, and for both the short-term measurement campaigns they were placed on top of a knoll, whose altitude is 6.00 m above sea level. With the aim of better exploiting the first Fresnel zone, the receiver antennas were placed on a 7.20 m pole raised on top of the knoll. In particular, they were installed on the pole upper extreme by mounting them on a 2.00 m bar fastened to the pole forming a cross. Hence, by summing up the altitude of the knoll and the length of the mounting pole, the receiver antennas were located at a height of $h_{RX} = 13.20$ m above sea level. Specifically, the length of the pole was measured by exploiting a measuring tape (having an accuracy of ± 0.1 cm), while the altitude of the knoll was measured by resorting to the satellite imagery analysis provided by Google Earth software. As it will be seen later on, such a set up was far from being sufficient to allow for the 60 % clearance of the first Fresnel zone, but, in order to keep the installation procedures as simple as possible, the antennas could not be placed any higher since only a temporary installation was planned for both the short-term campaigns.

The gateways were implemented by means of two RAK831 devices produced by the RAKWireless, which is a multi-channel LoRaWAN concentrator, driven by a Raspberry Pi 3 model B. Figure 3.7 shows the gateways setup on top of the knoll.

Two directional helical antennas having a gain $G_{RX} = 14$ dBi were selected for the gateways. They were in turn connected to the gateways via two 15.00 m long coaxial cables having a total loss of $L_{RX} = 4.06$ dB each, that was measured by exploiting a vector network analyser. Finally, Internet connectivity was guaranteed by a 4G LTE router.

Tests were performed from offshore towards land covering the distance $D = 8.33$ km. Figure 3.8 reports the position of the sensor node (i.e., point A), the position of the

Figure 3.7: Ashore setup of the gateways.

gateways (i.e., point B) and the length of the link (i.e., the red line), whilst Table 3.1 lists the coordinates of points A and B. Specifically, point A coordinates were provided by the on board GPS of the boat, while point B coordinates were given by the GPS of a smartphone. Then, the distance D was calculated a posteriori by making use of Google Earth software. Concerning its associated uncertainty, it can be considered that the accuracy of GPS devices can be estimated in ± 3 m. Then, according to the uncertainty

propagation, D can be expressed with an associated uncertainty of ± 5 m. This is the reason why it is expressed with a resolution of 10 m.

Table 3.1: Coordinates of points A and point B of Figure 3.8.

Point	Latitude [°]	Longitude [°]
A	42.895494	10.629385
B	42.942858	10.550552

Figure 3.8: Map showing the positions of the sensor node, point A, and of the gateways, point B, along with the covered distance, red line.

The tests were accomplished with smooth sea conditions having a maximum wave height of 50 cm (such information was gathered from a bulletin). It was a sunny day with a mean temperature of $18\,^{\circ}$C and a gentle breeze whose average speed was of 4 m/s. Testing the system with more severe marine and weather conditions would have been extremely interesting. Unfortunately, though, the exploited boat for the fulfilment of the tests could not cast off in such cases. Moreover, an amount of 600 packets were transmitted by respecting the laws on temporal occupation of the transmitting band [53] in an overall amount of time of approximately 14 h.

The first short-term measurement campaign was sorted out in 2 groups, namely $\#1$

and $\#2$, by covering the same link from point A to point B (see Figure 3.8) and by testing all the SFs by transmitting an amount of 300 packets per test collection (i.e., 50 packets per SF per collection). The test series differed from each other for the heights of the transmitting antenna above sea level.

A circumstance that has to be verified is to check whether or not points A and point B were in LoS. Hence, by making reference to Equation 3.7, and by considering h_{RX} and h_{TX}, it can be noticed that points A and B are always in LoS since the former is not behind the horizon because D_h is bigger than D. Table 3.2 summarises what has just been described and it also contains the results computed by applying Equation 3.7.

Table 3.2: Antennas heights, exploited SFs, number of transmitted packets and distance of the horizon from the receiver antennas for each trial group.

Transmission Technology	**Group**	h_{TX} **[m]**	h_{RX} **[m]**	P_{TX} **[dBm]**	**SFs**	**CR**	**Transmitted Packets**	D_h **[km]**
LoRaWAN	$\#1$	3.50	13.20	14	$7-12$	$4/5$	300	11.12
	$\#2$	2.10						11.89

At this stage, the concepts introduced in Section 3.1 can be applied and evaluated on the wireless link that has just been illustrated. First of all, the maximum radius of the first Fresnel zone F_1 can be calculated by applying Equation 3.6. Since a frequency diversity scheme was implemented by means of frequency hopping among the channels, F_1 is evaluated by exploiting as carrier frequency the mean value of the ones previously listed (i.e., 867.8 MHz). The same convention holds for all the following Equations in which the frequency of the carrier is involved. Concerning the maximum height of the Earth bulge H amid the link endpoints, it can be derived by means of Equation 3.8. The theoretical free space loss L_{FS} can be computed according to Equation 3.5, therefore an overestimation of the received signal power P_{RX} can be obtained via Equation 3.3. Indeed, the latter is estimated by plugging into its Equation the values cited beforehand (i.e., G_{TX}, G_{RX}, L_{TX} and L_{RX}), by exploiting the maximum power output for the transmitter P_{TX} according to the regional regulations [53] (i.e., 14 dBm) and by considering a null value for miscellaneous losses L_M. Actually, there are several losses of that kind due to the fact that, as it will be seen in a while, the $60\,\%$ of the first Fresnel zone is not free from obstacles. Unfortunately, though, the loss introduced by such a phenomenon is hardly numerically assessable. For the same reason, an overestimation of the link margin L_m may be computed by exploiting Equation 3.2 bearing in mind that the gateways have a sensitivity which varies along with the SF and the bandwidth. Indeed, according to the LoRaWAN concentrators datasheet [54], and considering that a bandwidth of 125 kHz

was exploited throughout the tests, the gateways sensitivity S_{RX} spans from -137 dBm at $SF = 12$ to -126 dBm at $SF = 7$. Another consequence stemming from the presence of miscellaneous losses is that a lower value of P_{RX}, with respect to the one that would have been obtained from Equation 3.3, was truly experienced on average during the measurements thus entailing a narrower L_m. Notice that all of these quantities do not depend on the set of tests since they only depend on the length of the link D. All the results stemmed out from the aforementioned Equations are reported in Table 3.3.

Table 3.3: Values of the quantities introduced in Section 3.1 for the fist short-term measurement campaign.

Quantity	**Value**
F_1	26.818 ± 0.008 m
H	1.021 ± 0.001 m
L_{FS}	109.631 ± 0.005 dB
P_{RX}	-78.791 ± 0.005 dBm
Minimum L_m	47.209 ± 0.005 dB
Maximum L_m	58.209 ± 0.005 dB
D	8.33 ± 0.005 km

The last condition to be assessed is the percentage of clearance of the first Fresnel zone F_{1_C}. Indeed, despite the LoS status between the link endpoints, F_1 is partially occupied by the sea because of the Earth bulge. Figure 3.9 shows a qualitative report of the wireless link respectively when h_{TX_1} is exploited, in Figure 3.9a, and h_{TX_2} is used, in Figure 3.9b. Such images are obtained by making use of BotRf [55] which is a Telegram Bot that aids in the planning phase of wireless links. The cyan line represents the direct LoS path between the link endpoints while the magenta one represents the $60\,\%$ of F_1. Finally, the brown area indicates the Earth curvature while the green one indicates the terrain profile. The reason for which the green area is for the most part flat is that it is actually occupied by the sea. Either the brown and green areas take into account the factor k (see Equation 3.4) for the bending effect on radio waves due to the declining of atmospheric pressure. As it can be noticed, LoS is effectively achieved and the first Fresnel zone is densely occupied.

However, by exploiting BotRf, it can be observed that estimates, though still rough, of the actual clearances are $20\,\%$ for h_{TX_1} and $15\,\%$ for h_{TX_2} (see Figure 3.10 bearing in mind that the same colour convention of Figure 3.9 is observed). Therefore, the whole tests setup can be considered as a worst case one (apart from the fact that a marine environment is itself a harsh environment) because of the following reasons:

- Antennas on both sides were not installed by making use of overhead spots in order

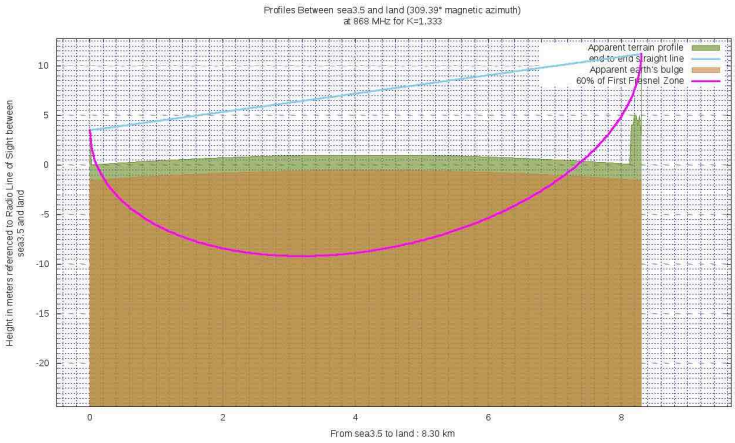

(a)

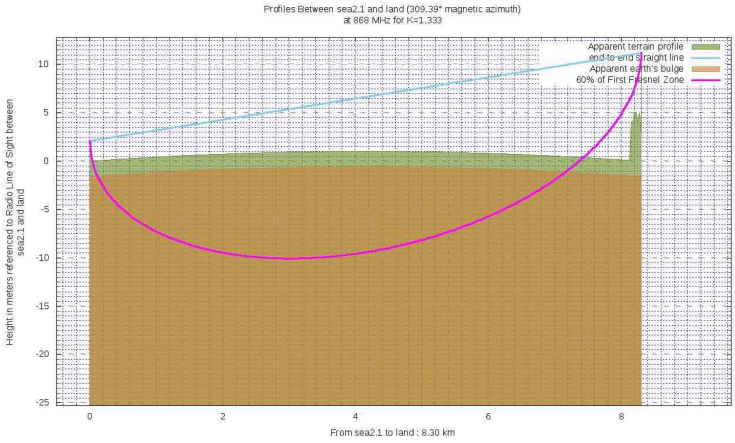

(b)

Figure 3.9: Ground profiles for either the exploited altitudes for the transmitting antenna: (a) 3.50 m; (b) 2.10 m.

to limit the complexity related to their installation which was thought to be only a temporary one;

- As a direct consequence of the last point, only a limited clearance of the first Fresnel zone (far from being the 60 %) was available;
- For the transmission, the biggest CR was adopted, which might had caused the loss

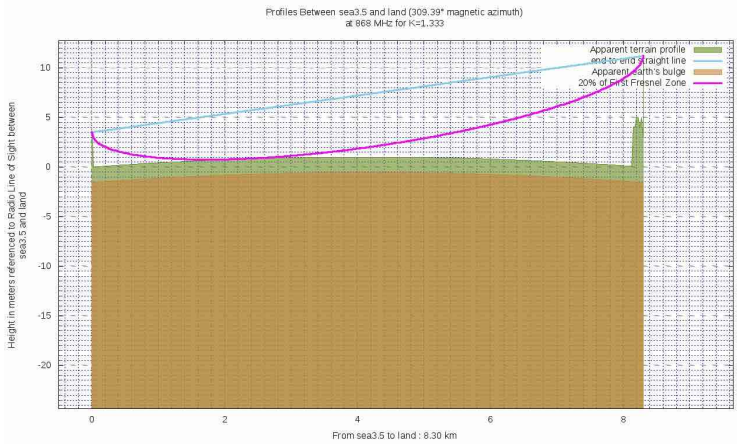

(a)

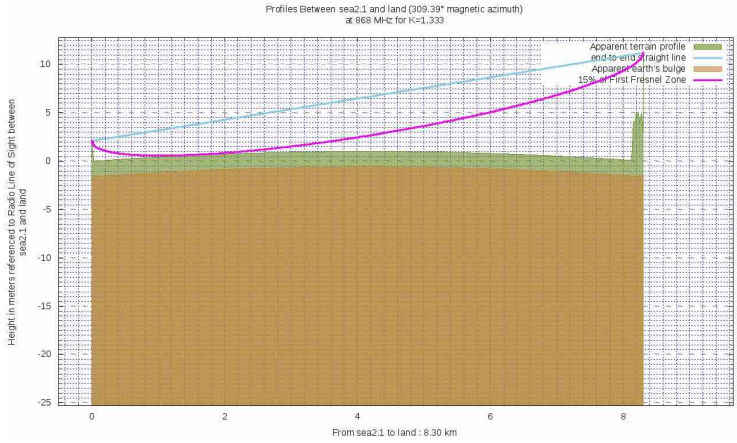

(b)

Figure 3.10: Estimates of the actual clearances for both the exploited altitudes for the transmitting antenna: (a) 20 % for $h_{TX_1} = 3.50\,\text{m}$; (b) 15 % for $h_{TX_2} = 2.10\,\text{m}$.

of some packets due to the inability of the gateways to restore corrupted data.

3.2.2 Second Short-Term Measurement Campaign

The second short-term measurement campaign was carried out by making use of the same prototype of the LoRaWAN network infrastructure of the first short-term measurement campaign (see Figure 3.5). Moreover, the same hardware for both the sensor node and the two gateways was exploited, and to limit the number of involved variables, the same spots for the transmitter and the receivers were adopted (see Figure 3.8). In addition, the sensor node and the gateways were installed in the same way as the first short-term measurement campaign. For the sake of readability, such measurement settings are repeated below.

The two gateways were ashore installed by establishing a space diversity scheme and by exploiting as installation site a knoll whose altitude is 6.00 m above sea level (see Figure 3.7). The receiver antennas, two directional helical ones whose gain was 14 dBi each, were mounted on a telescopic pole whose maximum height was 7.20 m. However, during the measurements shorter lengths of the pole were tested so to put into effect an increasing degradation of the link quality, especially because of the satisfactory results of the first short-term measurement campaign. Gateways and antennas were in turn connected to each other via two 15.00 m coaxial cables whose individual loss was 4.06 dB, and Internet connectivity was provided by a 4G LTE router.

A sensor node was offshore set up in point A of Figure 3.8. The B-L072Z-LRWAN1 discovery kit board was connected to a directional Yagi-Uda, antenna whose gain was 9 dBi (see Figure 3.6a), by employing a 4.00 m long coaxial cable whose loss was 2.10 dB, in order to install the antenna at the altitude of 2.10 m above sea level. Directional antennas were chosen for both the end-points so to enhance the link strength since it took place in a harsh environment as the sea.

The sensor node sent packets exploiting a power of 14 dBm and respecting the laws on the temporal occupancy of the exploited ISM band (i.e., devices have to respect a duty cycle of $1\,\%$): this temporal constraint limited the overall number of transmitted packets. Measurements were split into 4 groups (namely, $\#1$, $\#2$, $\#3$ and $\#4$). Group $\#1$ was the replica of the last group of the first short-term measurement campaign: 6 SFs were employed (i.e., $7, 8, \ldots, 12$), 50 packets per SF were sent and the receiver antennas were elevated at a total height, which includes the ones of the knoll and pole, of 13.20 m above sea level. Since this set of trials proved to be effective once again, for the remaining ones only $SF = 7$ was tested because, at least theoretically, it is the one having the worst performances in long distance links. Group $\#2$ was characterized by a worse quality of the channel since the gateways antennas were lowered at a total altitude of 9.95 m above sea level. For groups $\#3$ and $\#4$ the receiver antennas were further lowered down at a height of 8.30 m above sea level. Moreover, in group $\#4$ the transmitter antenna was rotated of 180° along the axis of its mounting pole thus pointing towards the opposite

direction than before. In doing so, the transmitter and the receiver antennas had an orientation mismatch of the main lobes. Groups $\#2$, $\#3$ and $\#4$, 50 packets were sent, therefore an amount of 450 packets was broadcast throughout the trials, spending a total time of 8 h. All the packets were transmitted exploiting a bandwidth of 125 kHz and, in order to model a worst case, a $CR = 4/5$ was employed. Moreover, a test string of 51 B as packet payload was sent. Finally, all these setups are listed in Table 3.4.

Table 3.4: Summary of the tests setup for the second short-term measurement campaign.

Transmission Technology	Group	h_{TX} [m]	h_{RX} [m]	P_{TX} [dBm]	SFs	CR	Sent Packets	Orientation Mismatch
LoRaWAN	$\#1$	2.10	13.20	14	$7-12$	$4/5$	300	✗
	$\#2$		9.95		7		50	✗
	$\#3$		8.30					✗
	$\#4$							✓

3.3 Results and Discussion

3.3.1 First Short-Term Measurement Campaign

At first, each of the test groups will be examined in detail. Then, a general analysis on the whole first short-term measurements campaign will be provided. A commonly examined outcome is the percentage of received packets and a solution to augment such a rate is to decrease the CR because some of the missing packets could be so due to the inability to restore corrupted data at the receiver side. However, the maximum CR was selected for both the measurements campaigns so as to implement a worst case scenario.

Hereinafter, the RSSIs and the SNRs will be analysed, for each SF and for each test trial, by modelling them as discrete random variables. Indeed, the gateways sample those quantities in a discrete fashion. In particular, the RSSIs take values in the set

$$\mathcal{R} = \{-137, -136, \ldots, -1, 0\}$$

where the elements of $\mathcal{R}$ are expressed in dBm, while the SNRs take values in the set

$$\mathcal{S} = \{-20.0, -19.9, \ldots, 19.9, 20.0\}$$

where the elements of $\mathcal{S}$ are expressed in dB. Since the measured RSSIs at the gateways side can be considered as the power of the received signals, a comparison between the values of RSSIs that were recorded during the tests and the value of P_{RX} reported in

Table 3.3 can be accomplished. The former ones were lower than the latter due to either the limited clearance of the first Fresnel zone (see Figure 3.10) and to the fact that the sea behaves as a huge ground plane because of the salinity of the water. Such phenomena cause a difference between the theoretical values and the measured ones of slightly more than 20 dB. However, this did not notably affect the performance of the wireless communication link. Along with those variables, also the percentage of the received packets for each SF for each test group will be evaluated.

The characteristics of measurements belonging to group $\#1$ are reported in Table 3.2. During this setup, 262 packets out of the 300 transmitted were received (i.e., the $87.33\,\%$). Table 3.5 reports the mean values, the standard deviations of the RSSIs and SNRs and the number of received packets out of 50 for each SF. It can be noticed that the maximum mean values for RSSIs and for SNRs were respectively observed for $SF = 10$ (i.e., $\bar{x}_{RSSI} = -97.1$ dBm), and for $SF = 9$ (i.e., $\bar{x}_{SNR} = 9.19$ dB). However, due to the minimum difference between the mean RSSIs of $SF = 7$ and $SF = 10$ and since the standard deviation associated to the former is less than the one of the latter, it is reasonable to claim that $SF = 7$ was the most suitable SF during this measurements setup. Figures 3.11–3.14 in turn show the RSSI Probability Mass Function (PMF), the RSSI temporal trend, the SNR PMF and the SNR temporal trend dividing them by SF. Regarding the latter two, some negative SNRs can be spotted underlining the capability of LoRa to demodulate heavy noisy signals. Focusing on Figures 3.12 and 3.14, a lack of values in the horizontal axis can be noticed. This is due to the fact that their purpose is just to display how the RSSIs and the SNRs varied during the tests. Since this test group turned out to be successful, it was chosen to worsen the link by lowering down the transmitting antenna to h_{TX_2} (see Table 3.2) for the next sets of trials.

Table 3.5: Experimental results from group $\#1$ of the first short-term measurement campaign in which 50 packets were transmitted for each SF.

SF	$\bar{x}_{RSSI}$ [dBm]	s_{RSSI} [dB]	$\bar{x}_{SNR}$ [dB]	s_{SNR} [dB]	Received Packets
7	-97.8	1.4	7.60	3.33	45
8	-100.3	3.0	7.92	4.06	47
9	-100.0	1.9	9.19	3.94	43
10	-97.1	1.8	9.17	3.25	44
11	-98.8	2.5	9.19	4.31	40
12	-99.4	1.6	7.12	4.33	43

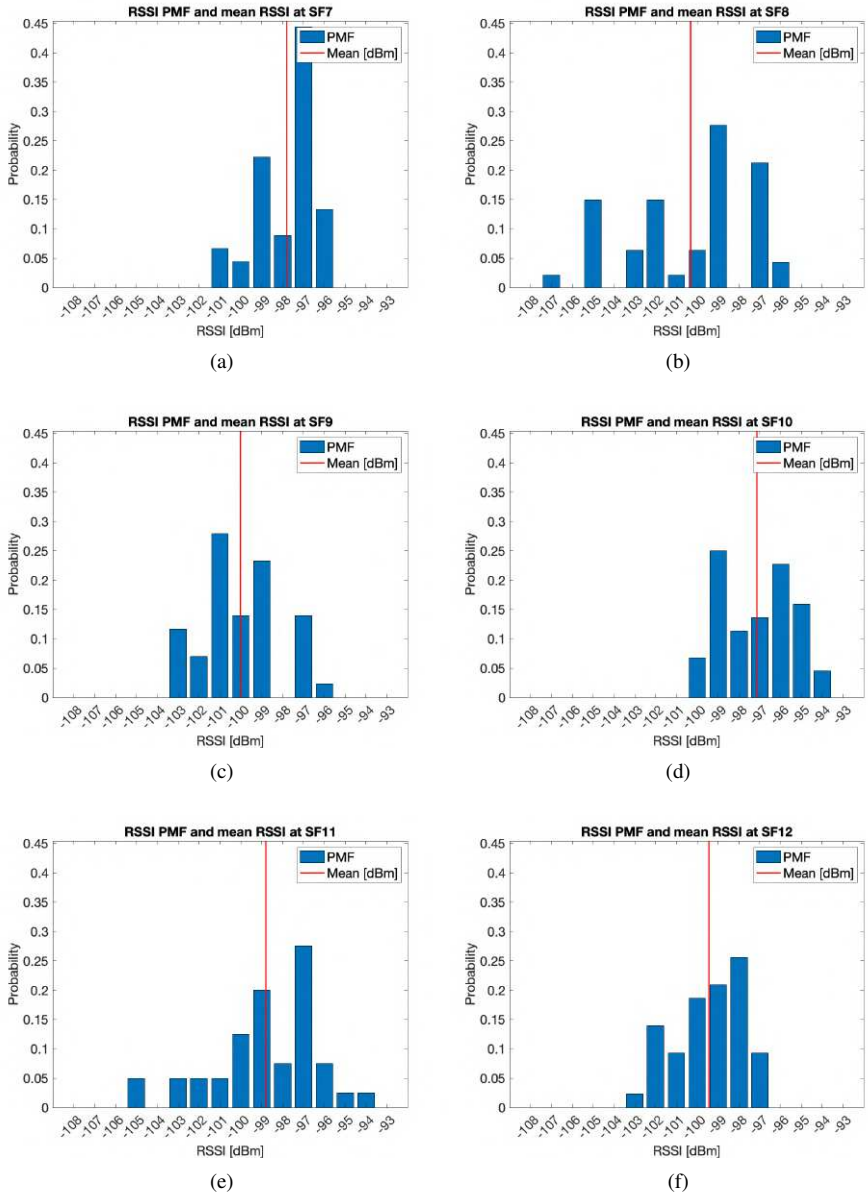

Figure 3.11: Group #1 RSSIs PMFs for the first short-term measurement campaign: (a) $SF = 7$; (b) $SF = 8$; (c) $SF = 9$; (d) $SF = 10$; (e) $SF = 11$; (f) $SF = 12$.

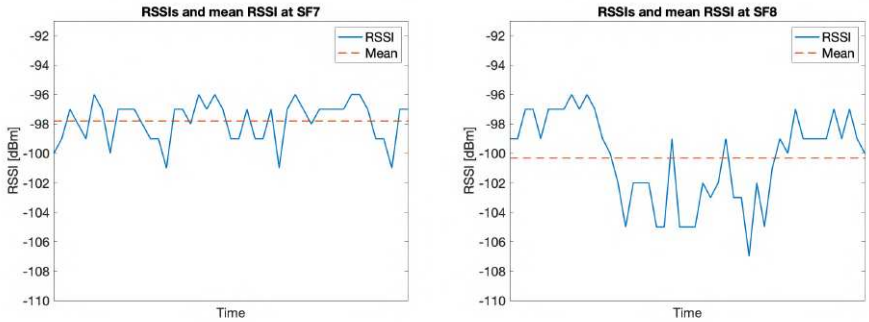

(a)

(b)

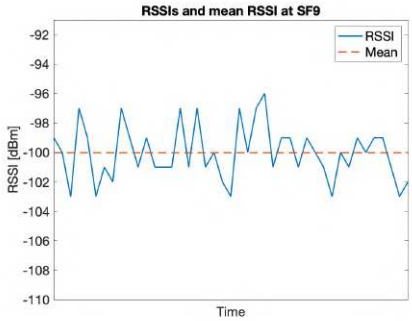

(c)

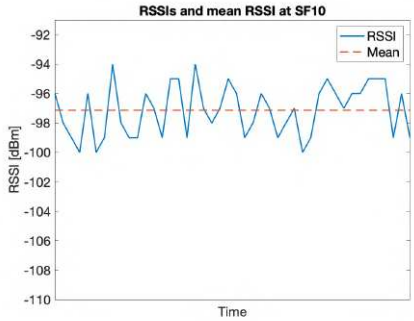

(d)

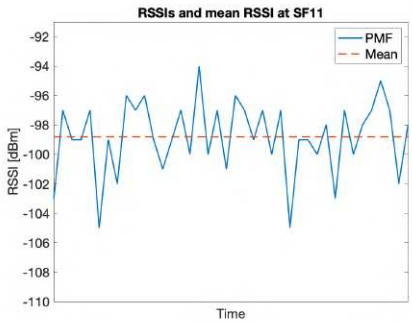

(e)

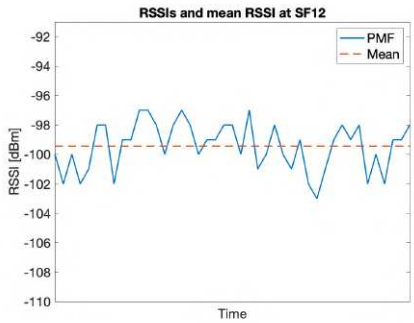

(f)

Figure 3.12: Group #1 RSSIs temporal trend for the first short-term measurement: (a) $SF = 7$; (b) $SF = 8$; (c) $SF = 9$; (d) $SF = 10$; (e) $SF = 11$; (f) $SF = 12$.

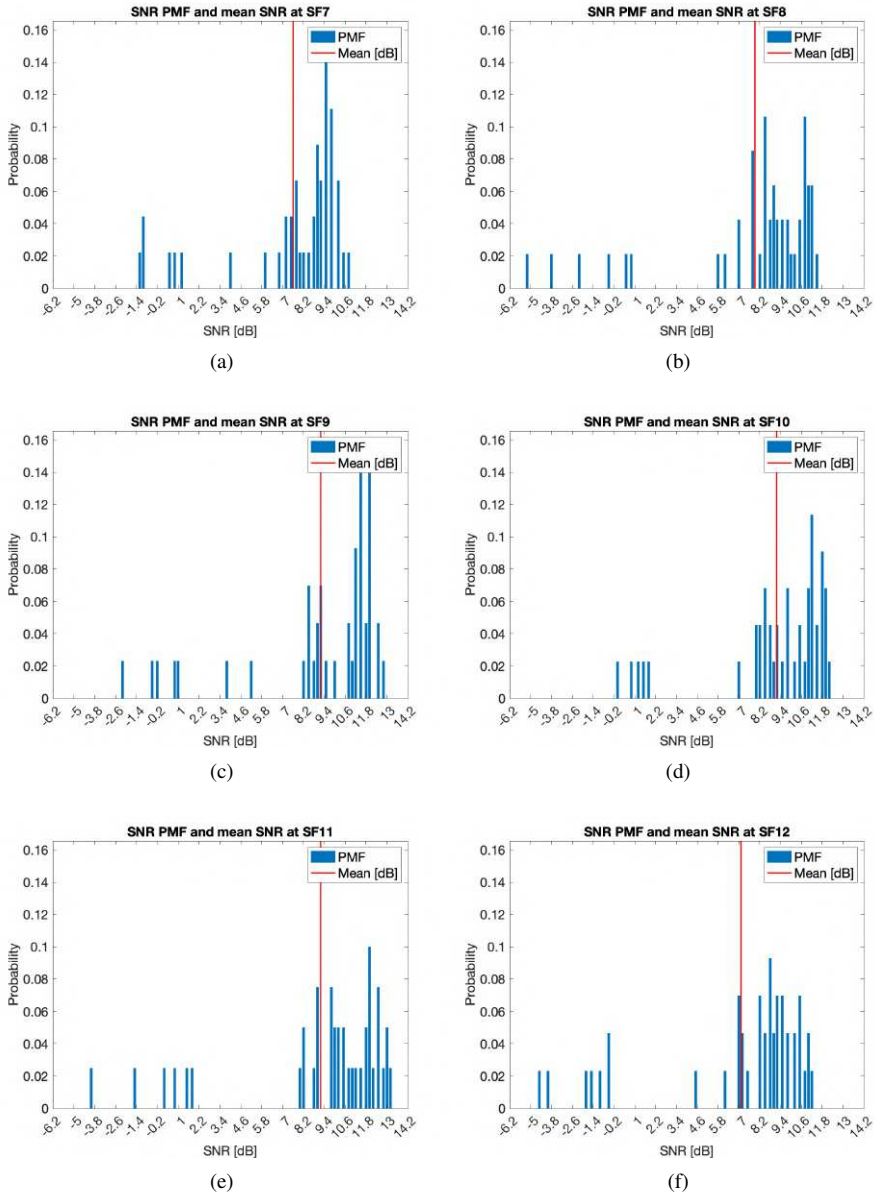

Figure 3.13: Group #1 SNRs PMFs for the first short-term measurement campaign: (a) $SF = 7$; (b) $SF = 8$; (c) $SF = 9$; (d) $SF = 10$; (e) $SF = 11$; (f) $SF = 12$.

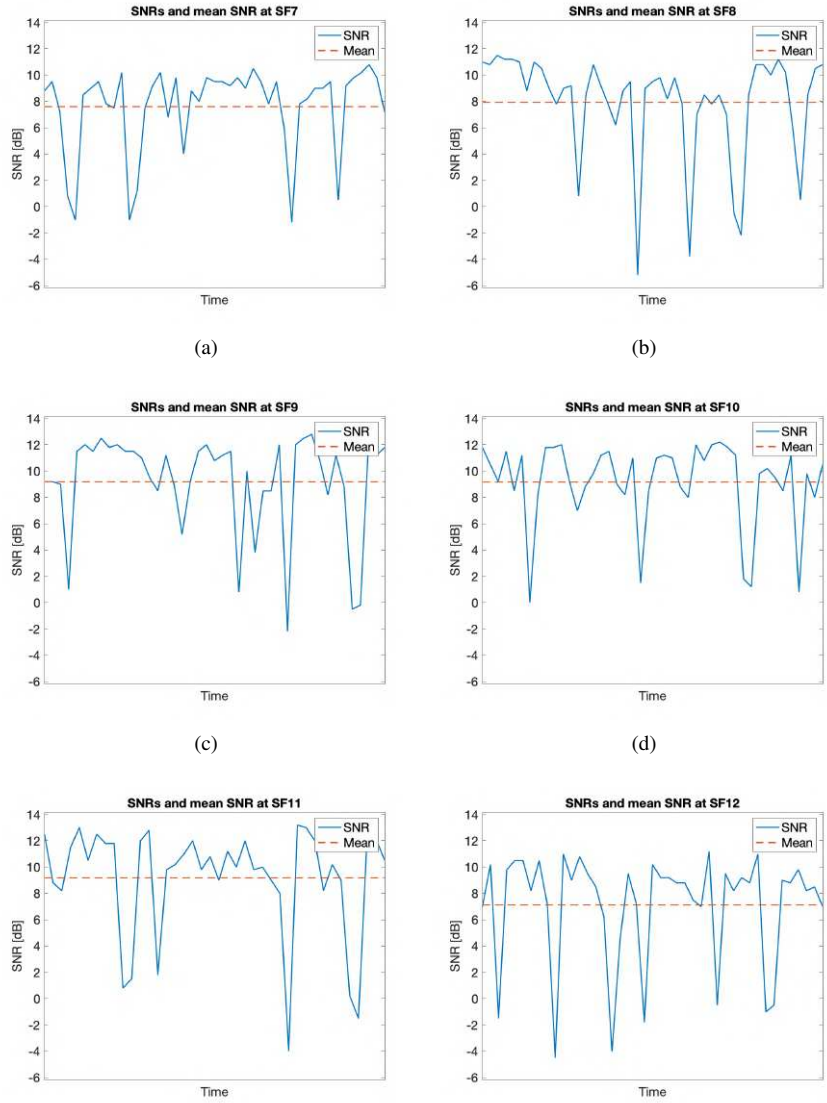

(a) (b)

(c) (d)

(e) (f)

Figure 3.14: Group #1 SNRs temporal trend for the first short-term measurement campaign: (a) $SF = 7$; (b) $SF = 8$; (c) $SF = 9$; (d) $SF = 10$; (e) $SF = 11$; (f) $SF = 12$.

The characteristics of measurements belonging to group $\#2$ are listed in Table 3.2. Throughout this group of experiments, 268 packets out of the 300 transmitted were received (i.e., the $89.33\,\%$). Table 3.6 outlines the mean values, the standard deviations of the RSSIs and SNRs and the number of received packets out of 50 for each SF. The best RSSI mean value was experienced for $SF = 7$ (i.e., $\bar{x}_{RSSI} = -100.7\,\text{dBm}$) while the best SNR mean value was observed for $SF = 11$ (i.e., $\bar{x}_{SNR} = 9.40\,\text{dB}$). However, because of the limited difference amid the mean RSSIs of $SF = 7$ and $SF = 8$ and due to the fact that the latter has the smallest standard deviation, it is plausible to assert that $SF = 8$ is the one having the best performances throughout this trial setup. Figures 3.15–3.18 respectively show the RSSI PMF, the RSSI temporal trend, the SNR PMF and the SNR temporal trend dividing them by SF. As it was averred for the analysis of group $\#1$, Figures 3.16 and 3.18 do not present any value in the horizontal axis since their purpose is just to visualise how the RSSIs and the SNRs varied during the tests. It can be seen that the number of the negative values for SNR was increased with respect to the ones belonging to group $\#1$.

Table 3.6: Experimental results from group $\#2$ of the first short-term measurement campaign in which 50 packets were transmitted for each SF.

SF	$\bar{x}_{RSSI}$ [dBm]	s_{RSSI} [dB]	$\bar{x}_{SNR}$ [dB]	s_{SNR} [dB]	Received Packets
7	-100.7	1.9	6.74	4.09	46
8	-102.0	1.4	7.72	4.45	45
9	-104.2	3.1	7.25	5.28	46
10	-102.0	2.3	7.59	4.41	43
11	-101.5	2.1	9.40	3.59	46
12	-101.5	2.1	8.07	2.46	42

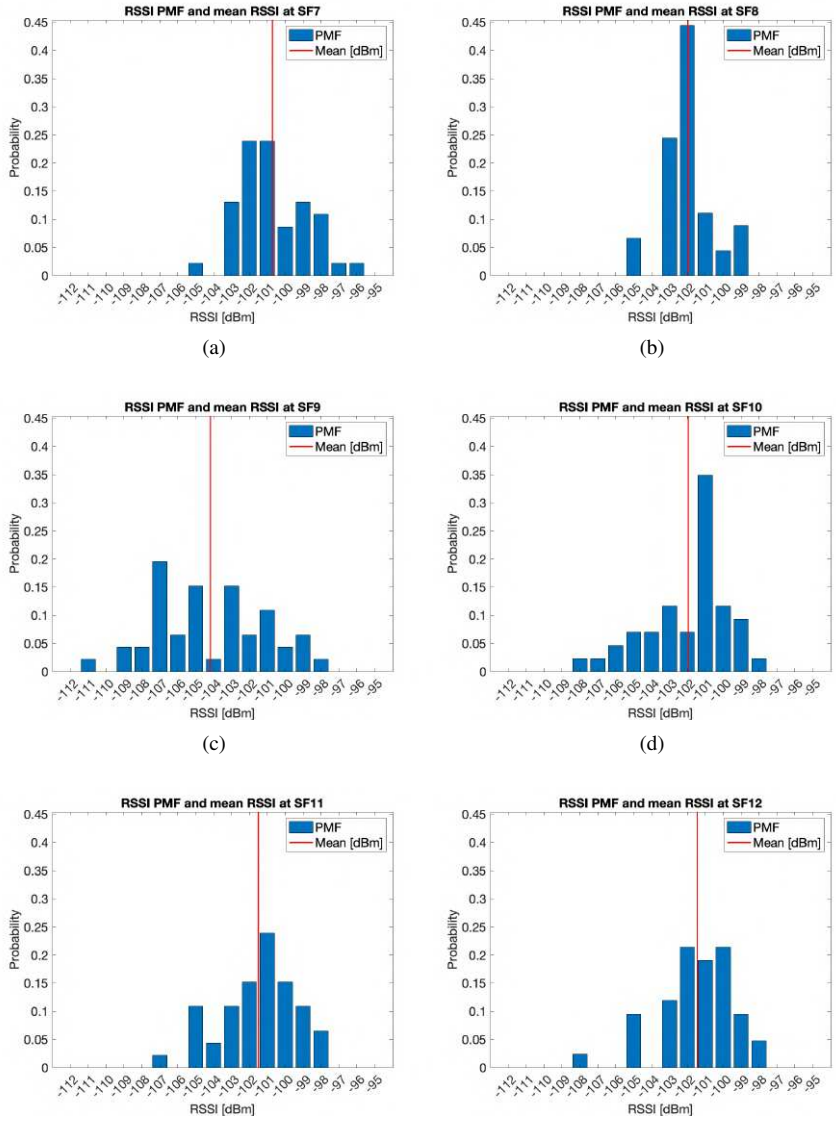

Figure 3.15: Group #2 RSSIs PMF for the first short-term measurement campaign: (a) $SF = 7$; (b) $SF = 8$; (c) $SF = 9$; (d) $SF = 10$; (e) $SF = 11$; (f) $SF = 12$.

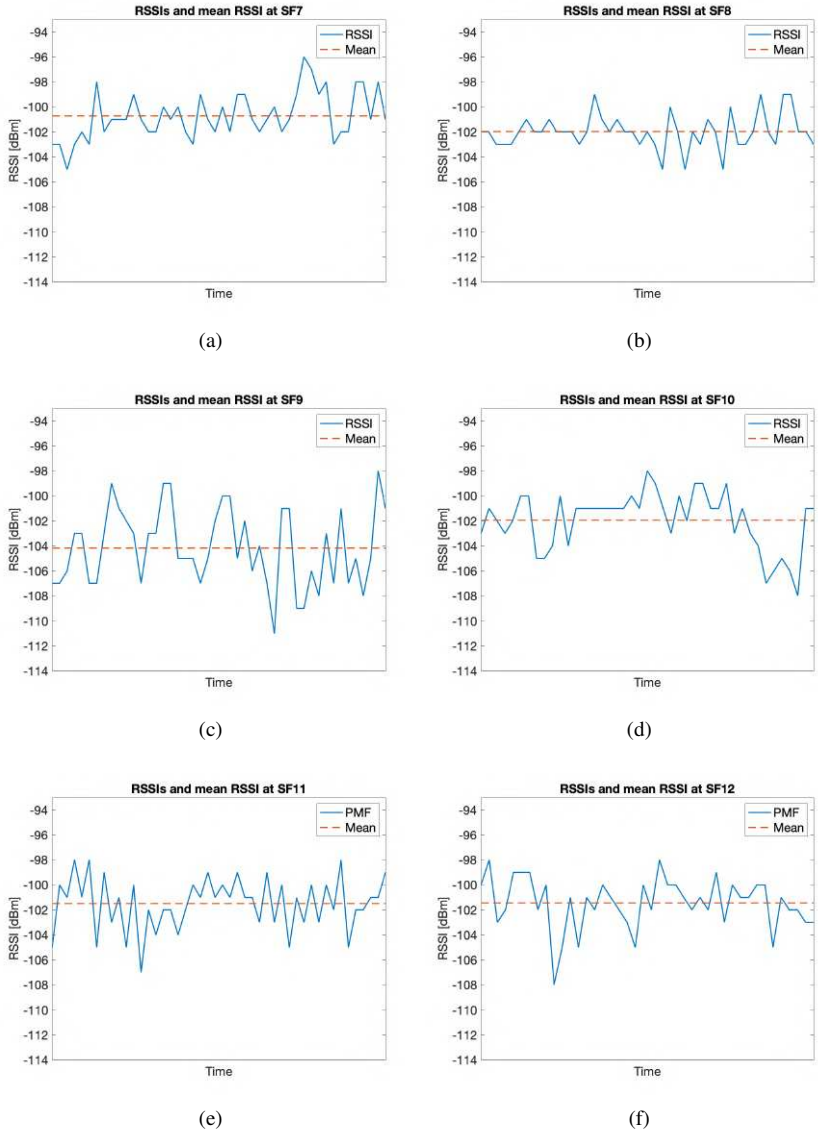

Figure 3.16: Group #2 RSSIs temporal trend of the first short-term measurement campaign: (a) $SF = 7$; (b) $SF = 8$; (c) $SF = 9$; (d) $SF = 10$; (e) $SF = 11$; (f) $SF = 12$.

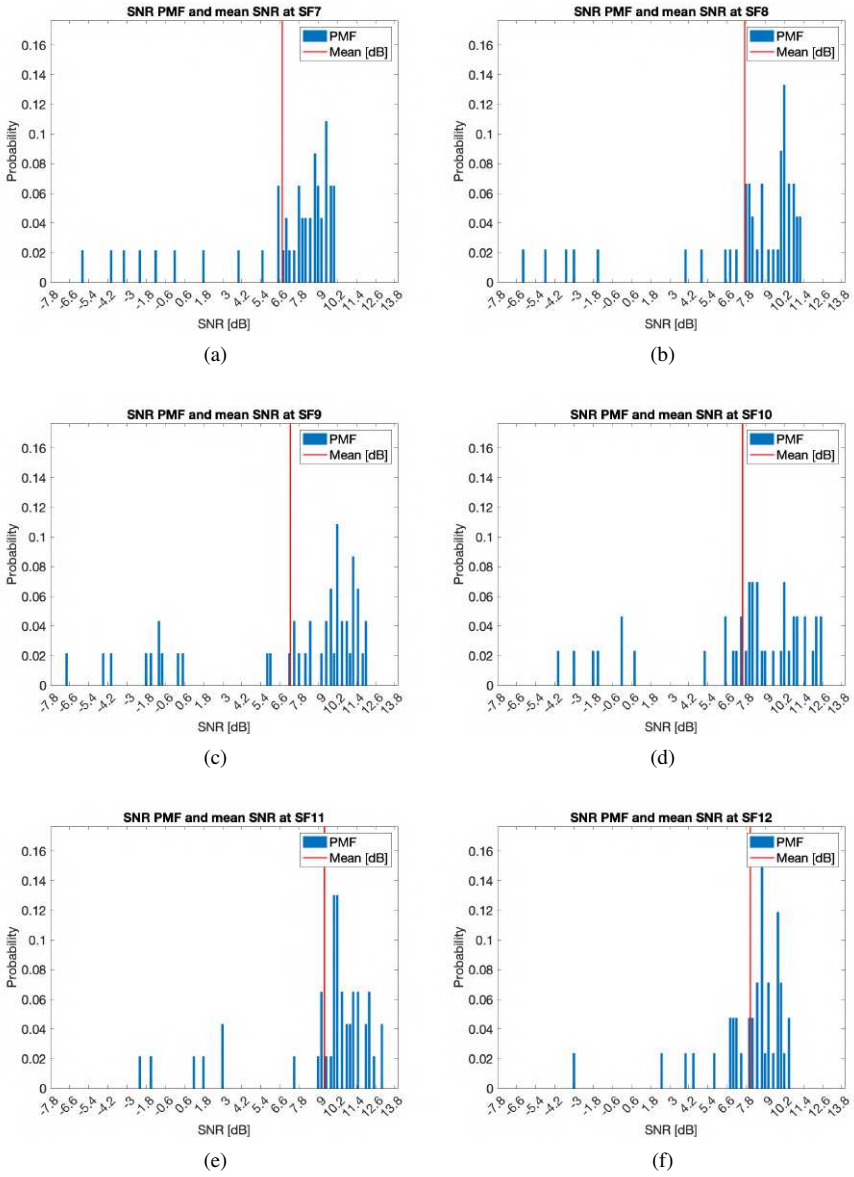

Figure 3.17: Group #2 SNRs PMFs of the first short-term measurement campaign: (a) $SF = 7$; (b) $SF = 8$; (c) $SF = 9$; (d) $SF = 10$; (e) $SF = 11$; (f) $SF = 12$.

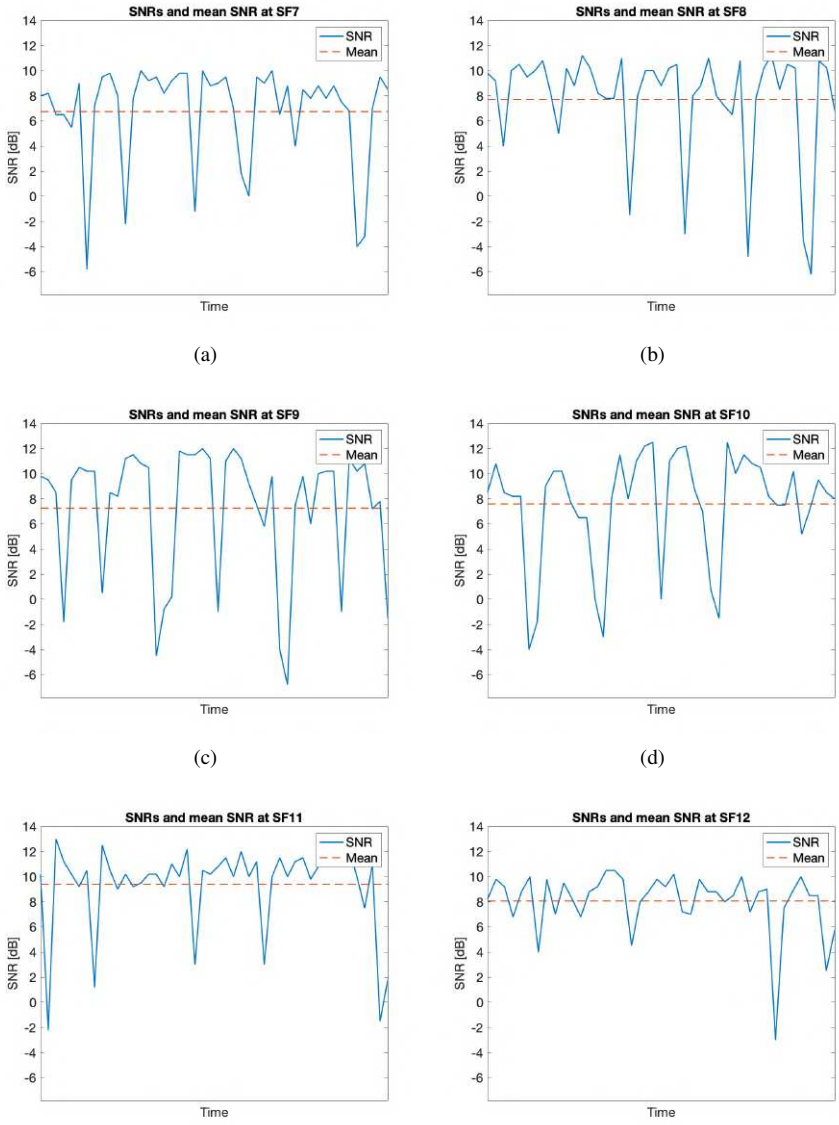

(a) (b)

(c) (d)

(e) (f)

Figure 3.18: Group #2 SNRs temporal trend of the first short-term measurement campaign: (a) $SF = 7$; (b) $SF = 8$; (c) $SF = 9$; (d) $SF = 10$; (e) $SF = 11$; (f) $SF = 12$.

With the aim of accomplishing a finer statistical analysis, it would have been necessary to collect a greater number of packets. However, the low data-rate and the limitations on the duty cycle due to the spectrum usage regulations hindered the measurements. Indeed, the limited number of transmitted packets could have caused notches in the plots related to SNR. These can be due to statistical fluctuations resulting from the fact that LoRa modulation intrinsically entails outliers and spurious values in terms of RSSI and SNR, that are much more evident whenever few packets are sent. Moreover, despite tests took place offshore and in a seasonal period in which maritime traffic in the testing site is moderate, sporadically some transmission occurred while other boats passed in the LoS degrading the channel, hence reducing SNR. In spite of it, the presented method and results could still be valuable to render insights into the potentialities of a LoRaWAN network to be employed in a marine environment. Indeed, for the purposes of the application scenario, the feasibility of the LoRaWAN communication ashore was successfully proven because of the total amount of 600 packets that were transmitted throughout the trial groups, 530 were correctly received and demodulated (i.e., roughly the $88.3\,\%$, which is similar to the results obtained in comparable tests sorted out in the same environments [56, 57]). Moreover, considering the distribution of the RSSIs, there was enough link margin (i.e., from $25.55\,\text{dB}$ at $SF = 7$ to $36.55\,\text{dB}$ at $SF = 12$ on average) to exploit worse wireless link setups. Some instances are further lowering down the antennas elevations thus reducing their installation complexity, or diminishing the transmitter power output thus augmenting the sensor node battery lifetime.

Due to the nature of the application scenario, a more complete analysis on the performance of the communication ashore would have been carried out by considering the behaviour of the system whenever different weather conditions, with respect to the one experienced during the measurement campaign, will have to be faced. As it was claimed earlier on, such trials were impossible to be actually analysed due to a logistical constraint associated with the adopted boat to reach point A (see Figure 3.8).

Nevertheless, significant path losses caused by meteorological events are not likely to be experienced by virtue of what is reported in the sixth chapter of Seybold book [52]. It presents several losses induced by atmospheric effects by showing their models and graphical representations to be taken into account during the design of a wireless link. Moreover, it also points out remedies. For instance, coastal and marine environments are particularly susceptible to fading due to atmospheric multipath and the preferred solution to mitigate such a shortcoming for fixed-length links is to establish an antenna diversity scheme. Hence, this strategy was adopted by employing two antennas at the receiver side.

Atmospheric attenuation due to gaseous absorption (e.g., oxygen and water vapour) is not significantly detrimental for sub-GHz wireless links. Indeed, Seybold [52] reports

plots showing the specific atmospheric attenuation of standard atmosphere and of dry air in function of the frequency for a horizontal path. In both the cases, the specific attenuation is less than 0.01 dB/km thus making it negligible for this application scenario. Apart from the gaseous one, there exist two forms of water that affect wireless propagation: precipitation (e.g, rain and snow), and suspended water droplets forming clouds and fog. Snow is directly related to the moisture content of the particles within the air but the effect of its attenuation is relatively smaller with respect to the one due to rain. The latter attenuation is deeply discussed in the tenth chapter of Seybold book [52] which concludes that the extent of this kind of loss is less than 0.01 dB/km for sub-GHz applications. On the other hand, clouds and fog rarely contribute to the detriment of a wireless link. Instead, they can slightly enhance communication since they can behave as waveguides. Similar considerations may be drawn for what concerns possible antennas orientation mismatches, due to the fact that the transmitting one is expected to be mounted on top of a seamark buoy. Since the first tests of the short-term measurement campaign were performed using a small dimensions boat with not perfect wave conditions, a certain degree of motion of the boat was present: nevertheless this did not significantly affect the performances of the link. While no analytical study was carried out due to the random nature of the movement of the boat, a set of tests with different angles of orientation is performed during the second short-term measurement campaign.

Figure 3.19 shows the comparison between the mean values and the associated standard deviations for the RSSIs and SNRs divided by SF and test groups. Furthermore, the same Figure displays the percentage of received packets split by SF and test trials. In light of the results derived from the first short-term measurement campaign, and despite it is not theoretically suitable for long distance links, $SF = 7$ is the most favourable SF to convey the sampled data from offshore towards ashore due to several reasons:

- Such a SF provided acceptable rates of received packets even though it was not the best one;
- In both groups $\#1$ and $\#2$ it turned out in having some of the best RSSI mean values and standard deviations, as well as satisfactory SNR statistics. While the differences among the RSSI values achieved using the different SFs can be attributed more to statistic fluctuations rather than to actual better performances, mostly due to the small number of transmitted packets, it is however possible to state that in the proposed conditions the performances of the six SFs are almost comparable, and do not suggest any particular choice in this sense;
- Its most important feature for the application scenario is that it is the SF ensuring

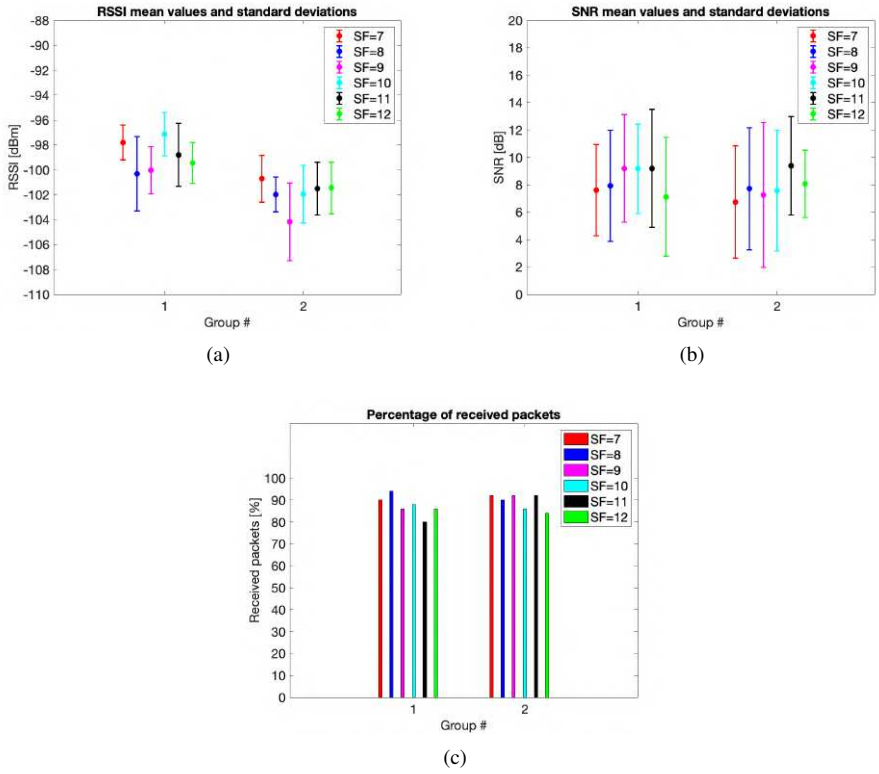

Figure 3.19: Group comparison graphical analysis divided by SFs for the first short-term measurement campaign: (a) RSSIs mean values and standard deviations; (b) SNRs mean values and standard deviations; (c) percentage of received packets.

the shortest ToA for the same packet length thus reducing power requirements.

3.3.2 Second Short-Term Measurement Campaign

The performances related to this set of trials were evaluated by examining means and standard deviations of RSSIs, Figure 3.20a, and SNRs, Figure 3.20b, along with received packets rate per SF and test group, Figure 3.20c. Moreover, they are listed in Table 3.7.

During group $\#1$, 278 packets out of 300 were correctly received (i.e., $92.67\,\%$) and the relative results were comparable with the ones obtained in the second group belonging to the first short-term measurement campaign. In groups $\#2$ and $\#3$ comparable rates of

Table 3.7: Summary of the tests results related to the second short-term measurement campaign.

Group	SF	Received Packets (%)	RSSIs ($\bar{x}$;s) [dBm; dB]	SNRs ($\bar{x}$;s) [dB; dB]
#1	7	45 (90 %)	(−101.9 ; 1.6)	(7.01 ; 3.99)
	8	48 (96 %)	(−100.5 ; 1.5)	(6.62 ; 4.65)
	9	48 (96 %)	(−103.5 ; 3.0)	(7.65 ; 4.58)
	10	42 (84 %)	(−103.9 ; 3.1)	(7.09 ; 5.61)
	11	49 (98 %)	(−101.6 ; 1.8)	(9.60 ; 3.19)
	12	46 (82 %)	(−100.4 ; 3.1)	(7.77 ; 2.76)
#2	7	44 (88 %)	(−108.3 ; 2.2)	(4.76 ; 3.46)
#3	7	47 (94 %)	(−107.1 ; 3.3)	(2.98 ; 5.78)
#4	7	24 (48 %)	(−116.4 ; 4.0)	(−4.43 ; 4.53)

received packets were experienced in comparison with the ones of group #1 even tough poorer RSSIs and SNRs statistics occurred. Finally, because of the antennas orientation mismatch, in group #4 a significant decrease of correctly received packets together with worse RSSIs and SNRs statistics were experienced. It has to be also noticed that a negative SNR mean value was recorded during group #4 thus confirming the robustness of LoRa modulation. In order to perform a finer statistical analysis, a larger number of data packets would have been required. Unfortunately, this was unfeasible due to the time constraint introduced by the slowness of the employed boat and by the duty cycle. However, the effectiveness over the sea of the LoRaWAN network prototype was once again proved since 393 packets out of 450 (i.e., 87.33 %) were correctly received. Furthermore, that rate could be improved if lower CRs were adopted since some packets losses may arise due to the inability of the gateways to restore corrupted data. In addition, a mean link margin of 13.66 dB at $SF = 7$ was recorded, hence suggesting that worse channel qualities may be exploited.

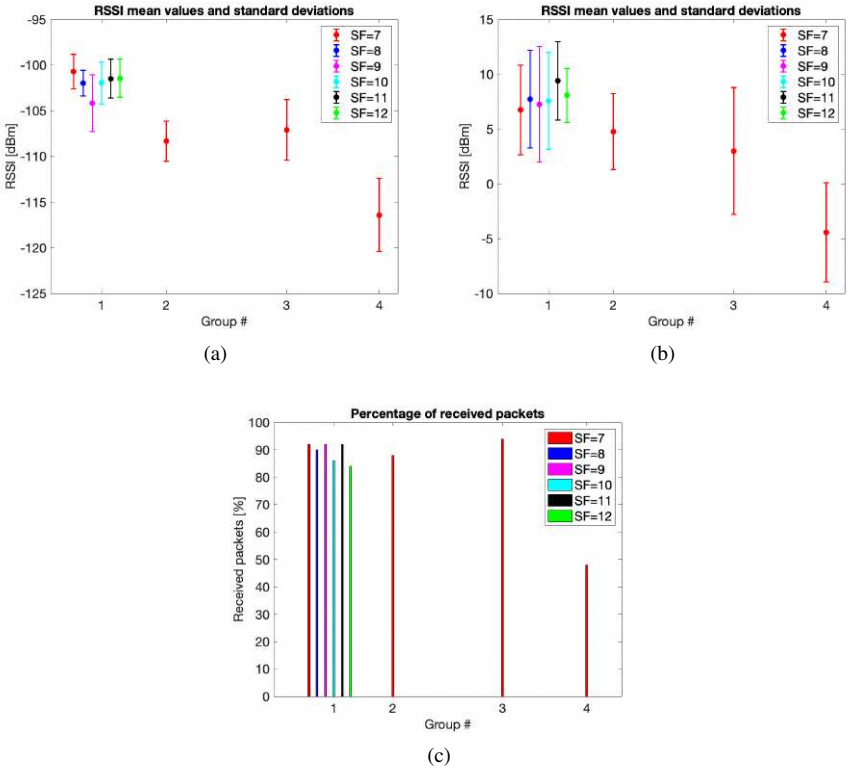

Figure 3.20: Second short-term measurements campaign results: (a) RSSIs means and standard deviations; (b) SNRs means and standard deviations; (c) received packets rates.

Chapter 4

Underground-to-Aboveground Links

4.1 Path Loss Model

Underground measurement systems, and WSNs in general, have been developed for years, giving birth to WUSNs, since the need of establishing pervasive monitoring infrastructures to be deployed in unreachable and hostile environments has become more and more compelling over time [58, 59]. Moreover, whenever the context of IoT is met, the brand-new paradigm of the Internet of Underground Things (IoUT) arises [60], which is currently paving the way for novel solutions for measuring, sampling and transmitting the extent of various phenomena, that take place underground, whose knowledge is required in order to actuate the most diverse operations either aboveground or underground (e.g., manage assets, predict occurrence of events, perform maintenance, schedule processes and so on). The design phases of such networks are notably more challenging with respect to the superficially deployed ones, due to the intrinsic attenuation properties of soil. To this end, several techniques for Underground-to-Underground (UG2UG), Underground-to-Aboveground (UG2AG), and Aboveground-to-Underground (AG2UG) transmissions have been devised in disparate contexts: oil and gas reservoirs [61], smart lighting systems [62], smart urban drainage systems [63], smart cities [64] and environmental monitoring [65] are only few instances although smart agriculture has taken a huge advantage from such technologies [66, 67, 68].

Wireless links in such infrastructures suffer from the intrinsic attenuation capabilities of soil, that mainly depend on soil composition, on the presence of metals in the soil, and on the amount of dissolved water in the soil. In particular, this quantity is also known as the Volumetric Water Content (VWC), and plays a key role within precision agriculture applications in order to optimise water resources and increase yields. Moreover, it is the main cause of attenuation in UG2AG links [69].

Many papers investigated electromagnetic waves propagation underground analysing dependencies on soil composition and VWC [70, 71, 72, 73] or estimating impulse response of such a medium [74]. Other studies performed evaluations on path loss related to underground wireless links [65, 66, 75, 76, 77, 78] and hereinafter a similar investigation

is conducted for UG2AG transmissions. For the sake of clarity, it is suggested to refer to the model in Figure 4.1.

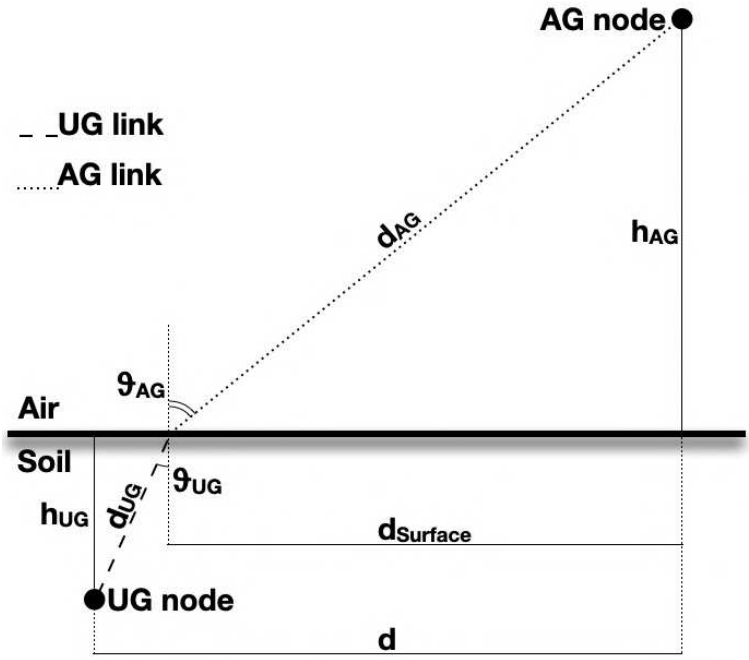

Figure 4.1: Channel model for UG2AG links, where d_{UG} is the path the signal covers underground, $d_{Surface}$ is the length of the soil-air interface, d_{AG} is the path the signal covers aboveground, h_{AG} is the height of the aboveground antenna, h_{UG} is the burial depth of the underground antenna, θ_{UG} and θ_{AG} are the incident angles at the point in which signals change the propagation medium.

Path loss can be calculated by modifying the Friis formula:

$$\begin{aligned} P_{RX} =& P_{TX} + G_{TX} + G_{RX} - L_{UG} - L_{UG-AG} + \\ & - 0.5(L_{AG} + L_{Surface}) - L_M - 10log_{10}(\chi^2) \end{aligned} \tag{4.1}$$

where P_{RX} is the RSSI, P_{TX} is the transmitted power output, G_{TX} is the transmitter antenna gain, G_{RX} is the receiver antenna gain, L_{UG} accounts for underground losses, L_{UG-AG} refers to refraction losses at the soil-air interface, L_{AG} represents aboveground losses, $L_{Surface}$ is the attenuation due to lateral waves (it is averaged with L_{AG}), and L_M refers to miscellaneous losses due to sundry possible sources (e.g., obstructions within the first Fresnel zone, antennas polarisation mismatch and so on) and due to the

fact that some of the conditions under which the Friis equation can be applied could not be met. Indeed, while the distance between the antennas can be far greater than the carrier wavelength for the most part of UG2AG transmissions, the transmitting and receiving antennas may have different polarisation and they can be probably misaligned. Moreover, due to the fact the transmitting antenna is buried underground, unobstructed free space hypothesis can never be satisfied. Finally, $10log_{10}(\chi^2)$ is the path loss due to multi-path fading phenomenon.

The aboveground losses L_{AG} may be calculated as free space loss (see Equation 3.5). On the other hand, L_{UG} may be computed as [78, 79] suggest:

$$L_{UG} = 6.4 + 20log_{10}(d_{UG}) + 20log_{10}(\beta) + 8.69\alpha d_{UG} \tag{4.2}$$

where d_{UG} is the path the signal covers underground expressed in m, α is the attenuation constant and β is the phase shifting constant. The former two terms may be evaluated as

$$\alpha = 2\pi f \sqrt{\frac{\mu_0 \mu_r \epsilon_0 \epsilon^{'}}{2} \left[\sqrt{1 + \left(\frac{\epsilon^{''}}{\epsilon^{'}} \right)^2} - 1 \right]}, \tag{4.3}$$

$$\beta = 2\pi f \sqrt{\frac{\mu_0 \mu_r \epsilon_0 \epsilon^{'}}{2} \left[\sqrt{1 + \left(\frac{\epsilon^{''}}{\epsilon^{'}} \right)^2} + 1 \right]} \tag{4.4}$$

in which f is the carrier frequency, μ_r is the relative magnetic permeability of soil, that can be approximated as 1 supposing that the soil composition is metal-free, while $\epsilon^{'}$ and $\epsilon^{''}$ are in turn the real and imaginary part of the effective soil permittivity that can be computed as [80] suggests. In particular, they can be evaluated by resorting to the Mineralogy-Based Soil Dielectric Model (MBSDM) [81] which is valid within the range $0.045 - 26.5$ GHz. It requires as inputs the VWC (V), the carrier frequency and the percentage of clay (C) related to soil composition. In doing so, the real and imaginary part of soil permittivity (i.e., $\epsilon^{'}$ and $\epsilon^{''}$) are derived from the refractive index n and the normalised attenuation coefficient k as follows:

$$\epsilon^{'} = n^2 - k^2; \tag{4.5}$$

$$\epsilon^{''} = 2nk; \tag{4.6}$$

$$n = \begin{cases} n_d + (n_b - 1)V & if\ V < V_m \\ n_d + (n_b - 1)V_m + (n_f - 1)(V - V_m) & else \end{cases}; \tag{4.7}$$

$$k = \begin{cases} k_d + k_b V & if\, V < V_m \\ k_d + k_b V_m + k_f (V - V_m) & else \end{cases} \tag{4.8}$$

where $n_{d,b,f}$ is the refractive index respectively of dry soil, bound and free water; $k_{d,b,f}$ is the normalised attenuation coefficient in turn of dry soil, bound and free water; V_m is the maximum bound free water fraction used to distinguish the two moisture regions (i.e., bound and free water). These quantities are evaluated according to:

$$n_d = 1.634 - 0.539 \times 10^{-2} C + 0.2748 \times 10^{-4} C^2; \tag{4.9}$$

$$k_d = 0.03952 - 0.04038 \times 10^{-2} C; \tag{4.10}$$

$$n_{b,f}\sqrt{2} = \sqrt{\sqrt{(\epsilon_{b,f}^{'})^2 + (\epsilon_{b,f}^{''})^2} + \epsilon_{b,f}^{'}}; \tag{4.11}$$

$$k_{b,f}\sqrt{2} = \sqrt{\sqrt{(\epsilon_{b,f}^{'})^2 + (\epsilon_{b,f}^{''})^2} - \epsilon_{b,f}^{'}}; \tag{4.12}$$

$$V_m = 0.02863 + 0.30673 \times 10^{-2} C \tag{4.13}$$

where $\epsilon_{b,f}$ are the complex dielectric values for bound and free water respectively, that can be computed as:

$$\epsilon_{b,f}^{'} = \epsilon_\infty + \frac{\epsilon_{0b,0f} - \epsilon_\infty}{1 + (2\pi f \tau_{b,f})^2}; \tag{4.14}$$

$$\epsilon_{b,f}^{''} = \frac{\epsilon_{0b,0f} - \epsilon_\infty}{1 + (2\pi f \tau_{b,f})^2} 2\pi f \tau_{b,f} + \frac{\sigma_{b,f}}{2\pi f \epsilon_0} \tag{4.15}$$

where $\epsilon_\infty = 4.9$ is the dielectric constant in the high frequency limit, $\epsilon_{0b,0f}$ are low frequency limit of the dielectric constant of bound and free water and in particular $\epsilon_{0f} = 100$, $\tau_{b,f}$ are the relaxation time of bound and free water and in particular $\tau_f = 8.5 \times 10^{-12}$, while $\sigma_{b,f}$ are the conductivity respectively of bound and free water. Finally, the remaining parameters can be evaluated as follows:

$$\epsilon_{0b} = 79.8 - 85.4 \times 10^{-2} C + 32.7 \times 10^{-4} C^2; \tag{4.16}$$

$$\tau_b = 1.062 \times 10^{-11} + 3.450 \times 10^{-14} C; \tag{4.17}$$

$$\sigma_b = 0.3112 + 0.467 \times 10^{-2} C; \tag{4.18}$$

$$\sigma_f = 0.3631 + 1.217 \times 10^{-2} C. \tag{4.19}$$

Alternatively, the real and imaginary part of soil permittivity may be computed by resorting to the methods and equations presented by the International Telecommunication Union (ITU) in [82]. In particular, for what concerns soils, such model requires the carrier

frequency, the temperature, the percentages of both sand and clay, the Specific Gravity (SG) (i.e., the mass density of the soil sample divided by the mass density of the amount of water in the sample), the VWC and the Bulk Density (BD) of the soil samples.

Refraction losses occurring at the soil-air interface are computed as

$$L_{UG-AG} \simeq 10log_{10}\left[\frac{(\sqrt{\epsilon'}+1)^2}{4\sqrt{\epsilon'}}\right], \tag{4.20}$$

while the attenuation due to lateral waves is

$$L_{Surface} = 40log_{10}(d_{Surface}), \tag{4.21}$$

where $d_{Surface}$ is the distance of the soil-air interface propagation.

Lastly, χ is a random variable accounting for path losses due to multi-path fading having a Rayleigh distribution

$$f(\chi) = \frac{\chi}{\sigma_R^2} e^{-\frac{\chi^2}{2\sigma_R^2}} \tag{4.22}$$

where $\sigma_R = \sqrt{\frac{2}{\pi}}$ is the distribution parameter.

Due to the higher soil permittivity, in comparison with the one of the air, reflected and refracted signals are incident to soil surface. In other words, only signals having small incident angle θ_{UG} are able to emerge towards the surface. Hence, especially for UG2AG links, signals propagate vertically trough the soil allowing the approximation $\theta_{UG} \simeq 0$ entailing $d_{UG} \simeq h_{UG}$ (i.e., the burial depth h_{UG}), and $d_{AG} = \sqrt{d^2 + {h_{AG}}^2}$.

4.2 Measurement Setup

Wireless measurement infrastrucutures set up in the underground suffer from the intrinsic attenuation capabilities of soil. As it was shown in Section 4.1, such detrimental effect mainly depends on soil composition and VWC. Therefore, the tests presented in the following sections aim at investigating both the contribution of those elements, and the overall effectiveness of a wireless measurement system, enabled by LoRaWAN or NB-IoT technologies, deployed in such contexts. Some of these tests considered reception parameters (i.e., RSSIs and SNR) as metrics, while some others only focus on losses due to the medium (i.e., the soil at hand). UG2AG links were tested by making use of two different transmission technologies: LoRaWAN and NB-IoT. Moreover, the tests were firstly sorted out in laboratory, in the first place just for the LoRaWAN protocol, and then accounting for both the aforementioned technologies. Secondly, field tests for LoRaWAN

links were accomplished. Finally, the effect of VWC on UG2AG links was additionally studied by means of a laboratory campaign.

4.2.1 Preliminary Laboratory Measurement Campaign for LoRaWAN Links

The aim of this measurement campaign was to test and analyse performances of UG2AG LoRaWAN transmissions. Therefore, the prototype of the LoRaWAN network infrastructure of Figure 3.5 was exploited, where the sensor node is a minimal IoUT one. It featured a microcontroller (i.e., an ATtiny84 produced by Microchip) driving a LoRa transceiver (i.e., an RFM95 produced by HopeRF embedded in a breakout board produced by Adafruit) that were both powered by a battery pack (i.e., 4 AA lithium batteries providing $6\,\mathrm{V}$ and $4800\,\mathrm{mAh}$) passing through a $5\,\mathrm{V}$ voltage regulator (i.e., a µA7805 produced by Texas Instrument).

4.2.1.1 Antenna Selection Tests Setup

The transceiver antenna was selected according to a dedicated set of tests. Indeed, the IoUT sensor node needed a small antenna, so to fit inside the node enclosure, as well as a suitable one, so to fulfil transmissions. Hence, tests whose target was to select the best antenna amid the available ones, namely A_1, A_2, A_3 and A_4 (see Figure 4.2), were set up. Antennas typologies and gains are listed in Table 4.1.

Table 4.1: Antennas typologies and gains for the LoRaWAN IoUT sensor node. Gain values are declared by the antennas manufacturers.

Antenna	Type	Gain [dBi]
A_1	$\lambda/4$ Dipole	1.2
A_2	$\lambda/4$ Whip	1
A_3	$\lambda/8$ Whip	2
A_4	$\lambda/2$ Whip	2

The most suitable one was selected according to the following procedure: for each antenna, 3 SFs were tested (i.e., 7, 9 and 12); for each SF, 200 LoRaWAN packets having a payload of $51\,\mathrm{B}$ were broadcast to the gateway. In order to speed up these tests, the transmitter was not buried underground. Indeed, the gateway and the node were placed indoor within a five floors building with plenty of rooms, walls and electromagnetic noise since most of them hosted scientific laboratories. Moreover, the gateway was placed

Figure 4.2: Employed antennas during the tests for antenna selection for the LoRaWAN IoUT sensor node. From top to bottom: A_1, A_2, A_3 and A_4.

on the third floor while the node on the last one by exploiting two spots at the opposite corners of the building. A distance of approximately 100 m was covered in which none of the packets were lost. Finally, RSSIs and SNRs were measured by the gateway and analysed. Table 4.2 summarises the test settings.

Table 4.2: Summary of the settings related to the test aiming at selecting the antenna.

Transmission Technology	**P_{TX}**	**SFs**	**CR**	**Payload**	**# Packets**	**Distance**
LoRaWAN	14 dBm	7, 9, 12	$4/5$	51 B	200 for each SF and antenna	100 m

4.2.1.2 Short-Term Measurement Campaign

Finally, the IoUT sensor node was housed within an IP56 box so to protect it during underground trials. The microcontroller run a firmware implementing a LoRaWAN end device (i.e., a Class A device) sending packets to a gateway on a periodic basis establishing a frequency diversity scheme amid 8 different channels in the 868 MHz ISM band. The LoRaWAN gateway was implemented by means of a Raspberry Pi 3 model B driving a RAK831 produced by RAKWireless (i.e., a multi-channel LoRaWAN

(a) (b)

Figure 4.3: The LoRaWAN IoUT sensor node 50 cm underground during the preliminary laboratory measurement campaign for LoRaWAN links.

concentrator). The gateway had a sensitivity which varied depending on the SF spanning from -137 dBm at SF$=12$ up to -126 dBm at SF$=7$. It behaved as a packet forwarder, hence it firstly received and demodulated LoRaWAN packets and then it sent such data to a remote network server exploiting the MQTT protocol. The network server was specifically designed and implemented by making use of Node-RED. It managed all the incoming packets and stored all the related data (e.g., payloads) and metadata (e.g., RSSIs and SNRs) in a MySQL database.

Concerning UG2AG tests, two groups were set up. During the first one, the gateway was equipped with a directional helical antenna having a gain of 14 dBi, while during the last one a $\lambda/2$ whip antenna having a gain of 1 dBi (i.e., A_4 of Figure 4.2) was exploited for the gateway. Both the groups of tests shared the methodology: the IoUT sensor node was tested at 10 cm, 20 cm, 30 cm, 40 cm and 50 cm underground (see Figure 4.3) by sending 1000 LoRaWAN packets at SF$=7$ having a 33 B payload for each burial depths. The transmitter power output, the CR and the bandwidth of the transmitted packets were in turn set to 14 dBm, $4/5$ and 125 kHz for both the groups of tests. Then, RSSIs, SNRs and Packet Losss (PLs) were analysed. Table 4.3 summarises the test settings.

Table 4.3: Summary of the settings related to the short-term measurement campaign.

Transmission Technology	P_{TX}	SF	CR	Payload	# Packets	Burial Depth
LoRaWAN	14 dBm	7	4/5	33 B	1000 for each burial depth	10 cm, 20 cm, 30 cm, 40 cm, 50 cm

4.2.2 Preliminary Laboratory Measurement Campaign for LoRaWAN and NB-IoT Links

With the aim of comparing LoRaWAN and NB-IoT techonologies in such application scenario, a sensor node capable of transmitting by employing both the technologies was realised (see Figure 4.4).

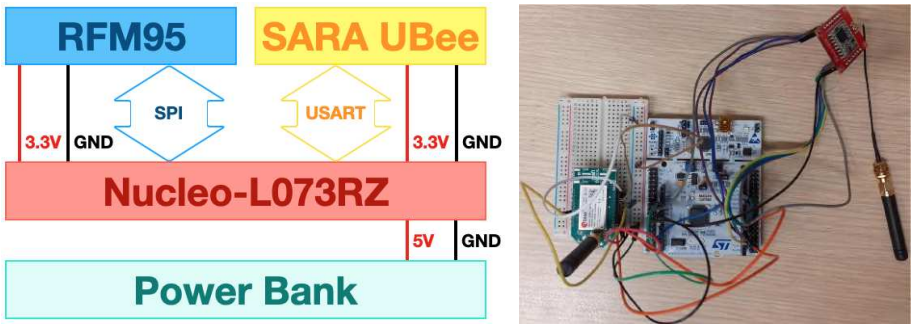

(a) (b)

Figure 4.4: Multi-protocol wireless sensor node prototype: (a) block diagram, (b) prototype without the power bank.

The core was a Nucleo-L073RZ board produced by STMicroelectronics: it is a general purpose development board embedding an STM32L073 microcontroller. The latter simultaneously drove a LoRaWAN transceiver (i.e., the RFM95 produced by HopeRF) via Serial Peripheral Interface (SPI), and an NB-IoT transceiver (i.e., the SARA UBee produced by Sodaq) via the Universal Synchronous and Asynchronous Receiver-Transmitter (USART) interface. The Nucleo board was powered via a power bank, while the communication modules were both powered by the Nucleo board. The microcontroller implemented a Class A LoRaWAN device which was fully capable of transmitting towards the prototype of LoRaWAN network infrastructure of Figure 3.5.

Figure 4.5: Tests setup for the preliminary laboratory measurement campaign for LoRaWAN and NB-IoT links.

LoRaWAN transmissions were put into effect by establishing a frequency diversity scheme via a frequency hopping technique amid 8 different channels belonging to the $863 - 870$ MHz ISM band. Finally, LoRaWAN packets, containing a 10 B test string as payload, were broadcast by setting SF$= 7$, bandwidth of 125 kHz and CR$= 4/5$, so to test a worst case scenario, and by exploiting a $\lambda/8$ whip antenna having 2 dBi gain in view of the antennas selection tests introduced before. The NB-IoT transceiver was controlled via AT commands by the microcontroller. At first, it executed all the needed routines to join the network, and then it broadcast packets exploiting the MQTT protocol. MQTT messages contained an incremental counter and the relative RSSI of the signals the eNodeB sent back to the sensor node during synchronisation procedures. Transmissions took place within the $863 - 870$ MHz band via a $\lambda/8$ whip antenna having 2 dBi gain. Such antenna was selected exploiting the results of the antennas selection tests.

In this measurement campaign, aiming at assessing performances of both the technologies in underground settings, only losses occurring in the medium were taken as reference. Such task was fulfilled by firstly sorting out a set of 300 transmissions for both the technologies in parallel by placing the prototype at open air and by measuring

and storing the RSSIs. Then, the same number of broadcasts were performed by putting the prototype underground. Afterwards, losses were calculated by subtracting RSSIs from the first set of measurements to each of the following one. Therefore, any losses due to factors which are not related to the critical environment could be neglected. At last, experimental losses were compared to the estimated ones by resorting to the models previously shown (see Section 4.1). Concerning LoRaWAN, RSSIs were measured by the same gateway presented in the short-term measurement campaign of Section 4.2.1.2 that was placed 35 m apart from the sensor node prototype. Such distance was chosen because of logistical constraints related to the availability of mains for powering the gateway. On the other hand, RSSIs of NB-IoT links were retrieved by subscribing to the same MQTT topic on which the sensor node posts MQTT message by making use of a computer. Unfortunately, the distance between the prototype and the various eNodeBs employed during the tests cannot be known. However, this was not an issue at all since only losses taking place underground were considered. Finally, such tests were performed by firstly digging into the soil (see Figure 4.5), then housing the prototype within an IP56 box and burying it. Concerning soil properties, it was composed by $8.86\,\%$ of gravel, $65.09\,\%$ of clay and $26.05\,\%$ of sand: such analysis was carried out by resorting to the sedimentologic scales put forth by Wentworth [83] (it will be described in detail later on). Finally, the soil had a BD of $1.43\,\mathrm{g/cm^3}$, a VWC of $35.42\,\%$ (that was measured by means of a gravimetric analysis), while for SG, the value of 2.56 was considered according to [84]. Lastly, the multi-protocol sensor node was buried 10 cm, 30 cm and 50 cm underground, respectively. Table 4.4 summarises the test settings.

Table 4.4: Summary of the settings related to the comparative measurement campaign accounting for LoRaWAN and NB-IoT.

Transmission Technology	SF	CR	Payload	# Packets	Burial Depth
LoRaWAN	7	$4/5$	10 B	300 for each burial depth	10 cm, 30 cm, 50 cm
NB-IoT	–	–	10 B	300 for each burial depth	10 cm, 30 cm, 50 cm

4.2.3 Field Measurement Campaign

UG2AG LoRaWAN links were additionally tested in the field. To this end, the IoUT sensor node was implemented by means of the B-L072Z-LRWAN1 discovery kit board

produced by STMicroelectronics. It basically embeds an STM32L072CZ microcontroller manufactured by STMicroelectronics and an SX1276 LoRa transceiver constructed by Semtech along with miscellaneous electronics. Concerning its power supply, a power bank was employed, while transmissions were carried out by exploiting a $\lambda/8$ whip antenna having 2 dBi gain, as it was suggested by the results of the tests on antennas selection, that was directly connected to the B-L072Z-LRWAN1 discovery kit board via a SubMiniature version A (SMA) connector. Finally, the IoUT sensor node and its antenna were housed within an IP56 box so to protect them during underground trials. The microcontroller run a firmware implementing a LoRaWAN end device (i.e., a Class A device) sending packets to a gateway on a periodic basis establishing a frequency diversity scheme amid 8 different channels in the $863 - 870$ MHz ISM band (i.e., 867.1 MHz, 867.3 MHz, 867.5 MHz, 867.7 MHz, 867.9 MHz, 868.1 MHz, 868.3 MHz and 868.5 MHz). Once again, the prototype of the LoRaWAN network infrastructure of Figure 3.5 was employed. However, concerning the gateway, an LG308 produced by Dragino was adopted. It had the same hardware included by the RAK831, that are two SX1257 (i.e., LoRa transceivers) and one SX1301 (i.e., a LoRa modem), both produced by Semtech. The gateway had a sensitivity which varied in function of the SF and the exploited bandwidth for the transmissions. Supposing to employ a bandwidth of 125 kHz, the gateway sensitivity spanned from -137 dBm at SF$=$ 12, to -126 dBm at SF$=$ 7. During the tests, it was equipped with the same antenna as the one of the sensor node (i.e., a $\lambda/8$ whip antenna having 2 dBi gain). It behaved as a packet forwarder, hence it firstly received and demodulated LoRaWAN packets, it measured both the associated RSSIs and SNRs, and then it sent such data to a remote network server exploiting the MQTT protocol.

4.2.3.1 Soil Analysis

Three deposits were selected in the surroundings of the city of Siena, Italy, for such field tests. In particular, the main difference was represented by the grain-size, which significantly differed from sample to sample and accounted for different behaviours and properties (e.g., angle of repose, packing, permeability, organic matter content, etc). Therefore, three samples constituted by gravel, sand and clay respectively, as representative of pure soils, were selected. From a geological point of view, such choice made sense because they exemplified the three main grain-size classes in which sedimentologic scales are classified (e.g., Wentworth scale [83]). Nonetheless, it was also useful because the vast majority of agricultural soils are usually composed of a combination of such grain-size classes. This means that the knowledge about the behaviour of pure soils would help in predicting the behaviour of mixed soils.

The first two samples were collected from an emerged longitudinal bar along the

Merse river bed, near Siena, Italy (i.e., samples Merse #1 and Merse #2). Due to the strong flows that typically characterise such a stream, the deposits were expected to be characteristically devoid of fine particles ($< 63\,\mu$m), which would be easily washed away with no chance of deposition in such environment. As the sampling site along the river was located far from the alluvial plain, the river still maintained the flow characteristics of a mountain creek. Gravel accumulations were easily spotted along the riverbed, as well as sand deposits. The clay sample was collected further downstream, in a site characterized by frequent floods over the natural levee. Such alluvial deposits are usually constituted by finer particles, as coarser sediments can hardly be transported past the levee even during flooding events.

The sedimentological characterisation of the three samples was carried out to calculate the traditional parameters that best define the main properties of sediments. Such parameters are mean and sorting [85], and the percentage of coarse (> 2 mm, gravel), medium (from 2 mm to $63\,\mu$m, sand) and fine ($< 63\,\mu$m, clay) fractions. Mean corresponds to the average grain-size of the sample; sorting describes the heterogeneity of the grain-sizes comprised in the sample. Percentage of coarse, medium, fine fractions is the proportion between the main populations of sediment grain-sizes in accordance with the Wentworth scale [83]. About 1 kg of sediment was sampled from the selected sites, collecting with a small shovel the surface of the deposits. The laboratory analysis was carried out in accordance with the technique described in [86]. No further characterisation of the finest population was done. The resulting data (see Table 4.5) were processed with an Excel macro named Granu, which enabled the calculation of the textural parameters.

Table 4.5: Results of the sedimentological analysis performed on the three samples relative to the field measurement campaign.

Sample	**Mean [mm]**	**Sorting [Φ]**	**Coarse Fraction (Gravel) [%]**	**Medium Fraction (Sand) [%]**	**Fine Fraction (Clay) [%]**
Merse #1	7.126	1.500	86	14	0
Merse #2	0.922	0.734	5	95	0
Certosa	0.056	0.545	3	7	90

The results of the grain-size analysis confirmed the expectations, as the first two samples (i.e., Merse #1 and Merse #2) presented no fine fraction, and varying content of coarse and medium fractions. The coarser one (i.e., Merse #1) was characterized by 86 % of gravel and pebbles, which translated into a 7.126 mm mean grain-size. Merse #2 was almost entirely constituted by sand (i.e., 95 %), with a mean grain-size of 0.922 mm

(i.e., medium sand). Though the percentage of sand was almost $100\,\%$, the sorting was moderately poor (i.e., 0.734), meaning that Merse #2 sample included very fine to very coarse sands. Merse #1 sorting was poor, as expected in a sample characterized by such proportions of coarse and medium fractions. The Certosa sample confirmed the provenance from the "Crete Senesi" deposit, as the mean grain-size was enough below the $63\,\mu$m threshold between fine and medium particles (i.e., $0.056\,$mm); predictably, such sample was very well sorted (i.e., 0.545).

Following the sedimentological characterisation, a gravimetric analysis was carried out on soil samples to measure their VWC and BD. In particular, soil samples were collected at 3 depths (i.e., $10\,$cm, $30\,$cm, and $50\,$cm): since differences among these depths were very small, intermediate values may be easily derived by interpolation. Moreover, the limited difference did not justify for a finer gravimetric analysis that took into account other depths in between the considered ones. A picture of the 9 soil samples after gravimetric analysis can be seen in Figure 4.6: from left to right shown samples were respectively Merse #2, Merse #1 and Certosa, and samples were displaced according to their pick depth starting from $10\,$cm at the bottom and $50\,$cm at the top.

Figure 4.6: Soil samples coming from the sites of the field measurement campaign, used for the gravimetric analysis: from left to right, Merse #2, Merse #1, and Certosa; from top to bottom their pick depth, $10\,$cm, $30\,$cm, and $50\,$cm.

Concerning the gravimetric analysis, as soon as the 9 samples were collected, they were placed in a container of known weight and volume V_{tot} and then weighted with a scale featuring a $\pm 0.001\,$g of accuracy. The samples were then put inside an oven, at a temperature of $105\,^{\circ}$C: then, their weight was checked every $12\,$h. When the difference

among two consecutive measurements was lower than 0.01 g the samples were assumed to be dry. VWC and BD were calculated applying the following formulas:

$$VWC = \frac{V_{water}}{V_{tot}} = \frac{m_{wet} - m_{dry}}{\rho_{water} V_{tot}}; \tag{4.23}$$

$$BD = \frac{m_{dry}}{V_{tot}}; \tag{4.24}$$

where m_{wet} is the mass of wet soil and m_{dry} is the mass after being dried in the oven, while water density ρ_{water} was assumed as equal to 1 g/cm^3. Concerning the SG, this was not measured since standard values can be found in literature [84], notice that variations according to different soil compositions are very small: therefore, for sand and gravel soils an SG of 2.66 was chosen, while an SG of 2.56 was considered for clay. All the values can be seen in Table 4.6, where all the measured data are presented.

Table 4.6: Results of the gravimetric analysis performed on the three samples coming from the sites of the field measurement campaign.

Measurement	**Sample**	**Burial Depth [cm]**		
		10	**30**	**50**
VWC [%]	Merse #1	7.15	9.35	9.74
	Merse #2	5.67	6.37	7.26
	Certosa	28.8	31.14	29.99
BD [g/cm^3]	Merse #1	1.45	1.54	1.39
	Merse #2	1.23	1.20	1.22
	Certosa	1.28	1.45	1.34
SG	Merse #1	2.66	2.66	2.66
	Merse #2	2.66	2.66	2.66
	Certosa	2.56	2.56	2.56

Once that the soils were identified and analysed, tests on UG2AG transmissions were carried out. In particular, the following factors were taken into account while defining the experimental setup:

- The possible RSSI degradation in long lasting operations due to the soil compaction;
- The different achievable results when placing the receiver at different distances from the transmitter;
- The attenuation due to different salinity levels in soil.

Figure 4.7: Compacted soil surface after node burial for the test assessing the impact of soil compaction on RSSIs.

For what concerns the first point, a test was carried out so to demonstrate the lack of influence of soil compaction on RSSI. Regarding the other two points, these were faced when defining the final experimental setup for the field tests.

4.2.3.2 Soil Compaction Effect on RSSI Tests Setup

The test aiming at demonstrating that the actual compaction of soil has no impact on the RSSI is crucial to show the validity of the data collected during the field tests since these were performed with the node buried under a layer of soil manually compacted, and by starting the data acquisition phase immediately after the node burial, without the need of waiting for the soil compaction. Therefore, such test was carried out burying a node in a soil characterized by a mixed composition: sedimentological analysis results for this soil pointed out that it was made by a $9\,\%$ of gravel, $26\,\%$ of sand and $65\,\%$ of clay while it had a mean of 0.112 mm and a sorting of $2.0\,\Phi$. Such a composition was chosen in order to detect possible attenuation contribution for every kind of soil since the sample has a sundry makeup. Moreover, since the aim of this test was only to detect possible decreases in the RSSI due to soil composition, a single SF was chosen for all the transmissions (i.e., SF $= 12$): indeed, RSSI is not dependent on the SF which, on the other hand, has a notable impact on PL because it decreases the receiver sensitivity. Similarly, no particular assumption was made for what concerns soil salinity and distance from transmitter and

Figure 4.8: The IoUT sensor node during the field measurement campaign. Ropes were used to ease the node retrieval.

receiver: in particular, the gateway was indoor placed at a $27.00\,\mathrm{m}$ distance from the transmitter. Such distance was measured using a measurement tape with $\pm 0.1\,\mathrm{cm}$ of accuracy, however considering the complexity in taking a correct measurement because of the logistical constraints in maintaining the tape taut, an accuracy of $\pm 2\,\mathrm{cm}$ can be assumed. The node was buried at a $30\,\mathrm{cm}$ depth and covered by paying attention at compacting the soil (Figure 4.7 shows the compacted soil surface after node burial), and then kept in transmission for 20 days, with a transmission rate of 1 packet every $20\,\mathrm{min}$.

4.2.3.3 Field Tests Setup

Field tests were carried out in the three sites described before: Figure 4.8 shows the IoUT sensor node during the burial depth measurement phase, just before its covering in soil,

within gravel soil. Such tests were performed bearing in mind the following assumptions:

- The sites where chosen in a fluvial environment, in order to reduce as much as possible the attenuating effects due to salinity, since fluvial soils are characterised by negligible salinity levels;
- For each soil, tests were performed at 5 burial depths (i.e., 10 cm, 20 cm, 30 cm, 40 cm, and 50 cm). No tests were performed at greater depths since a large part of significant underground monitoring applications are deployed at a maximum depth of 50 cm: for instance, in works like [87, 88, 89, 90, 91] that dealt with various application scenarios (i.e., smart farming, smart agriculture, pipeline monitoring and underground monitoring in a broad sense), sensor nodes were not buried at bigger depths;
- For each of the trials the soil was thoroughly compacted to uniform soil density after the node burial. Such procedure was performed just in order to reduce the number of involved variables, albeit it does not affect communication performances (as it will be seen later on);
- Concerning the radio settings, a power output of 14 dBm, a CR of $4/5$ and a bandwidth of 125 kHz were chosen. For what concerns the SF, since this parameter is crucial to identify the best trade off among PL and power consumption, tests were performed at each SF allowed by LoRaWAN protocol (i.e., from 7 to 12);
- The gateway was placed at a 15.00 m distance from the burial point and laid on the ground for each measurement. This distance was chosen in order to add a relatively short aboveground transmission distance, thus better identifying the link budget component for the underground segment of the transmission. The tests were not performed at other distances due to the fact that transmission performances at different distances can be easily assessed taking into account the behaviour of LoRaWAN networks in air, which was discussed in a wealth of papers like [92, 93, 94, 95].

For what concerns data acquisition, the following methodology was sorted out:

- 300 packets having a 10 B payload were sent at each of the burial depths (i.e., 10 cm, 20 cm, 30 cm, 40 cm, and 50 cm), for each SF (i. e., 7, 8, 9, 10, 11, and 12);
- For each of the received packets, the RSSI and SNR values were sampled and stored;

Table 4.7: Summary of the settings related to the field measurement campaign for LoRaWAN UG2AG links.

Transmission Technology	P_{TX}	SFs	CR	Payload	Soil Type	# Packets	Burial Depth
LoRaWAN	14 dBm	7, 8, 9, 10, 11, 12	$4/5$	10 B	Gravel, Sand, Clay	300 for each burial depth and soil type	10 cm, 20 cm, 30 cm, 40 cm, 50 cm

- For each of the test groups (i.e., 300 transmissions for a certain SF at a certain depth and within a certain soil) the PL was calculated.

Finally, Table 4.7 summarises the test settings.

4.3 Results and Discussion

4.3.1 Preliminary Laboratory Measurement Campaign for LoRaWAN Links

4.3.1.1 Antenna Section Tests Results

Tests results relative to the antenna selection for the IoUT sensor node are reported in Table 4.8 and in Figure 4.9.

Table 4.8: Antenna selection for the LoRaWAN IoUT sensor node test results: RSSIs and SNRs mean values and standard deviations.

	RSSI ($\bar{x}$ [dBm], $\bar{s}$ [dB])						SNR ($\bar{x}$ [dB], $\bar{s}$ [dB])					
	SF=7		SF=9		SF=12		SF=7		SF=9		SF=12	
	$\bar{x}$	s	$\bar{x}$	s	$\bar{x}$	s	$\bar{x}$	s	$\bar{x}$	s	$\bar{x}$	s
A_1	-88	2	-89	3	-81	3	8.9	1.1	11.0	1.6	10.4	1.9
A_2	-87	2	-88	3	-85	2	8.8	1.7	11.4	2.1	8.4	2.3
A_3	-84	3	-82	3	-80	2	9.2	0.9	11.6	1.8	9.8	1.6
A_4	-88	3	-91	3	-88	3	8.2	3.4	10.9	2.0	8.6	2.6

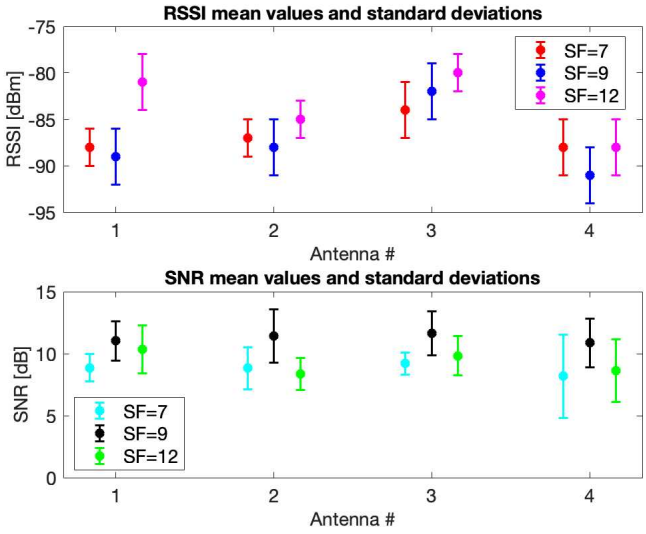

Figure 4.9: Antennas selection for the LoRaWAN IoUT sensor node tests results: RSSIs and SNRs mean values and standard deviations.

All the antennas had comparable performances. However, A_3 was selected since it was the smallest one. Moreover, it had the best RSSI statistics. Such result may be justified by statistical fluctuations due to the limited number of samples rather than actual better performances. In addition, since similar outcomes were experienced, SF$=7$ was chosen for the preliminary laboratory measurement campaign for LoRaWAN links since it is the one ensuring the shortest ToA supposing to send a fixed amount of data, and thus the one requiring the minimum quantity of energy.

4.3.1.2 Short-Term Measurements Campaign Results

Let us apply the model described in Section 4.1. Since the IoUT sensor node implemented a frequency diversity scheme, the mean value of the frequencies of the channels (i.e., $867.8\,\text{MHz}$) will be involved in all the equations. The gateway was placed indoor (pointing towards the field within which the node was buried) in front of a window at the second floor of a building at a distance d_{AG} of $27.00\,\text{m}$, that was measured with a tape, from the interred sensor node. The measuring tape had a resolution of $1\,\text{mm}$, and the associated measurement uncertainty can be estimated in $\pm 10\,\text{mm}$ owing to the intrinsic logistical complexity in keeping the tape taut while measuring because of the position of the gateway (i.e., indoor at the second floor). Therefore, from Equation 3.5, L_{AG} is

Table 4.9: Results of Equations 4.3 and 4.4 exploiting the values of $\epsilon^{'}$ and $\epsilon^{''}$ reported by Peplinski [96] in the best and worst cases.

	$\epsilon^{'}$ [F/m]	$\epsilon^{''}$ [F/m]	α [1/m]	β [rad/m]
Best Case	4.30	0.25	1.10	37.73
Worst Case	17.00	1.80	3.96	75.09

Table 4.10: RSSIs estimates for all the tests of the preliminary laboratory measurement campaign for LoRaWAN links from the IoUT sensor node by applying the model in Section 4.1 in best case and worst case.

	RSSI estimates [dBm]			
Burial	**Group #1**		**Group #2**	
Depth [cm]	$G_{RX} = 14$ **dBi**		$G_{RX} = 1$ **dBi**	
	Best Case	**Worst Case**	**Best Case**	**Worst Case**
10	−48.74	−57.20	−61.74	−70.20
20	−55.72	−66.66	−68.72	−79.66
30	−60.19	−73.63	−73.19	−86.63
40	−63.65	−79.57	−76.65	−92.57
50	−66.54	−84.95	−79.54	−97.95

equal to 59.85 dB. The real and imaginary parts of the effective soil permittivity were retrieved from results of Peplinski [96] that were derived by tests on four types of soil, which differed for the composition, by varying the VWC. Indeed, the mixture of the soil in which the IoUT sensor node was buried was not known, apart from the fact that it was metal-free, and no instrumentation for measuring the real and imaginary parts of the effective soil permittivity was available. In order to proceed with the analysis, values of $\epsilon^{'}$ and $\epsilon^{''}$ related to the best case and to the worst case, according to [96], were considered. In particular, the higher the VWC, the worse the case: best one is represented by VWC of 5 %, while worst one by VWC of 20 %. Thus, the values fetched from Peplinski [96] and the results from Equations 4.3 and 4.4 are delivered in Table 4.9.

Hence, by resorting to Equations 4.1, 3.5, and 4.2, the estimates of the RSSIs for all the tests are reported in Table 4.10. On the other hand, underground transmission results are shown in Figure 4.10 and in Tables 4.11 and 4.12.

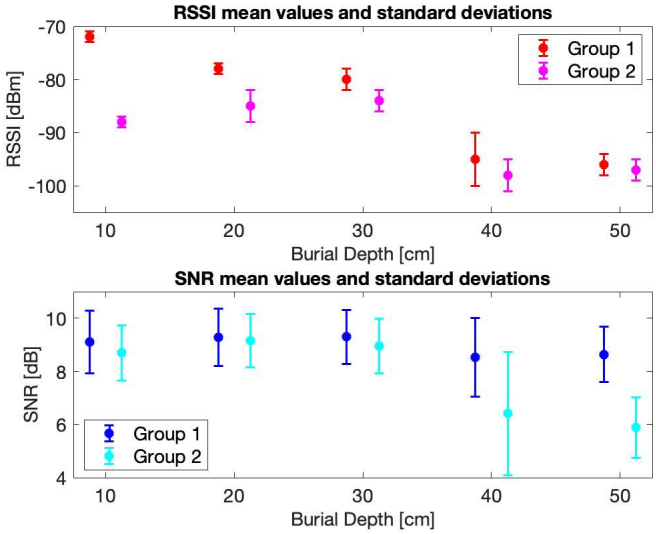

Figure 4.10: Test results of the preliminary laboratory measurement campaign for the LoRaWAN links sent by the IoUT sensor node: RSSIs and SNRs mean values and standard deviations.

Table 4.11: Underground tests results relative to the preliminary measurement campaign for LoRaWAN links: RSSIs and SNRs mean values and standard deviations along with PLs related to group #1.

Burial Depth [cm]	**Group #1** $G_{RX} = 14$ **dBi**				
	RSSI		**SNR [dB]**		**PL [%]**
	$\bar{x}$ **[dBm]**	s **[dB]**	$\bar{x}$	s	
10	−72	1	9.10	1.18	0.5
20	−78	1	9.29	1.08	0.4
30	−80	2	9.30	1.02	0.7
40	−95	5	8.53	1.48	0.4
50	−96	2	8.64	1.05	0.6

Table 4.12: Underground tests results relative to the preliminary measurement campaign for LoRaWAN links: RSSIs and SNRs mean values and standard deviations along with PLs related to group #2.

Burial Depth [cm]	**Group #2** $G_{RX} = 1$ **dBi**				
	RSSI		**SNR [dB]**		**PL [%]**
	$\bar{x}$ **[dBm]**	s **[dB]**	$\bar{x}$	s	
10	−88	1	8.70	1.04	0.4
20	−85	3	9.16	1.00	0.4
30	−84	2	8.95	1.03	0.0
40	−98	3	6.42	2.32	0.3
50	−97	2	5.89	1.14	0.5

The feasibility of UG2AG LoRaWAN links was confirmed both for a large link margin and for the impressive restricted figures for PLs. Particularly, the latter result could be stemmed out from the frequency diversity paradigm prescribed by LoRaWAN protocol. As expected, statistics degraded as burial depth increased. Test results from Tables 4.11 and 4.12 were sensibly worse than the estimated ones listed in Table 4.10: during the first group of tests an average difference of 11.8 dB between the measured RSSIs and the estimated ones in the worst case was experienced; throughout the last group of trials an average difference of 5 dB between the measured RSSIs and the estimated ones in the worst case occurred. This difference is not so impactful when considered in the telecommunications domain. However, the same discrepancy has a bigger extent from the point of view of the measurements field, especially when transmission performances are measured. However, the objective of this short-term measurement campaign was just to preliminary assess the modulation feasibility in such context, with the aim of enabling a sensor node forming a measurement system with connectivity. Therefore, firstly, the feasibility of UG2AG LoRa links was investigated; secondly, the quality of reception of such links was assessed, reproducing a standard situation belonging to a real application scenario (e.g., smart agriculture) in which a gateway is installed aboveground. Moreover, the link budget associated to LoRa links is notable since, on average, it has an order of magnitude of 140 dB. Therefore, the modulation is intrinsically suitable to be exploited in highly lossy setups, meaning that it can be successfully employed for covering long distances, or in harsh environments from the point of view of losses. Hence, given the LoRa link budget, it can be concluded that the observed discrepancy does not hinder the viability of a LoRa network exploited for UG2AG links. Such result was encouraging for continuing investigating the topic (as it is also shown in this Thesis). In addition, this discrepancy may be due to the adoption of the results from Peplinski for the assessment of $\epsilon^{'}$ and ϵ''. Indeed, a plausible reason is that the soil in which the IoUT sensor node was buried for the tests could have a slight different composition than the ones of Peplinski: either for sand, clay and loam and for the VWC which could have been reasonably greater than the 20 % throughout the transmission trials. Moreover, dissimilarities amid the values belonging to Tables 4.10, 4.11 and 4.12 may be motivated by miscellaneous losses which are hardly numerically assessable a priori. Albeit the inconsistency amid the estimated and the measured values for RSSIs, LoRa modulation and LoRaWAN standard were proven to be considered as valuable enabling technologies for IoUT sensor nodes which may be employed in more severe contexts with respect to the one exploited herein.

4.3.2 Preliminary Laboratory Measurement Campaign for LoRaWAN and NB-IoT Links

Losses due to the effect of the soil in this measurement campaign are shown in Figure 4.11 and listed in Table 4.13. First of all, no packet loss was experienced, thus remarking the robustness of both the technologies. Moreover, despite losses values within the same test condition slightly differ amid LoRaWAN and NB-IoT, they follow the same trend thus showing consistency. This behaviour is clear by looking at Figure 4.11: for instance, LoRaWAN performed worse during underground tests as burial depth gets bigger, and the same tendency was experienced by NB-IoT. Averagely, NB-IoT marginally outperforms LoRaWAN: this could be either due to the fact that the former is a cellular technology having higher Quality of Service (QoS) than LoRaWAN, and due to physics since NB-IoT operates at lower frequencies, albeit they are almost comparable, than LoRaWAN. However, an interesting detail is losses standard deviation: the ones of LoRaWAN are much smaller, and this could be due to the fact that just one LoRaWAN gateway was employed in contrasts with NB-IoT where multiple eNodeBs, whose geographical positions were unknown, were exploited. This hints at the fact that LoRaWAN can be deemed as more reliable in this application scenario, not so much for mean losses, as for the limited losses standard deviations.

Table 4.13: Losses mean values and standard deviations due to soil for both the technologies.

Burial Depth [cm]	**Losses [dB]**			
	LoRaWAN		**NB-IoT**	
	$\bar{x}$	s	$\bar{x}$	s
10	15.2	2.3	13.3	10.1
30	22.8	2.0	19.7	9.5
50	24.9	2.4	20.4	9.5

Measured losses were also compared with the relative estimates according to the models proposed in Section 4.1: Figure 4.12 shows the comparison results, while in Table 4.14 data are tallied. Underground loss estimates are quite diverse with respect to measurements regardless of the model: estimates are almost always twice to three times bigger than experimental data thus confirming the intrinsic harshness and attenuating properties of soil which are quite challenging to model. Moreover, both MBSDM and ITU models for soil losses estimation (which are massively employed within the literature) require an extended number of parameters as input, translating in a high variability.

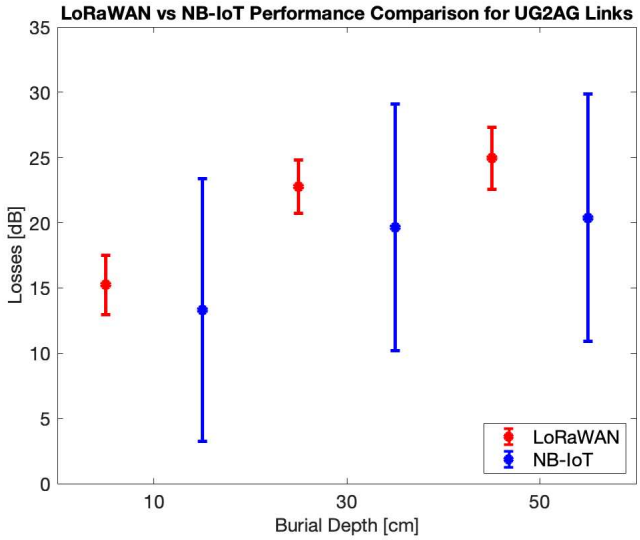

Figure 4.11: Losses mean values and standard deviations due to soil for both the technologies.

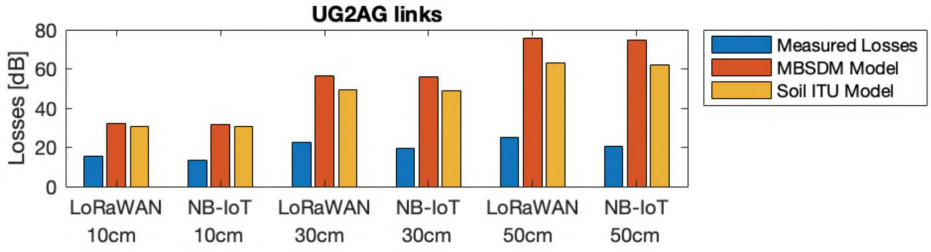

Figure 4.12: Losses comparison between measured and estimated values stemming from the model of Section 4.1 for each of the test conditions and for both the technologies.

Table 4.14: Measured underground losses in comparison with estimates for both the technologies.

	Burial Depth [cm]	Losses [dB]		Relative Difference [%]	
		LoRaWAN	NB-IoT	LoRaWAN	NB-IoT
Mean Measurements	10	15.2	13.3	–	–
MBSDM Model		32.2	31.9	−52.6	−58.2
ITU Model		30.9	30.9	−50.6	−56.9
Mean Measurements	30	22.8	19.7	–	–
MBSDM Model		56.4	56.0	−59.6	−64.9
ITU Model		49.6	46.7	−54.1	−57.9
Mean Measurements	50	24.9	20.4	–	–
MBSDM Model		75.5	74.9	−66.9	−72.8
ITU Model		63.2	61.8	−60.5	−67.0

4.3.3 Field Measurement Campaign

4.3.3.1 Soil Compaction Effect on RSSI Tests Results

During the 20 days in which the test assessing the effect of soil compaction on transmission performances on UG2AG links took place, different weather conditions were experienced, from clear sky to heavy rains. Daily rainfalls (see Figure 4.13) were retrieved from the closest weather station which is located 2.2 km far from the test site (i.e., Poggio al Vento weather station). The alternation between rainy and sunny periods allowed a full compaction of the soil after around 10 days.

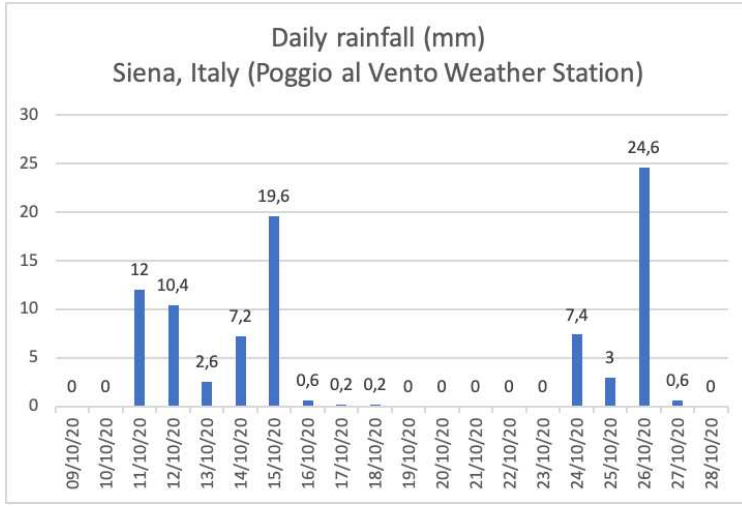

Figure 4.13: Daily rainfalls during the 20 days of the test on the assessment of soil compaction on transmission performances.

Figure 4.14 shows the trends of RSSI and SNR for the 20 days timespan by plotting their moving averages using a 3-hour window. From the Figure it is evident that the soil compaction had no effect on the actual transmission performances for the LoRaWAN channel. Indeed, there is no sign of any decrease for the two parameters, in particular for RSSI, along the whole 20 days period. Periodic fluctuations that can be noticed in the trends were not correlated with rainfalls (see Figure 4.13), and consequently with soil moisture, and they may be due to a wealth of other factors that were difficult to be taken into account. Nevertheless RSSI value was always in a range from -93.0 dBm down to -109.0 dBm, with a mean value of -100.5 dBm. On the other hand, SNR spanned in the range from 9.00 dB down to 1.00 dB with a mean value of 5.80 dB. These

results suggested that data can be reliably collected regardless of both the degree of soil compaction and the time the node spent buried underground.

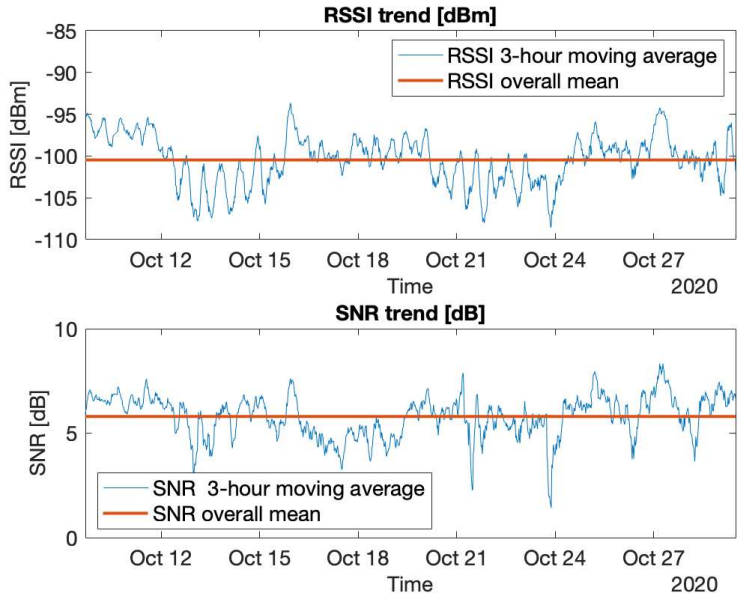

Figure 4.14: Test results on the effect of soil compaction on transmission performances: RSSI and SNR trends.

4.3.3.2 Field Tests Results

The results of the field measurement campaign are shown in Figure 4.15 and in Tables 4.15, 4.16, and 4.17. The detailed numerical results for each soil are then provided in Tables 4.15, 4.16, and 4.17 that also include data on PLs.

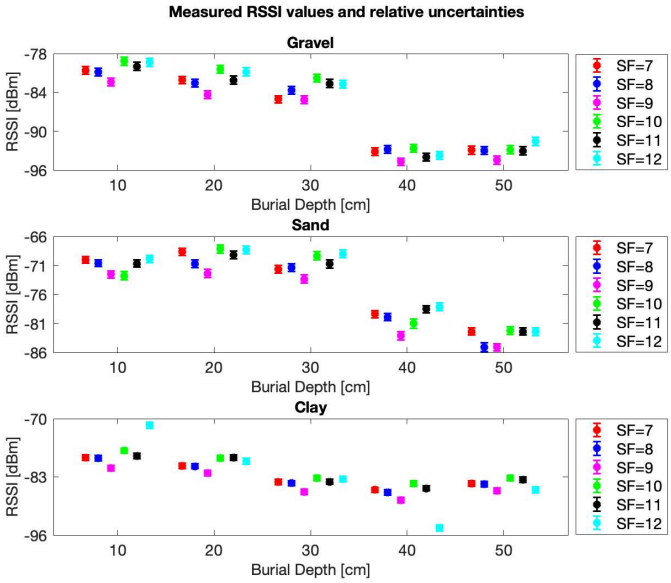

(a)

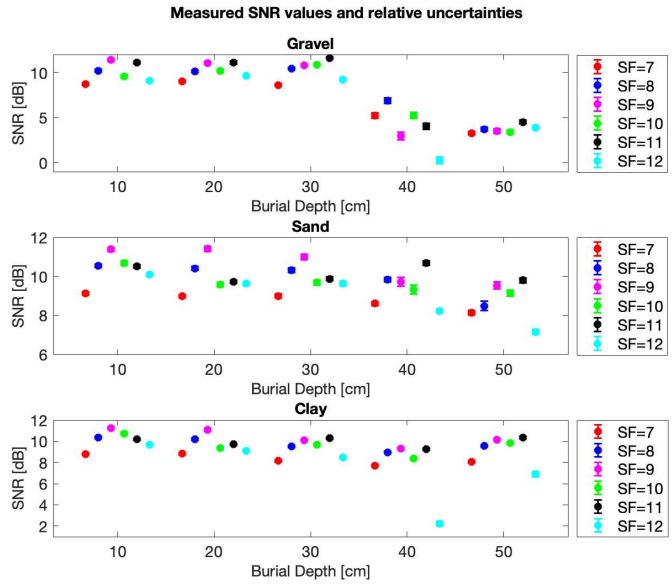

(b)

Figure 4.15: Field measurement campaign results: (a) measured RSSI values and relative uncertainties, (b) measured SNR values and relative uncertainties.

Table 4.15: Field measurement campaign results: RSSIs and SNRs measured values and relative uncertainties along with PLs for gravel soil (Merse #1).

			Burial Depth [cm]				
			10	**20**	**30**	**40**	**50**
SF=7	**RSSI**	$\bar{x}$ **[dBm]**	-80.6	-82.1	-85.1	-93.2	-92.9
		$u_c(\bar{x})$ **[dB]**	0.60	0.59	0.60	0.59	0.62
	SNR [dB]	$\bar{x}$	8.7	9.0	8.6	5.2	3.2
		$u_c(\bar{x})$	0.15	0.10	0.11	0.29	0.20
	PL [%]		0.6	0	0	0	0
SF=8	**RSSI**	$\bar{x}$ **[dBm]**	-80.9	-82.6	-83.7	-92.8	-93.0
		$u_c(\bar{x})$ **[dB]**	0.61	0.60	0.59	0.59	0.62
	SNR [dB]	$\bar{x}$	10.2	10.1	10.5	7.0	3.7
		$u_c(\bar{x})$	0.15	0.13	0.10	0.30	0.23
	PL [%]		0	0	0	0	0
SF=9	**RSSI**	$\bar{x}$ **[dBm]**	-82.4	-84.3	-85.1	-94.7	-94.5
		$u_c(\bar{x})$ **[dB]**	0.61	0.60	0.59	0.59	0.62
	SNR [dB]	$\bar{x}$	11.4	11.1	10.8	3.0	3.5
		$u_c(\bar{x})$	0.16	0.16	0.13	0.42	0.24
	PL [%]		1	0	0	0	0
SF=10	**RSSI**	$\bar{x}$ **[dBm]**	-79.2	-80.5	-81.8	-92.7	-92.9
		$u_c(\bar{x})$ **[dB]**	0.62	0.60	0.60	0.59	0.64
	SNR [dB]	$\bar{x}$	9.6	10.2	10.9	5.2	3.4
		$u_c(\bar{x})$	0.17	0.16	0.12	0.34	0.22
	PL [%]		0	0	0	0	0
SF=11	**RSSI**	$\bar{x}$ **[dBm]**	-80.0	-82.1	-82.6	-94.0	-93.0
		$u_c(\bar{x})$ **[dB]**	0.61	0.64	0.61	0.60	0.63
	SNR [dB]	$\bar{x}$	11.1	11.1	11.6	4.0	4.5
		$u_c(\bar{x})$	0.12	0.21	0.11	0.35	0.22
	PL [%]		0	0	0	0	0
SF=12	**RSSI**	$\bar{x}$ **[dBm]**	-79.4	-80.8	-82.7	-93.8	-91.6
		$u_c(\bar{x})$ **[dB]**	0.61	0.62	0.62	0.60	0.62
	SNR [dB]	$\bar{x}$	9.1	9.7	9.2	0.3	3.9
		$u_c(\bar{x})$	0.12	0.12	0.15	0.37	0.18
	PL [%]		0	0.3	0	0	1.6

Table 4.16: Field measurement campaign results: RSSIs and SNRs measured values and relative uncertainties along with PLs for sand soil (Merse #2).

			Burial Depth [cm]				
			10	**20**	**30**	**40**	**50**
SF=7	**RSSI**	$\bar{x}$ **[dBm]**	-70.0	-68.6	-71.7	-79.4	-82.4
		$u_c(\bar{x})$ **[dB]**	0.60	0.60	0.64	0.62	0.62
	SNR [dB]	$\bar{x}$	9.1	9.0	9.0	8.6	8.1
		$u_c(\bar{x})$	0.08	0.09	0.09	0.10	0.11
	PL [%]		0	0	0	0	0
SF=8	**RSSI**	$\bar{x}$ **[dBm]**	-70.6	-70.7	-71.4	-79.9	-85.1
		$u_c(\bar{x})$ **[dB]**	0.60	0.69	0.66	0.63	0.74
	SNR [dB]	$\bar{x}$	10.5	10.4	10.3	9.8	8.5
		$u_c(\bar{x})$	0.10	0.11	0.12	0.12	0.24
	PL [%]		0	0	0	0	0
SF=9	**RSSI**	$\bar{x}$ **[dBm]**	-72.6	-72.4	-73.4	-83.1	-85.1
		$u_c(\bar{x})$ **[dB]**	0.60	0.69	0.71	0.75	0.65
	SNR [dB]	$\bar{x}$	11.4	11.4	11.0	9.7	9.5
		$u_c(\bar{x})$	0.10	0.12	0.14	0.22	0.19
	PL [%]		0.3	0	0	0	0
SF=10	**RSSI**	$\bar{x}$ **[dBm]**	-72.8	-68.2	-69.4	-81.0	-82.2
		$u_c(\bar{x})$ **[dB]**	0.74	0.68	0.71	0.77	0.64
	SNR [dB]	$\bar{x}$	10.7	9.6	9.7	9.3	9.1
		$u_c(\bar{x})$	0.12	0.11	0.13	0.22	0.15
	PL [%]		0	0	0	0	0
SF=11	**RSSI**	$\bar{x}$ **[dBm]**	-70.7	-69.2	-70.8	-78.5	-82.4
		$u_c(\bar{x})$ **[dB]**	0.63	0.68	0.70	0.62	0.63
	SNR [dB]	$\bar{x}$	10.5	9.7	9.9	10.7	9.8
		$u_c(\bar{x})$	0.09	0.09	0.10	0.11	0.13
	PL [%]		0	0	0	0	0
SF=12	**RSSI**	$\bar{x}$ **[dBm]**	-69.9	-68.3	-69.0	-78.1	-82.4
		$u_c(\bar{x})$ **[dB]**	0.62	0.69	0.70	0.64	0.71
	SNR [dB]	$\bar{x}$	10.1	9.6	9.6	8.2	7.2
		$u_c(\bar{x})$	0.09	0.10	0.11	0.09	0.14
	PL [%]		0	0	0	0	0

Table 4.17: Field measurement campaign results: RSSIs and SNRs measured values and relative uncertainties along with PLs for clay soil (Certosa).

			Burial Depth [cm]				
			10	**20**	**30**	**40**	**50**
SF=7	**RSSI**	$\bar{x}$ **[dBm]**	-78.7	-80.5	-84.1	-85.9	-84.5
		$u_c(\bar{x})$ **[dB]**	0.58	0.59	0.58	0.58	0.58
	SNR [dB]	$\bar{x}$	8.8	8.8	8.2	7.7	8.1
		$u_c(\bar{x})$	0.08	0.08	0.08	0.08	0.08
	PL [%]		0.6	0	1	0.3	0.3
SF=8	**RSSI**	$\bar{x}$ **[dBm]**	-78.8	-80.6	-84.4	-86.5	-84.6
		$u_c(\bar{x})$ **[dB]**	0.58	0.59	0.58	0.58	0.58
	SNR [dB]	$\bar{x}$	10.4	10.2	9.5	9.0	9.6
		$u_c(\bar{x})$	0.09	0.09	0.08	0.08	0.08
	PL [%]		0.3	0	0.3	0.3	0.3
SF=9	**RSSI**	$\bar{x}$ **[dBm]**	-81.1	-82.2	-86.3	-88.2	-86.1
		$u_c(\bar{x})$ **[dB]**	0.59	0.59	0.59	0.59	0.59
	SNR [dB]	$\bar{x}$	11.3	11.1	10.1	9.3	10.2
		$u_c(\bar{x})$	0.10	0.10	0.09	0.10	0.10
	PL [%]		0.6	0.3	1	1	0.3
SF=10	**RSSI**	$\bar{x}$ **[dBm]**	-77.1	-78.8	-82.2	84.5	-83.2
		$u_c(\bar{x})$ **[dB]**	0.58	0.59	0.58	0.58	0.58
	SNR [dB]	$\bar{x}$	10.7	9.4	9.7	8.4	9.8
		$u_c(\bar{x})$	0.11	0.10	0.10	0.09	0.11
	PL [%]		0.6	0.3	0.3	1	0
SF=11	**RSSI**	$\bar{x}$ **[dBm]**	-78.3	-78.7	-84.1	-85.5	-83.7
		$u_c(\bar{x})$ **[dB]**	0.60	0.61	0.60	0.60	0.60
	SNR [dB]	$\bar{x}$	10.2	9.7	10.3	9.2	10.4
		$u_c(\bar{x})$	0.08	0.08	0.09	0.10	0.12
	PL [%]		0	1	0.3	0	1.6
SF=12	**RSSI**	$\bar{x}$ **[dBm]**	-71.5	-79.5	-83.5	-94.4	-85.9
		$u_c(\bar{x})$ **[dB]**	0.70	0.64	0.62	0.63	0.68
	SNR [dB]	$\bar{x}$	9.7	9.1	8.5	2.2	6.9
		$u_c(\bar{x})$	0.10	0.11	0.09	0.22	0.24
	PL [%]		0.3	6	0	3.3	6.6

Let us apply the model described in Section 4.1. Since the IoUT sensor node implemented a frequency diversity scheme, the mean value of the frequencies of the channels (i.e., 867.8 MHz) will be used in all the equations. As it was previously stated, the gateway was placed at a distance d_{AG} of 15.00 m and due to the fact that it was laid on the ground, $d_{Surface} = d_{AG}$. Therefore, from Equation 3.5, L_{AG} was equal to 54.74 dB and, from Equation 4.21, $L_{Surface}$ was equal to 47.04 dB. For what concerns the terms of

Table 4.18: Results of Equations 4.3 and 4.4 exploiting the values of $\epsilon^{'}$ and $\epsilon^{''}$ either according to MBSDM and ITU models for gravel soil (Merse #1) of the field measurement campaign.

		Burial Depth [cm]		
		10	**30**	**50**
MBSDM	$\epsilon^{'}$ **[F/m]**	5.04	5.97	6.14
	$\epsilon^{''}$ **[F/m]**	0.37	0.47	0.48
	α **[1/m]**	1.58	1.72	1.75
	β **[rad/m]**	40.87	44.67	45.11
ITU	$\epsilon^{'}$ **[F/m]**	3.83	4.49	4.56
	$\epsilon^{''}$ **[F/m]**	0.41	0.56	0.53
	α **[1/m]**	1.88	2.39	2.25
	β **[rad/m]**	35.62	38.61	38.89

Table 4.19: Results of Equations 4.3 and 4.4 exploiting the values of $\epsilon^{'}$ and $\epsilon^{''}$ either according to MBSDM and ITU models for sand soil (Merse #2) of the field measurement campaign.

		Burial Depth [cm]		
		10	**30**	**50**
MBSDM	$\epsilon^{'}$ **[F/m]**	4.46	4.73	5.09
	$\epsilon^{''}$ **[F/m]**	0.31	0.34	0.37
	α **[1/m]**	1.38	1.42	1.47
	β **[rad/m]**	38.44	39.59	41.05
ITU	$\epsilon^{'}$ **[F/m]**	12.12	12.90	13.47
	$\epsilon^{''}$ **[F/m]**	2.96	3.22	3.12
	α **[1/m]**	7.67	8.09	7.69
	β **[rad/m]**	63.76	65.81	67.18

Equation 4.1, they varied depending on the adopted procedure to evaluate $\epsilon^{'}$ and $\epsilon^{''}$ (i.e., according to MBSDM and ITU). In particular, ITU method was carried out by resorting to a specific MATLAB function [97]. In addition, they also changed in compliance with the burial depth because the required parameters by the two models changed by following the same trend. Therefore, the values of $\epsilon^{'}$ and $\epsilon^{''}$ along with the results from Equations 4.3 and 4.4 are reported within Tables 4.18, 4.19 and 4.20 either for MBSDM and ITU procedures and respectively for the three test soils.

Table 4.20: Results of Equations 4.3 and 4.4 exploiting the values of $\epsilon^{'}$ and $\epsilon^{''}$ either according to MBSDM and ITU models for clay soil (Certosa) of the field measurement campaign.

		Burial Depth [cm]		
		10	**30**	**50**
MBSDM	$\epsilon^{'}$ **[F/m]**	6.71	7.84	7.27
	$\epsilon^{''}$ **[F/m]**	2.29	2.70	2.49
	α **[1/m]**	7.96	8.61	8.29
	β **[rad/m]**	47.77	51.64	49.79
ITU	$\epsilon^{'}$ **[F/m]**	9.71	11.59	10.55
	$\epsilon^{''}$ **[F/m]**	2.09	2.48	2.27
	α **[1/m]**	6.07	6.59	6.32
	β **[rad/m]**	57.00	62.26	59.38

Finally, the RSSIs estimates may be computed by applying Equation 4.1 and the results are listed within Table 4.21. For the sake of comparison, for each test site the mean values of RSSIs were computed by averaging the sampled data for all of the SFs respectively at the burial depth of 10 cm, 30 cm, and 50 cm, and also these values are listed in Table 4.21.

Table 4.21: RSSIs estimates by applying the model in Section 4.1 evaluating $\epsilon^{'}$ and $\epsilon^{''}$ either according to MBSDM and ITU models in comparison with the mean values of the measured RSSI during the field measurement campaign.

				Burial Depth [cm]			Relative Difference [%]		
				10	**30**	**50**	**10 cm**	**30 cm**	**50 cm**
RSSI [dBm]	**Estimates**	**MBSDM**	**Gravel (Merse #1)**	-54.03	-67.38	-75.04	−48.8	−23.9	−23.9
			Sand (Merse #2)	-53.36	-65.65	-73.08	−33.3	−8.0	−14.0
			Clay (Certosa)	-60.86	-80.57	-104.27	−27.5	−5.9	18.8
		ITU	**Gravel (Merse #1)**	-53.16	-67.95	-75.99	−51.2	−22.9	−22.4
			Sand (Merse #2)	-62.99	-87.22	-104.14	−12.9	−12.0	20.3
			Clay (Certosa)	-60.67	-82.85	-97.16	−27.9	−3.0	12.8
	Mean Measurements		**Gravel (Merse #1)**	-80.4	-83.5	-93.0	–	–	–
			Sand (Merse #2)	-71.1	-70.9	-83.3	–	–	–
			Clay (Certosa)	-77.6	-85.3	-84.7	–	–	–

Taking into account the results shown in Figure 4.10 and Tables 4.15, 4.16, and 4.17, it is possible to make some interesting considerations about the usability of LoRa technology

for UG2AG data transmission in different contexts.

Firstly, successful data transmissions from underground at depths up to 50 cm can be achieved for every soil composition. Indeed, for the proposed experimental setup, for each test PL was almost always below 2 % (apart for clay at SF$=12$ for depths of 40 cm and 50 cm), which can be considered a physiological threshold for any successful LoRa transmission. Concerning the different types of soil, results showed that gravel provides the worst performances for what concerns RSSI and SNR, while the best ones are provided by sandy soil. Nevertheless, the difference was in general around 10 dB, suggesting that these values can be used to estimate the performances of the bulk of common soils which are in general a mixture of these three particle sizes.

Since LoRa receivers are generally characterized by a very high sensitivity value (e.g., the exploited gateway for this measurement campaign has a sensitivity down to -137 dBm at SF$=12$), that allows to receive packets even with very poor RSSIs, the results of the test suggested the viability of this transmission technology even in harsher conditions. Nevertheless, the following considerations can be made:

- In order to better point out the attenuating effects of the UG2AG transmission, for what concerns the underground lag of the transmission channel, the gateway was placed at a limited distance from the node burial spot. Nevertheless, even in the worst case link margin was high enough (i.e., -94.7 dBm$+137$ dBm$=42.3$ dB) to ensure a theoretically long aboveground transmission distance. Indeed, at 868 MHz, for a 1000 m transmission distance in air, free space loss can be calculated as in Equation 3.5 resulting in 31.22 dB.

- Other factors may concur in degrading the transmitted signal, first of all VWC: indeed, for every kind of radio transmission a larger water presence turns in larger attenuating phenomena. While the assessment of the system performances for different VWC contents will be done in a dedicated measurement campaign, a rough indication of its possible contribution can be extrapolated from the test assessing the effect of soil compaction on RSSI. In this case, during the test assessing the effect of soil compaction on RSSI, the node was kept running for a 20-day period, during which several rainy days occurred. As a consequence, a high VWC was surely experienced in this timespan. Nevertheless, no significant signal degradation was measured, thus suggesting that VWC impact on link budget should be quite limited.

- Another critical parameter that may affect the UG2AG channel is the chemical composition of soil. In this case, high salinity values or presence of metallic sediments may have attenuating effects on transmission. Analysing such a phe-

nomenon by means of field tests is anyway very complex because of several factors. Some of them include the difficulty in finding a wide range of different test sites characterized by the required chemical compositions, the wide range of possible parameters to be taken into account and the non-homogeneity of the composition even in soils with homogeneous sedimentological features.

A further analysis points out that RSSIs and SNRs related to 50 cm underground within gravel (i.e., Merse $\#1$) and clay (i.e., Certosa) were slightly better than those obtained at a burial depth of 40 cm within the same fields. This odd data is justified by the fact that LoRaWAN networks are naturally subject to RSSI oscillations at the receiver side due to a plethora of factors, the bulk of which are hardly identifiable. Nonetheless, such oscillatory outcomes usually stem out from statistical fluctuations, thus they would be averaged out in case a huge number of packets would have been received. Theoretically, the aforesaid number should be infinite, but practically speaking the same effect (i.e., fluctuation vanishing) would take place whether the number of received packets would have been $3 - 4$ orders of magnitude greater than the one carried out during the field measurement campaign.

A last, yet important, consideration has to been drawn by resorting to data within Tables 4.18, 4.19 and 4.20: from these values, the difference between theoretically calculated and measured RSSI values is evident. Such a result suggests that a perfect modelling of a real UG2AG transmission channel was scarcely achievable. The discrepancy among the values may be due to an extremely wide range of different factors, like the presence of attenuating items in the test environments (e.g., trees, vegetation, rivers, etc.), different environmental and meteorological conditions during the tests (relative humidity, mist, temperature, etc.), or the possible presence of rock layers below the test sites. All these factors are almost unpredictable and fall within the so-called miscellaneous losses L_M. At the same time, for some tests the measured value was larger than the theoretical one: in this case too, several factors may concur in achieving this outcome like, for instance, soil porosity. In conclusion, despite these discrepancies, it is still possible to point out that the theoretical models can be extremely precious to evaluate the feasibility of the UG2AG radio link, provided that miscellaneous losses (having an order of magnitude that can be deduced from the comparison in Table 4.21) are considered during estimation procedures.

Chapter 5

Underwater-to-Abovewater Links

5.1 Path Loss Model

Underwater environments are extremely harsh, especially the marine ones due to the presence of dissolved salt acting as a corrosive and rusting agent on electronics. This means that proper housing strategies must be implemented so to protect devices. However, because of the necessity of sampling physical quantities underwater, sensors have to be placed outside the protective housing, translating into the requirement of ad hoc designing phases for such components. Conversely, transmitting antennas can be installed within the protecting housing. Nonetheless, the transmitted signals experience the underwater path, producing a notable attenuation. For this reason, estimating losses in such contexts is fundamental whenever an underwater measurement system has to be designed [98, 99, 100], where sensor nodes are deployed both underwater and abovewater. Therefore, network links may be labelled as Underwater-to-Underwater (UW2UW), Underwater-to-Abovewater (UW2AW), and Abovewater-to-Underwater (AW2UW). For what concerns application scenarios, underwater measurement systems can be exploited, for instance, in lakes [101, 102], in contaminated ecosystems [103], in fish farming plants [104], or in marine contexts [105].

Underwater links suffer from the attenuation properties of water. Generally, this is strictly related to the temperature of water, the quantity of dissolved salt, and to the possible presence of metallic structures underwater. However, the latter condition is only met within specific application scenarios (e.g., oil and gas infrastructures), therefore it will not be taken into account below.

Underwater and underground media share the same channel model. The only difference is the method for evaluating the relative complex permittivity. However, for the sake of readability, such model is repeated by considering water as propagation medium, and by making reference to Figure 5.1.

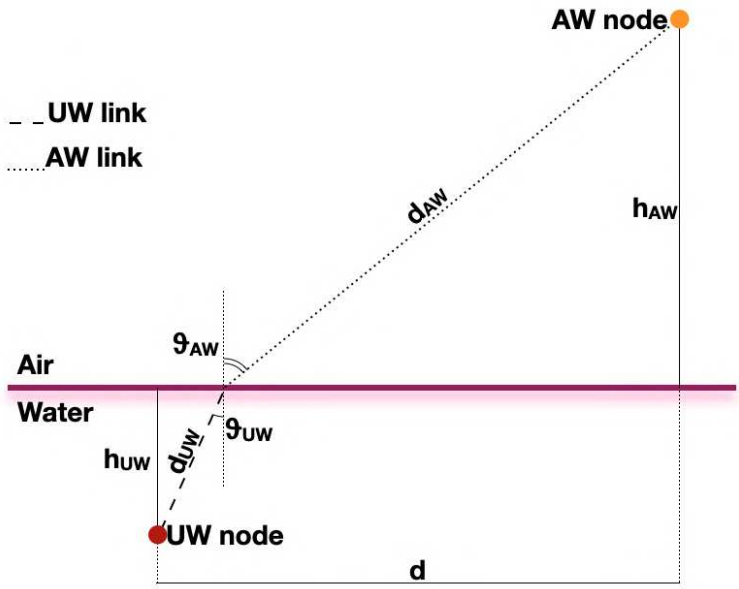

Figure 5.1: Channel model for both UW2AW links.

Losses in UW2AW links can be evaluated as the superimposition of two terms [102]: losses within the medium (i.e., L_{UW}) and losses at the medium-air interface (i.e., L_{UW-AW}). Therefore, the total losses can be computed in dB as:

$$L_{Tot} = L_{UW} + L_{UW-AW}. \tag{5.1}$$

L_{UW} may be computed resorting to

$$L_{UW} = 6.4 + 20log_{10}(d_{UW}) + 20log_{10}(\beta) + 8.69\alpha d_{UW} \tag{5.2}$$

where d_{UW} is the path the signal covers underwater in m, while α and β are in turn constants for the attenuation and for the phase shifting that can be evaluated by respectively resorting to Equation 4.3 and Equation 4.4, in which f is the carrier frequency, μ_r is the relative magnetic permeability of water, that can be considered 1 presuming it as metal-free, while $\epsilon^{'}$ and $\epsilon^{''}$ respectively are the real and imaginary part of the effective water permittivity. For the sake of completeness, α and β are related one another via the propagation constant in a lossy medium:

$$\gamma = \alpha + j\beta. \tag{5.3}$$

Owing to the fact that water permittivity is by far bigger than the one of the air, signals are able to emerge towards air only if their incident angle θ_{UW} is small enough. Thus, signals follow a vertical propagation towards the interface entailing the approximation $\theta_{UW} \simeq 0$ leading to $d_{UW} \simeq h_{UW}$, and $d_{AW} = \sqrt{d^2 + {h_{AW}}^2}$, while d is the distance between the UW and AW nodes. Therefore, refraction losses taking place at the medium-air interface (i.e., L_{UW-AW}) are evaluated according to

$$\begin{aligned} L_{UW-AW} =& 10log_{10}\left[\frac{(cos\theta_{UW} + \sqrt{\epsilon' - sin^2\theta_{UW}})^2}{4cos\theta_{UW}\sqrt{\epsilon' - sin^2\theta_{UW}}}\right] \\ \simeq& 10log_{10}\left[\frac{(1+\sqrt{\epsilon'})^2}{4\sqrt{\epsilon'}}\right]. \end{aligned} \tag{5.4}$$

The real and imaginary parts of the complex permittivity of water can be assessed by resorting to two alternative procedures: Debye model [106] and the techniques issued by ITU [82]. Debye model is valid for frequencies lower than 100 GHz and for temperatures ranging from -4 °C to 40 °C, and it requires as inputs the water temperature T and the carrier frequency f. Real and imaginary parts of relative complex permittivity of water (i.e., $\epsilon^{'}$ and $\epsilon^{''}$) are computed as:

$$\epsilon^{'} = \epsilon_\infty + \frac{\gamma_D^2(\epsilon_0 - \epsilon_\infty)}{\gamma_D^2 + f^2}; \tag{5.5}$$

$$\epsilon^{''} = \frac{\gamma_D(\epsilon_0 - \epsilon_\infty)}{\gamma_D^2 + f^2}; \tag{5.6}$$

where ϵ_0 is the static dielectric constant of water at low frequency, ϵ_∞ is the dielectric constant of water at high frequency limit and γ_D is the relaxation frequency of water. The latter is equal to:

$$\gamma_D = \frac{1}{2\pi\tau} = \frac{480.77(T^2 + 63.0128T + 1381.72)}{(T + 273.15)^2} \tag{5.7}$$

where τ is the relaxation time constant for water and T is water temperature expressed in °C. Finally, the static dielectric constant of water at low frequency can be computed as

$$\epsilon_0 = \frac{30990}{273.15 + T} - 25.64 \tag{5.8}$$

where T is water temperature expressed in °C, while the dielectric constant of water at high frequency limit is

$$\epsilon_\infty = 0.066\epsilon_0. \tag{5.9}$$

5.2 Measurement Setup

Wireless measurement systems deployed underwater are usually enabled by ultrasonic devices, because they proved to be robust in such application scenarios (indeed, they do not rely on electromagnetic propagation), along with the fact that they allow for long range coverage underwater (due to the relative wavelength). While ultrasonic underwater systems were widely validated, it is commonly known that long range communication infrastructures exploiting electromagnetic technologies are not effective. Nonetheless, they could be employed for underwater data transmission provided that short distances would be covered. To this end, these tests aim at showing the performances of LoRaWAN and NB-IoT technologies underwater, and specifically in UW2AW links. Such tests were carried out in laboratory, and considered as metric the measured losses due to water. UW2AW links were tested by exploiting both LoRaWAN and NB-IoT LPWAN standards. For what concerns LoRaWAN, the prototype of the network infrastructure of Figure 3.5 was retrieved. Moreover, concerning the sensor node, the prototype of the multi-protocol transmitter of Section 4.2.2 was adopted. However, for the sake of readability, its characteristics are reported below by making reference to Figure 4.4.

The most important part of the sensor node was a Nucleo-L073RZ board produced by STMicroelectronics which embeds an STM32L073 microcontroller. It concurrently drove via SPI a LoRaWAN transceiver (i.e., the RFM95 produced by HopeRF), and via USART an NB-IoT transceiver (i.e., the SARA UBee produced by Sodaq). Power to the Nucleo board was provided by exploiting a power bank, while the transceivers were both powered by the Nucleo board itself. The microcontroller run the firmware of a Class A LoRaWAN device, transmitting LoRaWAN packets by resorting to a frequency diversity scheme via a frequency hopping technique amid 8 different channels belonging to the $863 - 870$ MHz ISM band. Moreover, LoRaWAN packets payloads were composed of a 10 B test string, and they were sent by making use of SF$= 7$, bandwidth of 125 kHz and CR$= 4/5$, testing a worst case scenario, and by exploiting a $\lambda/8$ whip antenna having 2 dBi gain. On the other hand, the NB-IoT module was controlled by the Nucleo board by resorting to AT commands. Firstly, it performed all the joining routines so to connect to the NB-IoT network. Secondly, it sent packets employing the MQTT protocol. Such packets contained a counter and the relative RSSI of the acknowledgement signals the eNodeB broadcast to the transceiver throughout the synchronisation procedures. Transmissions occurred within the $863 - 870$ MHz band via a $\lambda/8$ whip antenna having 2 dBi gain.

The multi-protocol sensor node was tested 19 cm underwater, by measuring losses ascribed by the attenuating properties of water. Further depths were not tested due to the limitation of the testing site (i.e., a fountain in an out of order state). To this end, a set of 300 transmissions for both the technologies was performed in parallel,

Figure 5.2: Test setup for the UW2AW links exploiting LoRaWAN and NB-IoT technologies.

by placing the prototype at open air and by measuring and storing the relative RSSIs. Next, an additional set of 300 transmissions was carried out by deploying the sensor node underwater. Subsequently, losses were calculated by subtracting RSSIs from the first set of measurements to the ones taking place underwater. Therefore, any losses due to factors which were not related to the critical environments could be neglected. Finally, experimental losses were compared to the estimated ones by exploiting the models presented in Section 5.1. For what concerns LoRaWAN, the packets RSSIs were measured by the gateway (i.e., the one of Section 3.2.1), that was installed 35 m apart from the multi-protocol sensor node. Such distance was chosen because of logistical constraints related to the availability of mains for powering the gateway. Conversely, NB-IoT packets RSSIs were retrieved exploiting a computer running an MQTT client subscribed to the same MQTT topic on which the multi-protocol sensor node published data. Finally, Table 5.1 summarises the test settings.

The tests were carried out by enclosing the prototype within an IP68 box and by submerging it within a fountain (see Figure 5.2) containing fresh water at 8 °C. Since the fountain had a mix of rainwater and water coming from the city aqueduct, and owing to the fact that no salt was added, such water can be considered as salt free.

Table 5.1: Summary of the settings related to the comparative measurement campaign accounting for LoRaWAN and NB-IoT.

Transmission Technology	SF	CR	Payload	# Packets	Underwater Depth
LoRaWAN	7	4/5	10 B	300	19 cm
NB-IoT	–	–	10 B	300	19 cm

5.3 Results and Discussion

Losses due to water are reported in Figure 5.3 and listed in Table 5.2, and the robustness of both the technologies was proven because no packet loss arose. On average, LoRaWAN performances were slightly worse than the ones of NB-IoT, and this can be due to the fact the latter offers a higher QoS since it operates in licensed frequency bands. Nonetheless, NB-IoT showed a much larger RSSIs standard deviation with respect to LoRaWAN. This is due to the fact that a single LoRaWAN gateway was exploited, while several eNodeBs, sparsely located, were used.

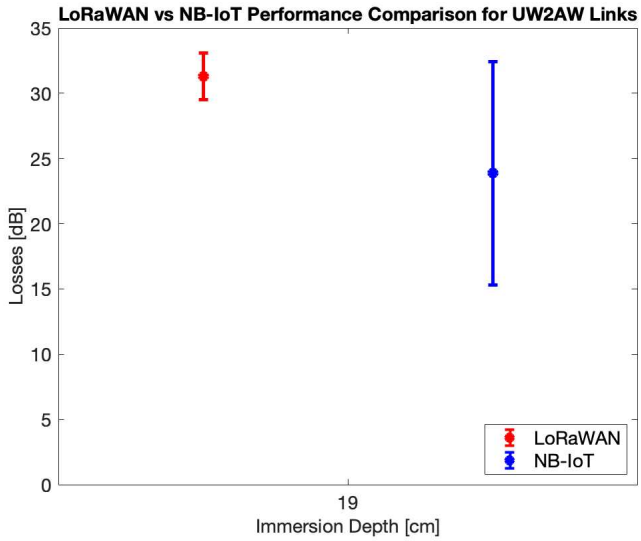

Figure 5.3: Losses mean values and standard deviations due to water for both the technologies.

Table 5.2: Losses mean values and standard deviations due to water in UW2AW links.

Immersion Depth [cm]	**Losses [dB]**			
	LoRaWAN		**NB-IoT**	
	$\bar{x}$	s	$\bar{x}$	s
19	31.3	1.8	23.9	8.6

The theoretical loss models of Section 5.1 were compared with the experimental results in Figure 5.4, which visually shows the comparison, and in Table 5.3. Debye model far better estimates losses than the one issued by ITU: by applying the former model, few dB of difference were experienced with respect to tens of dB when the latter model is considered.

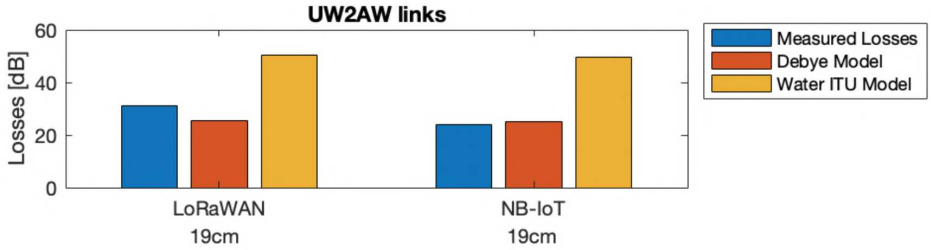

Figure 5.4: Losses comparison between measured and estimated values stemming from the model of Section 5.1 for both the transmission technologies.

Table 5.3: Measured underwater losses in comparison with estimates for both the technologies.

	Losses [dB]		**Relative Difference [%]**	
	LoRaWAN	**NB-IoT**	**LoRaWAN**	**NB-IoT**
Mean Measurements	31.3	23.9	–	–
Debye Model	25.4	25.2	23.2	−5.3
ITU Model	50.4	49.7	−37.8	−52.0

Chapter 6

Through-Metal Links

6.1 Path Loss Model

Through-metal communications usually occur whenever sensor nodes need to be housed within metal boxes, or when the requirement of monitoring whatsoever parameter within metallic-enclosed environments arises. For instance, the application scenario in which such transmission paradigm is encountered the most is freight containers shipping, where the monitoring of environmental parameters (e.g., temperature, relative humidity and air pressure) during transportation can be achieved along with the container tracking [22]. Similarly, vehicle localisation within indoor car parks can be set up provided that each vehicle has a beacon installed inside [107]. Such outcome is achievable also by resorting to the results of [108, 109] showing the feasibility of satisfactory wireless links (i.e., LoRaWAN transmissions in particular) from the inside of metal cabinets. However, even cellular LPWAN standards proved their effectiveness in container monitoring and tracking throughout their shipments. In particular, in [110] NB-IoT is widely tested and validated in such context.

The metallic enclosure enveloping the transmitter, or the receiver, acts as a shield in through-metal links. In particular, if it is solid, meaning that it has no holes or apertures, just few mm of thickness are extremely effective preventing any sort of wireless transmission. However, such hypothesis is hard to meet because in real applications metallic enclosures are not continuous, meaning that some apertures like lids or cable glands are present. In these cases, the shield is not ideal, and allows electromagnetic waves to propagate towards the outside. This theory is the one on which path loss models in these contexts are grounded.

Through-metal losses are strictly related to Shielding Effectiveness (SE) of the metallic structure within which the transmitter, or the object requiring to be shielded, is enclosed. In particular, SE can be expressed in terms of the reduction in either the magnetic and electric fields strength induced by the shield. Moreover, it is far more convenient to measure SE in dB since such a choice allows to sum sundry effects causing the total SE.

Therefore, as a first instance, SE can be expressed in dB in turn as

$$SE = 20log_{10}\left(\frac{E_0}{E_1}\right), \tag{6.1}$$

$$SE = 20log_{10}\left(\frac{H_0}{H_1}\right) \tag{6.2}$$

where E_0, H_0 is the incident field strength, and E_1, H_1 is the field strength of the transmitted wave as it emerges from the shield. Unfortunately, measuring those quantities within practical contexts is not always easy. Therefore, theoretical models were put forth so to estimate SE.

SE theory was originally stated by Schelkunoff [111]. It is grounded on the ideal assumption of dealing with fully solid shields. However, such a condition is usually too constraining in the bulk of the application scenarios since most shields are not solid. There must be access doors, covers, holes for ventilation or cables, seams, joints and so on. These apertures notably reduce SE, especially at high frequencies (i.e., from the order of magnitude of MHz and above, in which ISM bands where LPWANs operate are located) when the endogenous SE due to shield material is less effective with respect to leakages due to apertures. In other words, SE of apertures determines the overall SE, and not the intrinsic shield material SE whenever high working frequencies are employed. The latter theory, which directly stems from first hand experience on electromagnetic compatibility problems, was formalised by Ott [112]. Herein, both the theories will be shown so to provide a complete overview. In addition, without losing generality, within the theoretical treatise suppose the source of the electromagnetic field within the shield rather than outside.

6.1.1 Ideal Shields

Consider the SE provided by a plane sheet of conducting material with no holes or apertures thus being solid (see Figure 6.1).

SE can be evaluated as the superimposition of the terms

$$SE = A + R + B \tag{6.3}$$

where A represents losses due to absorption phenomenon of shield material, R accounts for reflection losses generated by the shield and B stands for a correction factor due to multiple reflections occurring in thin shields.

The amplitude of an electromagnetic wave exponentially decays whenever it crosses a medium. This decrease takes place due to the induced currents in the shield triggering

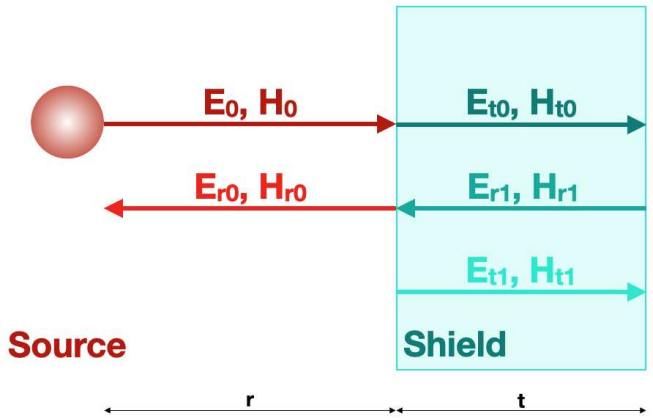

Figure 6.1: Channel model for evaluating SE according to Schelkunoff theory. The source irradiates a field (i.e., E_0 and H_0) which impinges on a shield. Part of the wave is reflected (i.e., E_{r0} and H_{r0}) and part enters in the shield (i.e., E_{t0} and H_{t0}). If the shield is thick enough, the latter wave is completely absorbed, otherwise multiple reflections occur within the shield (i.e., E_{r1}, H_{r1} and E_{t0}, H_{t0}).

losses as a result of material heating. Such phenomenon gives rise to absorption losses through the shield calculable in dB as

$$A = \frac{8.69t}{\delta} \tag{6.4}$$

where t is shield thickness expressed in m, and δ

$$\delta = \sqrt{\frac{1}{\pi f \mu_0 \mu_r \sigma_0 \sigma_r}} \tag{6.5}$$

is the skin depth expressed in m. Finally, σ_0 is the conductivity of copper while σ_r is the shield material relative conductivity with respect to the one of copper.

When an electromagnetic wave bumps into a medium, in part it is back-scattered and, at the same time, it propagates in the medium. Such a fact causes reflection losses R whose extent depends on r which is the distance between the field source and the shield. Indeed, close to the source, field properties are mainly defined by source characteristics. Conversely, far from the source, field properties are mostly outlined by the propagation medium. Therefore, the space in which a radiating source is present can be distinguished into two regions depending on the wavelength λ: near the source (i.e., at distances less than $\lambda/2\pi$) an induction field is present; far from the source (i.e., at distances greater than $\lambda/2\pi$) a radiation field exists. Such discriminating point translates into the fact that wave impedance Z_w (i.e., the ratio between the electric field E and the magnetic one

H) drastically changes. In free space, wave impedance Z_0 is $377\,\Omega$. For radiation fields, wave impedance equals the propagating medium characteristic one. On the other hand, for induction fields, wave impedance depends both on the distance from the source and on source characteristics. Indeed, if the latter has high current and low voltage (e.g., a loop antenna), the induction field is predominantly magnetic and $Z_w < Z_0$; while if the source has low current and high voltage (e.g., a straight wire antenna), then the induction field is mainly electric and $Z_w > Z_0$. This background is needed to evaluate R because this issue is grounded on the difference in characteristic impedances between the media thus resembling to an optical problem. Therefore, R is assessed as follows:

$$R = \begin{cases} 168 + 10log_{10}\left(\frac{\sigma_r}{\mu_r f}\right) & if\, r > \frac{\lambda}{2\pi} \\ 322 + 10log_{10}\left(\frac{\sigma_r}{\mu_r f^3 r^2}\right) & if\, r \leq \frac{\lambda}{2\pi} \cap Z_w > Z_0 \\ 14.6 + 10log_{10}\left(\frac{f r^2 \sigma_r}{\mu_r}\right) & if\, r \leq \frac{\lambda}{2\pi} \cap Z_w < Z_0 \end{cases}. \tag{6.6}$$

In case thin shields are exploited, multiple reflections within the shield may take place. Indeed, the wave propagating through the barrier may be not so absorbed thus being capable of being reflected once again by the second boundary of the shield. Similarly, and especially for extremely thin barriers, this phenomenon may be triggered one more time at the first boundary thus giving rise to a new wave reflection. By the time the wave reaches the second boundary for the second time, it has an exiguous amplitude since it has travelled the shield thickness back and forth three times. This fact is modelled by the correction term B in Equation 6.3 which is evaluated according to r and to the extent of A. Indeed, if $A \geq 9\,\text{dB}$, then multiple reflections may be neglected. In addition, since electric fields are usually completely reflected by the first shield boundary, it is worth accounting for B only when magnetic fields are examined by taking into account the exponential decay of H within the shield which is strictly related to t and δ. Therefore, B is evaluated as follows:

$$B = \begin{cases} 20log_{10}(1 - e^{\frac{-2t}{\delta}}) & if\, r \leq \frac{\lambda}{2\pi} \cap Z_w < Z_0 \cap A < 9\,dB \\ 0 & else \end{cases}. \tag{6.7}$$

Summarising, according to Schelkunoff theory and assumptions, it is relatively easy to obtain high SE (i.e., way more than $100\,\text{dB}$) without resorting to extremely thick shields as far as shield continuity is concerned.

6.1.2 Shields with Apertures

Leakage effect due to apertures primarily depends on: the maximum linear dimension of the aperture, despite the common belief that its area matters the most; Z_w of the

incident field; the frequency of the field. Maximum linear dimension plays a key role because the impinging electromagnetic field induces a current into the shield generating an induced supplementary field that is able to nullify the impinging one. This effect takes place at the opposite shield boundary with respect to the incident one (i.e., outside the shield). However, this counteraction occurs only if the induced current is allowed to smoothly flow in the shield as it was induced. Therefore, if apertures are presents, then the induced current will undergo detours (see Figure 6.2) resulting in a reduced capability of nullifying the incident field thus diminishing the overall SE.

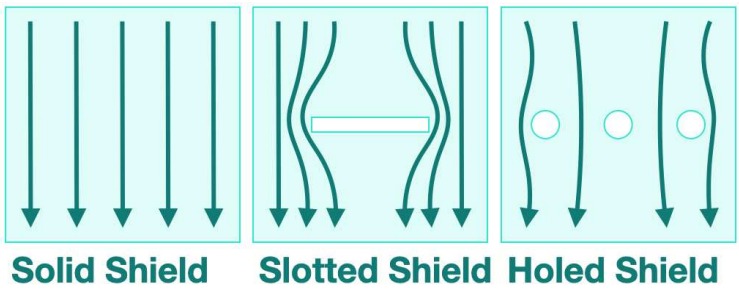

Figure 6.2: Qualitative detouring effect of apertures in shields. It is evident that the bigger the aperture, the greater the detour.

Usually, apertures may be broadly classified in rectangular slots and holes. They can cause notable leakage, especially if they are very narrow, if their length is bigger than $\lambda/10$ because they behave as slot antennas. In particular, this effect has the greater extent whenever the maximum linear dimension is equal to $\lambda/2$. This event occurs because slot antenna theory claims that radiated field from a slot antenna is the same as the one radiated by the relative complementary antenna, apart from the fact that E field and H field are subject to 90° phase shift. A complementary antenna is the one in which the parts are switched: air within the slot is replaced by metal, while metal of the shield takes the place of air. Therefore, a complementary antenna relative to a slot one is a dipole: that is the reason why SE is drastically diminished whenever apertures are present.

Generally, shields may have multiple apertures which additionally worsen SE depending on their number N, the spacing between them and the frequency of the field. Specifically, a linear array of closely distributed apertures (i.e., whenever the latter ones are less than $\lambda/2$ apart) causes an SE drop proportional to the square root of N. Apertures occurring at different shield surfaces do not significantly decrease SE since they radiate in different directions. Finally, if apertures are deployed as a two-dimensional array of holes, just the first row produces a crucial SE decrease since the ones displaced in subsequent

rows do not effectively create additional detours to the induced currents flowing within the shield.

Therefore, as far as the aforesaid assumptions are met, without losing generality, SE in presence of apertures can be assessed as

$$SE = 20log_{10}\left(\frac{150}{fl\sqrt{N}}\right) \tag{6.8}$$

where f is the field frequency expressed in MHz and l is the maximum aperture length measured in m. Recapping, this theory is less rigorous with respect to that of Schelkunoff, since it comes from practical experience, but it is by far more reasonably applicable to sundry real contexts.

6.2 Measurement Setup

Wireless links taking place from the inner to the outer part of a metallic structure are peculiar of application scenarios like asset tracking and monitoring (e.g., freight containers), or smart metering for distributed utility management. In order to assess the performances of the main LPWANs technologies in such contexts, two measurements campaigns were sorted out aiming at comparing several technologies. Through-metal links were tested by sorting out two measurement campaigns so to compare several LPWAN technologies. During the former one, which took place by making use of a decommissioned container, LoRaWAN over $863 - 870$ MHz ISM band, Sigfox, and Amplitude Shift Keying (ASK) modulation over 433 MHz ISM band were involved. On the other hand, during the latter one, which was carried out employing a metallic box, LoRaWAN and NB-IoT were tested.

6.2.1 Measurement Campaign for LoRaWAN, Sigfox and ASK Links

In order to carry out this measurement campaign, three sensor node prototypes were developed. All of them shared the microcontroller, an STM32L053R8 produced by STMicroelectronics [113] that was embedded in a Nucleo board, and the power supply method, two Li-ion batteries ensuring 3600 mAh and 7.4 V [114]. They were conditioned by two voltage regulators: a 2.5 V one (i.e., a MCP1700T-2502E/TT produced by Microchip [115]) powering the microcontroller, and a 5 V one (i.e., a MCP1702T-5002E/CB manufactured by Microchip [116]) for the transceiver at hand. In particular, the LoRaWAN transceiver was the RFM95 produced by HopeRF [117], the Sigfox transceiver was the S2-LP produced by STMicroelectronics [118], while the ASK over 433 MHz

Figure 6.3: Decommissioned container employed for the measurement campaign testing LoRaWAN, Sigfox, and ASK modulation.

transceiver was the FS1000A produced by Summitek Technology [119]. Regarding the receivers, sundry solutions were employed in function of the transmission technology. For LoRaWAN, the same gateway of Section 3.2.1 was adopted, and it was included within the prototype of the LoRaWAN network infrastructure of Figure 3.5. On the other hand, Sigfox does not require to set up receivers, since they are already deployed and installed by Sigfox so to ensure both coverage and data forwarding towards Sigfox cloud. Finally, for what concerns ASK modulation, the receiver was a replica of the sensor node continuously listening for incoming packets.

This measurement campaign was conducted by employing a decommissioned container situated within a landfill (see Figure 6.3). Trials were performed according to the following procedure:

- LoRaWAN was tested using the relative sensor node placed inside the container stuck on its door. A gateway 2 m away from the container door was responsible to collect data conveyed from the inside, and measure the associated RSSIs. SF= 7 was selected since it is the one ensuring the smallest packet ToA thus reducing power consumption;
- Sigfox communication towards the cloud was validated directly from the inside of the container. Likewise the tests concerning LoRaWAN, the sensor node was stuck on the inner side of the container door;
- ASK communication over 433 MHz carrier was examined by installing the transmitter and the receiver at the same location of the container door in turn in the inner and in the outer part.

To reduce the number of involved variables within the experiment, a 12 B test payload was broadcast for each of the technologies. Such a length was selected since it is the maximum payload length Sigfox packets may contain, while LoRaWAN and ASK allow for larger maximum payload sizes. During LoRaWAN and ASK tests 1000 packets were transmitted. On the other hand, only 300 packets were sent during Sigfox tests. PL, RSSI sample means and standard deviations were analysed, except for ASK since the relative transceivers provide no RSSI measures at all. However, PL is the main benchmark to be taken into account so to evaluate the most suitable through-metal transmission technology. Finally, Table 6.1 summarises the test settings.

Table 6.1: Summary of the settings related to the comparative measurement campaign accounting for LoRaWAN, Sigfox and ASK exploiting a decommissioned container.

Transmission Technology	SF	CR	Payload	# Packets
LoRaWAN	7	4/5	12 B	1000
Sigfox	–	–	12 B	300
ASK	–	–	12 B	1000

6.2.2 Measurement Campaign for LoRaWAN and NB-IoT Links

This measurement campaign aimed at comparing the performances of LoRaWAN and NB-IoT for through-metal links. While the previous campaign was sorted out exploiting a container, this one was carried out by making use of a metallic box so to be able to properly apply the model of SE of Section 6.1. Moreover, concerning the sensor node,

the prototype of the multi-protocol transmitter of Section 4.2.2 was exploited. However, for the sake of readability, its characteristics are reported below by making reference to Figure 4.4. Similarly, regarding LoRaWAN, the prototype of network infrastructure of Figure 3.5 was adopted.

The sensor node relied on a Nucleo-L073RZ board produced by STMicroelectronics, which is a general purpose development board embedding an STM32L073 microcontroller. Moreover, two transceivers (i.e., one for each transmission technology) were controlled by the Nucleo board. Such modules were the LoRaWAN transceiver RFM95 produced by HopeRF, driven via SPI, and the NB-IoT transceiver SARA UBee produced by Sodaq, driven via USART. The sensor node was powered by means of a power bank, then the Nucleo board powered both the communication modules. The microcontroller implemented a LoRaWAN Class A device, that transmitted LoRaWAN packets by adopting a frequency diversity scheme over 8 different channels belonging to the $863 - 870$ MHz ISM band. In addition, LoRaWAN packets contained a 10 B test string as payload, and in order to set up a worst case scenario, they were sent by exploiting SF$= 7$, bandwidth of 125 kHz and CR$= 4/5$. The LoRaWAN transceiver was connected to a $\lambda/8$ whip antenna having 2 dBi gain. Instead, the NB-IoT transceiver firstly carried out all the needed routines to join the network, and then it transmitted packets by resorting to the MQTT protocol. Such packets contained an incremental counter and the relative RSSI of the signals the eNodeB sent back to the sensor node. Communication occurred in the $832 - 862$ MHz band via a $\lambda/8$ whip antenna having 2 dBi gain.

The multi-protocol wireless sensor node was tested within a metal box (see Figure 6.4), by measuring losses due to such shield. Despite it had a door, the relative slots were greater than $\lambda/2$, therefore they can be neglected for the evaluation of SE. However, the box had two holes having a diameter of 17.5 mm each: since they were spaced at a distance bigger than $\lambda/2$, just the effect of one of them can be considered to evaluate box SE. Tests were performed by setting up a first set of 300 transmissions for both the technologies in parallel, by placing the sensor node prototype at open air and by measuring and storing the associated RSSIs. Subsequently, the sensor node was housed within the shield and another set of 300 transmissions was done by measuring RSSIs. Finally, losses were evaluated by subtracting RSSIs from the first set of measurements to the ones related to through-metal links. In doing so, experimental losses can be compared to the estimated ones by exploiting the SE model Section 6.1. Table 6.2 summarises the test settings.

Figure 6.4: Test setup for the through-metal links exploiting LoRaWAN and NB-IoT technologies.

Table 6.2: Summary of the settings related to the comparative measurement campaign accounting for LoRaWAN and NB-IoT exploiting a metal box.

Transmission Technology	**SF**	**CR**	**Payload**	**# Packets**
LoRaWAN	7	4/5	10 B	300
NB-IoT	–	–	10 B	300

Regarding LoRaWAN, RSSIs were measured by using the gateway of Section 3.2.1 that was placed 35 m apart from the multi-protocol sensor node prototype. Such distance

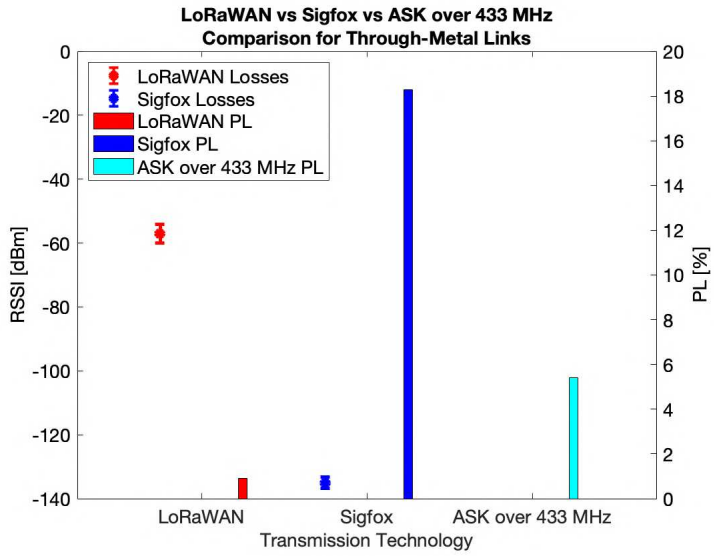

Figure 6.5: Tests results for LoRaWAN, Sigfox, and ASK modulation during the through-metal communication. Notice that for ASK modulation data on RSSIs is missing because of the inability of the receiver to sample such metric.

was chosen because of logistical constraints related to the availability of mains for powering the gateway. On the contrary, the RSSIs of the NB-IoT packets were retrieved by making use of a computer executing an MQTT client subscribed to the same MQTT topic the multi-protocol sensor node published data on.

6.3 Results and Discussion

6.3.1 Measurement Campaign for LoRaWAN, Sigfox and ASK Links

Tests results are reported in Figure 6.5 and in Table 6.3. Through-metal communication enabled by Sigfox reported the highest PL hence pointing out the necessity to employ other communication technologies for such a purpose. In addition, the low RSSIs mean value has to be marginally considered because Sigfox receivers were located far from the testing site. Indeed, they are installed and maintained by Sigfox itself, and users are just allowed to exploit them as they are. Conversely, LoRaWAN RSSIs mean value was much larger because the gateway was placed just outside the container. Therefore, a more

Table 6.3: Through-metal communication results for the tests related to LoRaWAN, Sigfox, and ASK modulation.

Technology	Transmitted Packets	Received Packets	PL [%]	$\bar{x}$ RSSI [dBm]	s RSSI [dB]
LoRaWAN	1000	991	0.9	−57.0	2.9
Sigfox	300	245	18.3	−135.0	1.7
433 MHz ASK	1000	946	5.4	–	–

meaningful metric is the associated PL (i.e., 0.9 %). Finally, despite ASK transceivers are extremely cheap, using such technology in this operation scenario is not advisable because of the non negligible PL. On the whole, this measurement campaign showed the reliability and feasibility of LoRaWAN protocol for through-metal communications, but the most interesting result was that such sort of links were possible and satisfactory.

6.3.2 Measurement Campaign for LoRaWAN and NB-IoT Links

Losses taking place in through-metal links are shown in Figure 6.6 and listed in Table 6.4.

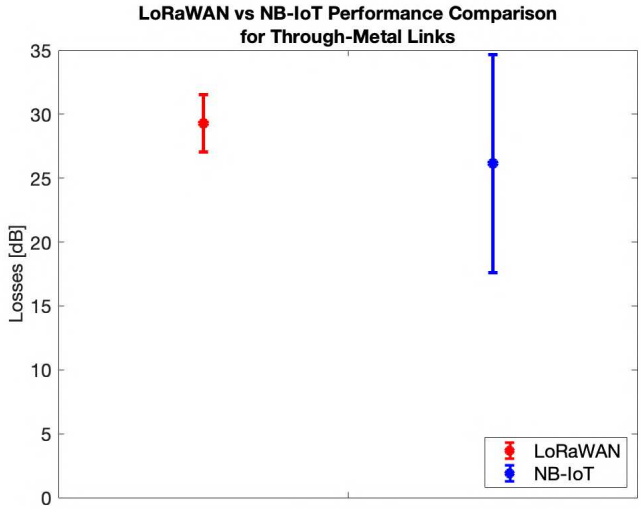

Figure 6.6: Losses mean values and standard deviations due to through-metal links for both the technologies.

Table 6.4: Losses mean values and standard deviations for through-metal links for both the technologies.

	Losses [dB]	
	$\bar{x}$	s
LoRaWAN	29.3	2.3
NB-IoT	26.1	8.5

First of all, no packet loss was experienced, thus remarking the robustness of both the technologies. NB-IoT performed slightly worse than LoRaWAN, especially for what concerns RSSIs standard deviations, but such outcome was due to the fact that NB-IoT links were longer with respect to the LoRaWAN ones because eNodeBs were placed further in contrast to the LoRaWAN gateway. Therefore, such result should not be considered as pivotal. On the contrary, both the technologies can be deemed as reliable in such application scenario.

Measured losses were also compared with the relative estimates according to the models proposed in Section 6.1. The comparison results are reported in Figure 6.7 and in Table 6.5. Unfortunately, SE theory from Schelkunoff could not be applied since the metal box exploited for the test did not meet the underlying assumptions since it had holes. Therefore, Ott model was employed. It turned out to be a relatively good loss estimator: it is fairly reasonable to deem that discrepancies arise due to the fact that such model directly comes from first hand experience on electromagnetic compatibility applications.

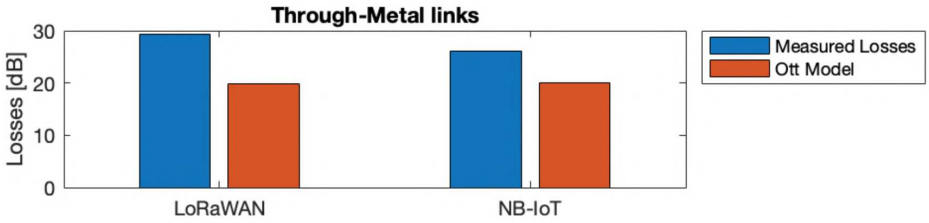

Figure 6.7: Losses comparison between measured and estimated values stemming from the model of Section 6.1 for both the technologies during through-metal links tests.

Table 6.5: Measured through-metal losses in comparison with estimates for both the technologies.

	Losses [dB]		Relative Difference [%]	
	LoRaWAN	**NB-IoT**	**LoRaWAN**	**NB-IoT**
Mean Measurements	29.3	26.1	–	–
Ott Model	19.9	20.1	47.3	30.0

Chapter 7

Industrial Harsh Environments

As it was shown during the presented measurement campaigns in several critical environments, LoRa modulation and LoRaWAN protocol are suitable technologies for the deployment of distributed monitoring infrastructures, in industrial contexts too [120, 121, 122], where extreme environmental conditions may be experienced. Indeed, in several industrial applications, parameters like temperature and humidity may span in a wide range: extremely low or tremendously high temperatures may occur, while elevated humidity levels, nearly up to $100\,\%$, may be present. Furthermore, severe environmental conditions can be characterised by a high vibration intensity (e.g., machineries, turbines and pipelines), and high concentration of various gases such as Nitric Oxide (NO), Nitrogen Dioxide (NO_2) and Carbon Monoxide (CO), which can denote a corrosive atmosphere. For the characterisation of the LoRa transmission channel in these operating conditions is crucial to validate the usability of this technology for remote data acquisition within the context of the IIoT. To this end, several testing setups taking place in such harsh operation scenarios typical of industrial monitoring are shown herein.

7.1 Measurement Setup

In order to study the behaviour of LoRaWAN transmitters whenever the relative electronics is exposed to a wide range of temperature and humidity values (i.e., from very low to the most extreme ones), as well as to machinery vibration and NO, NO_2 and CO gases, dedicated measurement campaigns were set up. In particular, tests were carried out by performing several transmissions putting the transmitter in different environmental conditions by employing a climatic chamber, an ad-hoc vibration test bench and a fume extraction plant, thus having full control on both temperature and humidity, vibration frequency and amplitude, and gases concentration, therefore obtaining a controlled environment. Such working conditions are typical of industrial contexts (e.g., oil and gas field), where wireless communication technologies can be used to establish pervasive monitoring infrastructures.

7.1.1 Temperature and Humidity, Corrosive Gaseous Atmospheres, and Vibrating Systems Characterisation

Temperature is important due to the effects on semiconductor diffusion and threshold changes in integrated amplifiers, impurity diffusion, material mismatch and electronic noise generation [123, 124, 125, 126, 127]. On the other hand, humidity plays an important role too considering that at specific points where water vapour becomes liquid (i.e., dew points) such amount of water may induce, on the long run, rusting on contacts and local short circuits. Therefore, it leads to uncontrolled and undesired system behaviours, up to premature and unpredictable failures which may result in a catastrophic system outcome. These considerations also apply to specific wireless transmission systems operating into open environments which are subject to environmental excursions and sudden seasonal variations. Nevertheless, such effects may affect even systems deployed into enclosed systems (e.g., IP67, or higher rating, boxes) due to the fact that the water content trapped inside the housing during maintenance activities may change status several times affecting different circuit parts due to temperature cycling.

The standard DIN EN 60721.3.3 is mainly used to specify corrosive environments by manufacturers making products that are commonly used in these settings. Nevertheless, this standard does not address the way tests should be conducted. Therefore, the lack in quantitative evaluation criteria and missing thresholds may lead to inconsistent testing plans within products development planning. As a result, testing using mixed gases based on specific company experience is utilised in industry to demonstrate compliance with the specified requirements.

Vibrations were extensively studied and used by companies to verify compliance with actual usage conditions. Moreover, such tests were proposed to prove the possibility to create ageing models and enhance failure mechanisms connected to single components or electronic assemblies [128, 129, 130, 131]. However, in such papers the authors tried to investigate a very limited set of frequencies of interest in industrial applications to verify whether electronics transmission capabilities of wireless devices are affected on short-term exposure.

7.1.2 Transmitter-Receiver Architecture

Tests were performed employing the following devices. The transmitter node was composed of an ATtiny84A-SSU microcontroller produced by Microchip, an RFM95 LoRa transceiver manufactured by HopeRF and a $2\,\mathrm{dBi}$ gain omnidirectional antenna. The microcontroller features an $8\,\mathrm{kB}$ flash program memory and an industrial functioning temperature in the range $-40\,^{\circ}\mathrm{C}$ to $85\,^{\circ}\mathrm{C}$. Finally, the node was powered using a $3400\,\mathrm{mAh}$

NCR18650B Li-ion battery produced by Panasonic. In order to reduce the number of the involved variables within the experiments, all the electronics forming the transmitter were embedded within a Printed Circuit Board (PCB). To this end, many PCBs were realised in order to make replicas of the same device so to employ different clones for each of the testing setup. The receiver part was characterized by an LG308 Dragino LoRaWAN gateway for the tests related to temperature and humidity effect, while for the tests on vibration and gas impact on transmissions a RAK2245 LoRaWAN gateway was used. Both the receivers share the same electronics (that is the same of the RAK831), and they were provided with the same antenna, therefore we assume they ensure the same performances.

7.1.3 General Methodology

Tests aiming at assessing the effect of temperature and humidity were carefully carried out within a climatic chamber (i.e., the ACS Angelantoni HYGROS 250 environmental test chamber) which permitted to precisely control temperature and humidity values. Similarly, tests concerning the impact of gas exposure on transmission performances were accomplished within a fume extraction plant for safety reasons and for ensuring a controlled environment as well. Likewise, the dependence of transmission performances on vibrations was evaluated by resorting to an ad-hoc vibration test bench that allows to precisely set vibration frequency and amplitude which are strictly related to acceleration.

Experimental tests were sorted out according to the following methodology. Tests on temperature and humidity, on gas exposure and on the effect of vibrations were comprised of many measurement sets, each consisting of three batches during which the sensor node sent 1000 LoRaWAN packets, and at the same time, RSSIs were sampled by the gateway. This decision was adopted so to average measurements from the three batches of a single set in order to even out undesired disruptive phenomena which are not related to temperature or humidity, gases or vibration influence (e.g., fast fading effects).

While the tests on temperature and humidity and the ones on gas exposure were accomplished by making use of a single SF for the transmission of the LoRaWAN packets (i.e., SF$= 12$), all the SFs were tested during trials on vibrations. Such a choice was selected in order to find out probable correlations between the SFs and the movement resulting from vibrations. The remaining transmission parameters were shared between all of the tests within the whole measurement campaign. In particular, a bandwidth of 125 kHz, a CR of $4/5$, a packet payload of 10 B, and eight different channels within the $863 - 870$ MHz band (so to establish a frequency diversity scheme) were used. For what concerns the transmitter power output P_{TX}, three different values were selected (i.e., -80 dBm, 0 dBm and 14 dBm). In doing so, not only was the effect of the aforementioned

agents investigated, but also the reception capability of the system at different levels of received power was assessed. Eventually, considering that evaluating the performances of the battery powering the transmitter falls outside the scope of this Thesis, it was not included within the experimental sites, and the node was activated by passing power cables through cable glands.

7.1.4 Temperature and Humidity Test Setup

Regarding the tests within the climatic chamber, transmitter and receiver were respectively put inside and outside it (see Figure 7.1): taking into account the chamber door, the former was located 10 cm-distant from it, while the latter was 40 cm-distant.

(a) (b)

Figure 7.1: Testing setup within the climatic chamber: (a) transmitter within the chamber, (b) gateway and transmitter placed one in front of the other.

The climatic chamber is thought to precisely set temperature and humidity values in order to perform environmental tests. However, it is important to point out that for each temperature value the humidity concentration range is limited to certain values defined by psychrometric principles. For instance, for negative temperatures it is not possible to set a desired relative humidity. Similarly, relative humidity higher than $90\,\%$ cannot be reached for positive temperatures. On the other hand, minimum relative humidity ranges from $60\,\%$ at $10\,°\mathrm{C}$, down to $20\,\%$ at $30\,°\mathrm{C}$ and finally down to the minimum of $10\,\%$ for temperatures from $50\,°\mathrm{C}$ and over. Such shortcomings entailed that not all of the relative humidity values may be freely spanned. Thus, tests were sorted out throughout twelve environmental sets, each of which was characterized by its own temperature and humidity pair: $-25\,°\mathrm{C}$ and $-10\,°\mathrm{C}$ for negative temperatures while $10\,°\mathrm{C}$, $30\,°\mathrm{C}$, $50\,°\mathrm{C}$, $70\,°\mathrm{C}$

Table 7.1: Summary of the settings related to the field measurement campaign for LoRaWAN links in harsh temperature and humidity conditions.

Transmission Technology	**P_{TX} [dBm]**	**SF**	**CR**	**Payload**	**# Packets**	**Temperature Values [°C]**	**Humidity Values [%]**
LoRaWAN	-80, 0, 14	12	$4/5$	10 B	1000 for each P_{TX} and temperature and humidity pair	-25, -10, 10, 30, 50, 70, 90	10, 20, 60, 90

and 90 °C for the positive. Concerning the latter ones, relative humidity was only tested for the minimum and maximum achievable value for each of the temperatures. Table 7.1 summarises the test settings.

Tests were compliant with IEC 60068-2-1, IEC 60068-2-2 and IEC 60068-2-78 for cold, dry heat and damp heat environmental testing standards respectively. These standards describe approaches which are directly related to specimen characteristics and temperature changes over time. According to them, the specimen under test (i.e., the transmitter) can be considered as non-heat dissipating. As a matter of fact, the hottest point on its surface is always 5 °C below the ambient temperature of the environment after temperature stabilisation. In this measurement campaign, the non-heat dissipating specimen was exposed to a gradual change of temperature. Consequently, the test methods that corresponded to each of the aforementioned IEC standards were:

- Test Ab for cold environment;
- Test Bb for dry heat environment;
- Test Cab for damp heat environment.

Figure 7.2 depicts the temperature profiles for cold and hot tests, which were deduced by the aforementioned IEC standards. More specifically, the tests followed the subsequent approach. The specimen was introduced into the climatic chamber at laboratory temperature. The chamber was turned on and the temperature was gradually augmented to reach the desired value with a rate of 1 °C per minute. As soon as the system reached the target temperature, the transmitter was turned on the data acquisition started. Once the test set at hand was over, the temperature was gradually settled to the laboratory one with a rate of 1 °C per minute. The specimen remained in this condition for at least 1 hour to allow the whole thermodynamic system to get to the steady state. During the measurement period, the chamber provided a stable temperature and relative humidity with ± 2 °C and ± 3 % accuracy, respectively. Throughout these tests, the transmitter was

not coated at all in order to expose the hardware to the harshest possible conditions to assess whether the transmission performances suffered from such a testing condition or not.

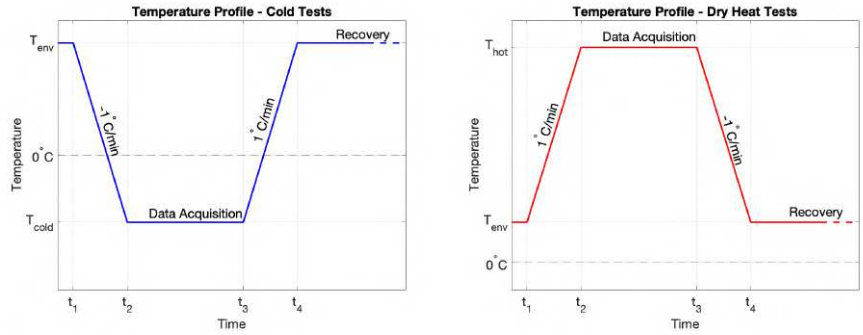

Figure 7.2: Adopted temperature profiles for the temperature and humidity tests according to the IEC standards: (a) Cold Tests, (b) Dry Heat Tests.

7.1.5 Gas Test Setup

Tests on gas effect were accomplished in order to expose the transmitter to an atmosphere composed of a fixed concentration of a target gas diluted in a carrier gas consisting of N_2. The test was repeated for three target gases: CO (with a concentration of 200 ppm in N_2), NO (with a concentration of 50 ppm in N_2) and NO_2 (with a concentration of 50 ppm in N_2). The transmitter was put in a containment box in which a constant flow (i.e., 100 mL/min) of the gas mixture was fluxed. The box had an inlet pipe, supplied with the gas mixture flow, and an outlet pipe to let out the mixture. The gas mixture flow was obtained by mixing a sample gas mixture, from reference gas tanks, with N_2 by means of two mass flow meters: for both, the full-scale flow was 200 mL/min. The used mass flow meters were the Bronkhorst F201C. One flow meter was used to set a flux of N_2 and the other one was used to dose a mixture of the target gas. The two gas flows were mixed obtaining a constant total flux of 100 mL/min at the required concentration. The mass flow meters controller was connected to a PC hosting a LabVIEW program allowing an automatic control of the test. Once that the transmitter was housed within the containment box, the gas mixture was fluxed within the latter for two hours so to let it act on the electronics. Such box was placed within the fume extraction plant 10 cm-distant from the plant door, while the gateway was placed outside the plant 40 cm-distant from

the door (see Figure 7.3). Then, the three batches were sequentially accomplished. The experiments on gas exposure were compared with two control tests. Both of them were sorted out by placing the transmitter and the receiver one in front of the other at a distance of $50\,\text{cm}$, and in the same position (i.e., the node within the fume extraction plant and the gateway outside the latter). The former was carried out before proceeding with the current fume exposure in order to collect a reference. On the other hand, the latter, which can be named as post experimental set, was executed 24 hours after the fume exposure so to assess whether the gases detrimental effect is permanent or not. Finally, Table 7.2 summarises the test settings.

Figure 7.3: Gas exposure test setup showing the transmitter within the containment box and the gateway in front of the fume extraction plant.

Table 7.2: Summary of the settings related to the field measurement campaign for LoRaWAN links in corrosive gaseous atmospheres.

Transmission Technology	**P_{TX} [dBm]**	**SF**	**CR**	**Payload**	**# Packets**	**Target Gas**
LoRaWAN	-80, 0, 14	12	$4/5$	$10\,\text{B}$	1000 for each P_{TX} and target gas	CO NO NO_2

7.1.6 Vibration Test Setup

In order to evaluate the performances of the transmitter in presence of external vibrations, a vibration test bench (see Figure 7.4) was sorted out, where the vibration source was a modified loudspeaker actuated by a power amplifier [132].

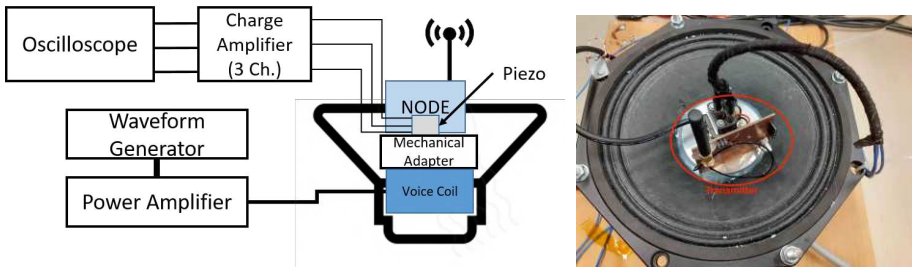

(a) (b)

Figure 7.4: Vibration test bench: (a) block scheme, (b) hardware implementation with the transmitter placed on the aluminum support disk.

The loudspeaker was modified by mounting a rigid aluminum disk on the diameter of the voice coil which was used as a support for the sensor node and a reference accelerometer. The voice coil had a diameter of 65 mm, such as the one of the aluminum disk. The payload given by the disk, the transmitting node and the accelerometer can be easily driven by the 700 W coil of the speaker and the 1 kW power amplifier. The reference accelerometer was needed to measure the acceleration of the vibration exerted by the loudspeaker itself. The adopted accelerometer was a triaxial piezoelectric B&K 4326A coupled with a three channel piezo amplifier [133]. The tests were performed by vibrating the transmitter with sinusoidal vibrations at known accelerations and specific frequencies. In particular, the tested frequencies spanned from 25 Hz to 285 Hz with variable amplitudes providing acceleration from 3.14 m/s^2 to 17.90 m/s^2. Moreover, for frequencies lower or equal to 125 Hz the vibration amplitude was set so that a speed of 0.02 m/s was ensured, while for higher frequencies the amplitude was set in order to produce a speed of 0.01 m/s. In addition, a set of transmissions was performed when the system was still (i.e., vibration frequency equal to 0 Hz) in order to collect a reference sample. The selected speed amplitudes and corresponding frequency ranges were chosen because these are the ones that are requested by all the electronic devices exploited in industrial monitoring (e.g., offshore applications in oil and gas context). Additionally, the proposed speed levels result in a higher severity with respect to the IEC 60068-2-6 standard for sinusoidal testing. For this purpose, a signal generator was used to feed the

Table 7.3: Summary of the settings related to the field measurement campaign for LoRaWAN links subject to vibrations.

Transmission Technology	**P_{TX} [dBm]**	**SFs**	**CR**	**Payload**	**# Packets**	**Vibration Values [Hz]**
LoRaWAN	-80, 0, 14	7, 8, 9, 10, 11, 12	$4/5$	10 B	1000 for each P_{TX}, SF and vibration value	0, $25 - 285$

loudspeaker power amplifier. To adjust the output level of the signal generator, the output of the accelerometer charge amplifier was monitored. In particular, the charge amplifier was set to provide 1 V/g, and the vibration level supplied to the node was adjusted by controlling the amplitude of the signal coming from the charge amplifier itself. Since such tests were conducted at low frequencies, the transmitter was fixed onto the aluminum disk support by making use of hot glue, and it was placed 50 cm apart from the LoRaWAN gateway. Similarly as before, the transmitter was a brand new PCB so to reduce the number of experimental variables. Finally, Table 7.3 summarises the test settings.

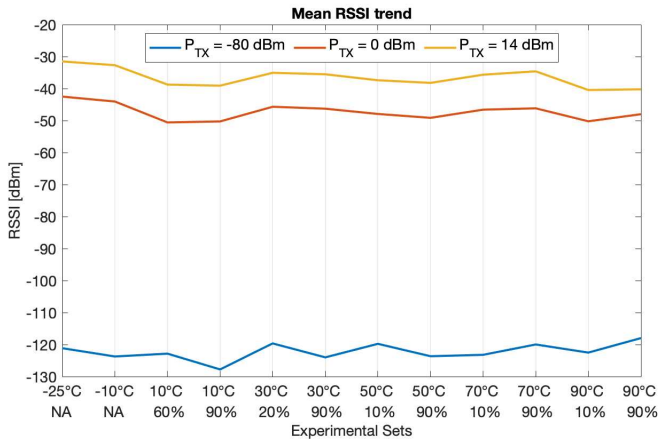

Figure 7.5: Mean RSSI trend throughout the different measurement sets whose values of both temperature and relative humidity are reported in the abscissa. NA for relative humidity stands for the inability to set such parameter for negative temperatures.

7.2 Results and Discussion

7.2.1 Temperature and Humidity Test Results

Figure 7.5 shows the RSSI values during the twelve measurement sets, for each of the P_{TX}, related to the tests within the climatic chamber that are distinguished by their own temperature and humidity values, that are reported on the abscissa of the chart in Figure 7.5. A performance drop as temperature increases can be noticed, but it seems that such a tendency was not exactly confirmed for humidity rises. Indeed, at constant temperature values, RSSIs did not particularly suffer from humidity increments.

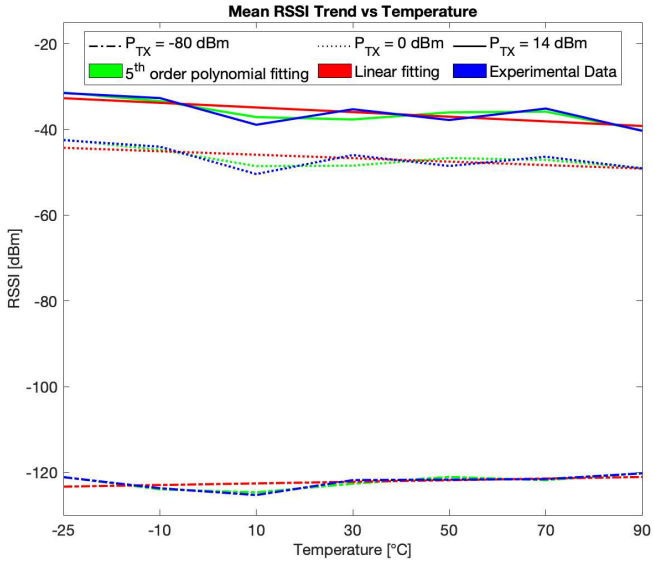

Figure 7.6: Mean RSSI trend in function of temperature.

Moreover, temperature results did not follow a linear behaviour. Indeed, within Figure 7.6 experienced RSSI values for any tested temperature were averaged and plotted in function of temperature so to check the aforementioned linear correlation: it was evident that dependence amid RSSI and temperature may be adequately approached by a 5^{th} order polynomial curve rather than by a linear trend.

Figure 7.7 qualitatively presents the results of the temperature and humidity tests by means of a pseudocolor plot where blank cells stand for unfeasible experimental

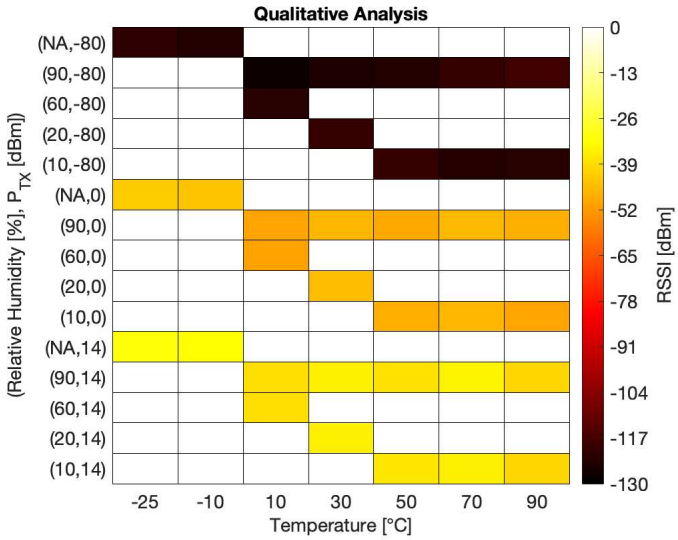

Figure 7.7: Qualitative RSSI analysis in function of temperature and relative humidity. Blank cells represent unobtainable experimental conditions, while NA remarks the fact that no relative humidity can be set for negative temperatures.

conditions due to the aforesaid constraints stemming from the operation modes of the climatic chamber. Yet again, the dependence on temperature and humidity of the suitable electronics for LoRaWAN transmissions is underlined. Indeed, all of the tests were aimed at investigating hardware behaviour rather than channel performances since only a limited leg of the link (i.e., 10 cm) was subject to controlled variations of temperature and humidity. Sure enough, temperature directly hinders hardware performances since thermal noise becomes more and more prevailing according to Johnson–Nyquist derivation

$$N_T = 10log_{10}\left[\frac{K_B \cdot T \cdot BW}{0.001}\right] \tag{7.1}$$

where N_T is thermal noise expressed in dBm, K_B is Boltzmann constant, T is the temperature expressed in K and BW is the bandwidth in Hz. Under these assumptions it is evident that temperature variations, and thermal cycling in particular, have an influence on the induced noise by analog and digital electronic components. The increase in the electron junction ionisation activity with temperature justifies the reason why the aforesaid parameters negatively affect transmission performances. Concerning the humidity contribution, it is possible to notice that an increase of the water content in air

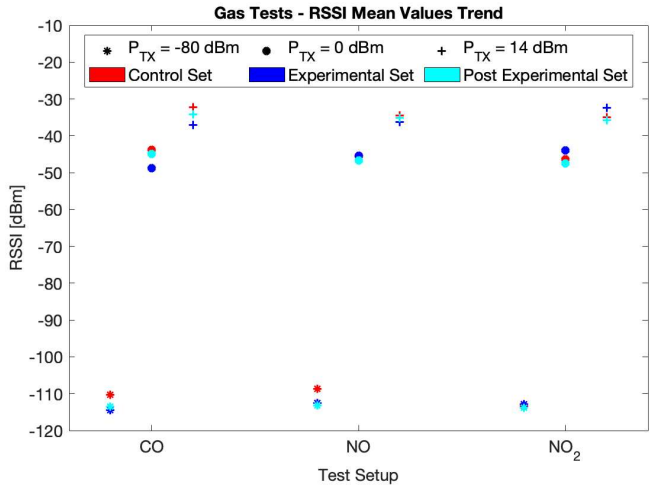

Figure 7.8: Mean RSSI trend in function of the target gas compared with both the control sets.

enhances communication capabilities. This may be justified by the increased thermal capacity of water vapour with respect to dry air, and with a local lowering of the junction temperature of the single involved components.

7.2.2 Gas Test Results

Figure 7.8 shows the RSSI mean values of the gas exposure test sets in comparison with both the control ones. First of all, no packet loss arose during each of the testing setups. Moreover, and as it can be drawn from the plot, no significant disruptive effects occurred, both immediately after the exposure and several hours later. Indeed, at a given P_{TX}, only slight differences amid mean RSSIs throughout the three test sets (i.e., the control, the experimental and the post experimental ones) were measured. In particular, when $P_{TX} = -80\,\text{dBm}$ such discrepancies were respectively of $4.2\,\text{dB}$, $4.5\,\text{dB}$ and $1.0\,\text{dB}$ in turn for CO, NO and NO_2. Similarly, when $P_{TX} = 0\,\text{dBm}$ such differences were respectively of $4.9\,\text{dB}$, $1.3\,\text{dB}$ and $3.6\,\text{dB}$ in turn for CO, NO and NO_2. Finally, when $P_{TX} = 14\,\text{dBm}$ such variations were respectively of $4.7\,\text{dB}$, $1.7\,\text{dB}$ and $3.4\,\text{dB}$ in turn for CO, NO and NO_2. On the whole, performance drop due to gas exposure is relatively limited and it can be compared to other disruptive causes which are likely to happen in whichever wireless link. In addition, despite the corrosive capabilities of NO_2 whenever water traces are present in the atmosphere, the electronics and the technology

are robust enough that no hindrances to the transmission system were experienced. Therefore, it can be concluded that the proposed system (i.e., both the hardware and the communication infrastructure) can be beneficially employed within all the IIoT scenarios that are intrinsically characterised by harsh gaseous atmospheres.

7.2.3 Vibration Test Results

Figure 7.9 and Figure 7.10 display RSSI mean values of the vibration test sets. These tests highlighted an interesting result concerning the effect of the detrimental agents (i.e., vibration and acceleration) on transmission performances by varying the SF, which are in line with a previous work entailing LoRaWAN transmissions from moving vehicles [35]. In particular, RSSIs at a given frequency or acceleration, and at a given transmitter power output, are very close to each other regardless of the SF. Indeed, discrepancies are always no bigger than 6.0 dB. On the contrary, what is strongly varying is the number of received packets. While no loss occurred whenever $P_{TX} = 0$ dBm and $P_{TX} = 14$ dBm, no matter what SF was exploited, no data was barely received for $P_{TX} = -80$ dBm whenever SF$= 8$ and SF$= 7$ were selected. In particular, at SF$= 7$ data was only received at the vibration frequencies of 135 Hz and 145 Hz the 21 % and the 6 % of the times in turn. Similarly, at SF$= 8$ no data was received at the vibration frequencies spanning from 165 Hz to 275 Hz, while it was correctly received from the 1 % to the 94 % of the times for the other tested frequencies. Such results may be considered as spurious because they seem to be the consequence of external effects rather than systematic outcomes. This hinted at the fact that higher SFs are by far preferable whenever the transceiver is subject to vibrations and a low transmitter power output is used in order to limit consumption, and this is due to the fact that the receiver sensitivity proportionally grows along with the SF. All in all, apart from the just mentioned cases, it can be drawn that no significant correlation between RSSI degradation and vibration or acceleration can be found, and that successful data transmission is ensured even when exiguous transmitter power output values are used. However, another result is that vibrations do affect RSSI on the whole. Indeed, independently on the SF, an average drop of 3.0 dB can be experienced between measurements at 0 Hz and at 25 Hz when $P_{TX} = -80$ dBm. Similarly, such drop averagely becomes bigger as P_{TX} increases: 10 dB if $P_{TX} = 0$ dBm, and 12.0 dB if $P_{TX} = 14$ dBm. These results are also in agreement with the ones in [134] where an RSSI drop is experienced whenever a sensor node, exploiting a different wireless technology than LoRaWAN, undergoes vibrations. However, possible motivations for such an effect could be the Doppler shift owing to the movement due to vibrations, or even by the fact the vibration test bench can generate electromagnetic noise affecting the hardware forming the transmitter. Nevertheless, such degradation does not undermine

the system reception capabilities thus underlying the robustness of LoRa modulation and LoRaWAN protocol.

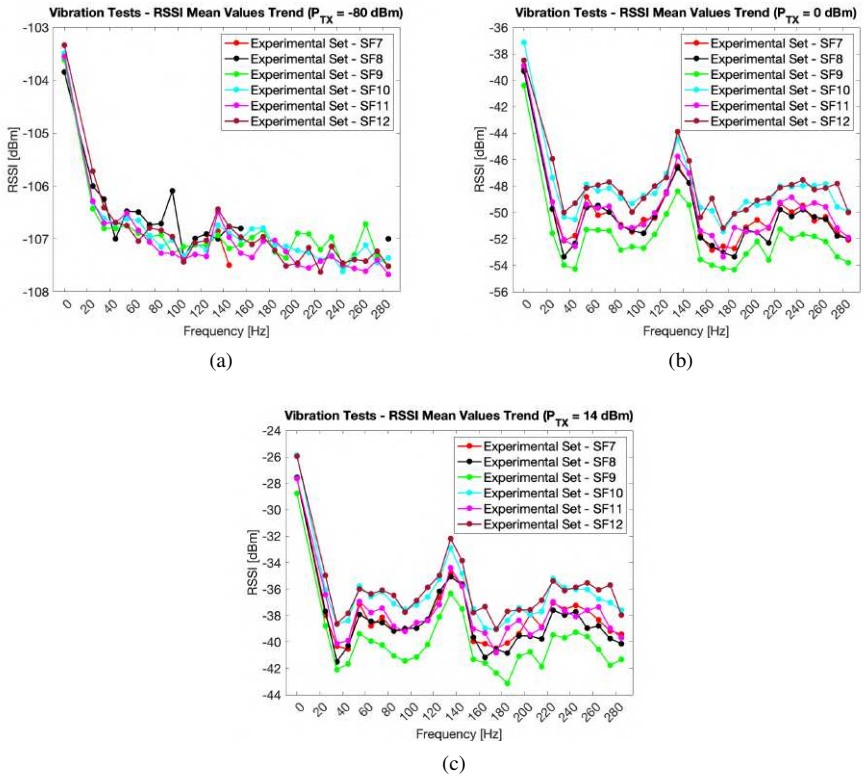

Figure 7.9: Mean RSSI trend in function of vibration frequency for all the SFs. Each plot refers to a different transmitter power output: (a) −80 dBm, (b) 0 dBm, (c) 14 dBm.

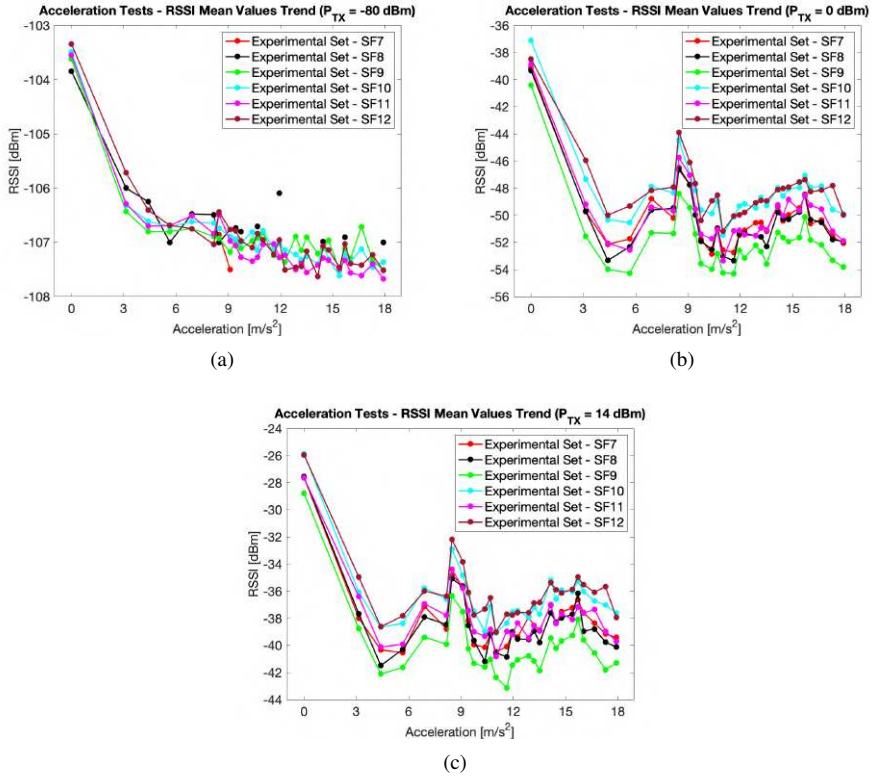

Figure 7.10: Mean RSSI trend in function of acceleration for all the SFs. Each plot refers to a different transmitter power output: (a) -80 dBm, (b) 0 dBm and (c) 14 dBm.

Chapter 8

IoT Measurement Infrastructures Deployed in Critical Environments

This Chapter shows two IoT measurement facilities that were developed and deployed in as much harsh contexts. Specifically, the former is a LoRaWAN network infrastructure for the remote monitoring of offshore sea farming plants, while the latter is a facility set up to assess the relationship between VWC and RSSIs in UG2AG links. Indeed, such results are preliminary in order to develop an augmented sensor for VWC to be employed within precision agriculture scenarios.

8.1 LoRaWAN Network Infrastructure for the Remote Monitoring of Offshore Sea Farming Plants

This system directly stemmed from the successful results of the measurement campaigns of Section 3. Indeed, the infrastructure was composed of an offshore sensor node installed on board of a seamark buoy, and of a Video Surveillance Unit (VSU) installed on board of the breeding cages floating structure.

8.1.1 Seamark Buoy Sensor Node

8.1.1.1 System Description

The system was grounded on the prototype of the prototype of the LoRaWAN network infrastructure of Figure 3.5. Similarly, the space diversity scheme for the gateways was adopted owing to the good results of the short-term campaigns of Section 3. Conversely, the complete system underwent a test lasting 70 days.

The sensor node was installed on board of the seamark buoy (see Figure 8.1), placed in point A of Figure 3.8.

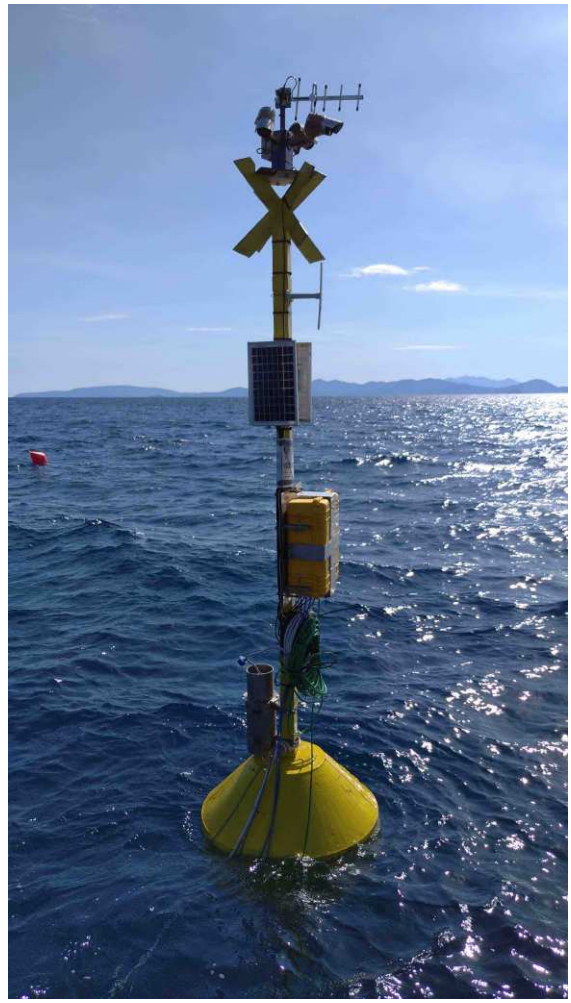

Figure 8.1: Seamark buoy on which the sensor node was installed.

The sensor node was housed within an IP67 box along sundry electronics dealing with sensor sampling (i.e., submerged marine probes). However, apart from the fact that it communicated via a serial interface, no additional details are provided since such hardware was designed by a third-party company. Therefore, the sensor node acted as a RS232 – LoRaWAN interface (see Figure 8.2) whose purpose was to arrange data coming from sensors in LoRaWAN packets and to broadcast such information ashore by covering an 8.33 km distance.

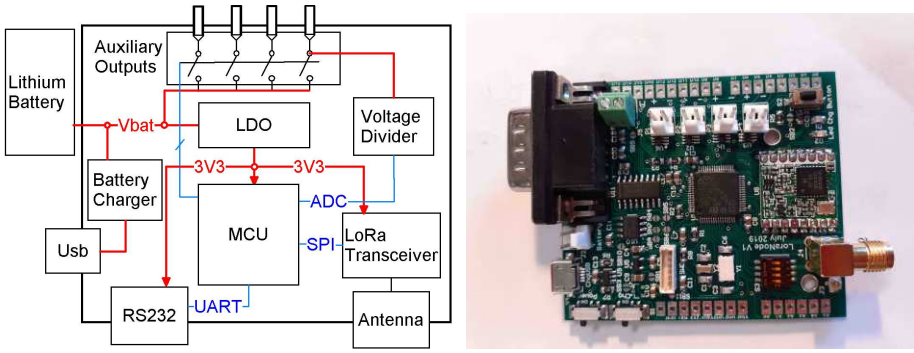

(a) (b)

Figure 8.2: Sensor node embedded system: (a) block diagram; (b) board without battery and antenna.

Albeit the seamark buoy hosted two photovoltaic panels, the sensor node board was designed in order to be battery powered. Indeed, the panels were solely necessary to supply the sensors probes and the front-end electronics because they were the power hungrier elements. Since the sensor node had to be low-power, the following components were embedded into it: an STM32L073 microcontroller produced by STMicroelectronics, an RFM95 LoRa transceiver manufactured by HopeRF (which relies on an SX1276 LoRa module produced by Semtech) and miscellaneous low power electronics. Finally, the system was powered by a 3600 mAh Li-ion battery providing 3.7 V. Moreover, a sampling period of 1 h was selected. In particular, all the data was split in 3 LoRaWAN packets that were sent 3 times in order to overcome losses which naturally came into play, as it was proven during the short-term measurement campaigns of Section 3. Concerning the transmission parameters, packets were broadcast exploiting a bandwidth of 125 kHz, an SF of 7 and a CR of $4/5$ since, by resorting to results of previous short-term trials, such settings proved to be successful while minimising power consumption. Moreover, the sensor node sent packets exploiting a power output of 14 dBm and respecting the laws on the temporal occupancy of the exploited ISM band (i.e., devices have to respect a duty cycle of 1 %). The packets were broadcast to any gateway in the vicinity establishing a frequency diversity scheme via a frequency hopping technique amid 8 different channels belonging to the $863-870$ MHz ISM band. Finally, a 9 dBi Yagi-Uda antenna mounted on top of the seamark buoy (i.e., at 2.00 m above sea level) was exploited for the transmission. The connection between the antenna and the sensor node was established by means of a 4.00 m-long coaxial cable whose loss was 2.10 dB.

Two gateways were installed as in Figure 8.3, and they were connected to two directional helical antennas whose gain is 14 dBi each, which were installed at an altitude

of 5.00 m above sea level. The connection was performed via two 15.00 m-long coaxial cables whose individual loss was 4.06 dB, while Internet connectivity was provided by a 4G LTE router.

Figure 8.3: Gateways and their antennas in the installation site for setting up the LoRaWAN infrastructure monitoring offshore sea farms.

8.1.1.2 Tests Setup and Results

In order to avoid data compression on-board of the sensor node, the sensor measurements were arranged in 3 LoRaWAN packets whose payloads had a variable size: one of 51 B and the other two of 106 B. Such a choice was motivated by the fact that regional regulation on the exploitation of ISM bands does not allow to sort out all the measurements only within 2 packets since their payload would be too long. Moreover, as stated beforehand, in order to reduce the probability of data loss, those 3 packets were sent 3 times to establish a redundancy paradigm. Therefore, the ashore system operated

according to the following scheme:

A. The sensor node retrieved the samples from the probes conditioning electronics;

B. It arranged the data within 3 LoRaWAN packets;

C. It broadcast the packets 3 times;

D. It entered in sleep mode until new measurements were sampled, and then it restarted the cycle from step 1.

Such a procedure took 62 minutes and 51 seconds (i.e., 2 minutes and 44 seconds for accomplishing steps from 1 to 3 since packets were sent abiding by regional regulations on temporal occupancy of ISM bands, while 60 minutes and 7 seconds were spent in step 4). Hence, according to the aforesaid procedure, during 70 days of tests 14220 packets were transmitted from the ashore buoy. Finally, Table 8.1 summarises the test settings.

Table 8.1: Summary of the settings related to the field measurement campaign for LoRaWAN seamark buoy sensor node.

Transmission Technology	$\mathbf{P}_{TX}$	**SF**	**CR**	**Payload**	**# Packets**	**Distance**
LoRaWAN	14 dBm	7	4/5	51 B, 106 B	14220	8.33 km

The first instance of system performances is the overall number of received packets out of the transmitted ones which was 10301 out of 14220 (i.e., 72.44 %). In addition, the number of received packets for each of the channels the sensor node exploited for performing frequency diversity was evaluated and the results are reported in Table 8.2. Finally, mean values and standard deviations for RSSIs and SNRs were taken into account. In particular, they were firstly computed either for the whole amount of data and for data split by date, and then they were evaluated by dividing data according to weather conditions as well as to atmospheric temperature, relative humidity and atmospheric pressure. Indeed, all of the meteorological information were associated to each of the received packets by resorting to the Application Program Interfaces (APIs) that are offered by OpenWeather [135]. The results related to RSSIs and SNRs concerning all of these cases are reported in Table 8.3 and in Figures 8.4, 8.5, 8.6, and 8.7.

Table 8.2: Number of received packets for each of the channels.

Channel [MHz]	Received Packets
867.1	1466
867.3	1449
867.5	287
867.7	1454
867.9	887
868.1	1901
868.3	1426
868.5	1431

Table 8.3: Mean values and standard deviations of RSSIs and SNRs for the experienced weather conditions.

	RSSI		SNR [dB]	
	$\bar{x}$ [dBm]	$\bar{s}$ [dB]	$\bar{x}$	$\bar{s}$
Total	-114.3	2.3	-1.34	2.53
Clear Sky	-114.2	2.3	-1.30	2.58
Few Clouds	-114.5	2.3	-1.48	2.48
Scattered Clouds	-114.5	2.4	-1.34	2.50
Cloudy	-114.4	2.2	-1.18	2.32
Light Rain	-115.0	2.2	-1.90	1.98
Moderate Rain	-115.5	1.9	-2.57	1.65
Heavy Rain	-116.8	1.5	-2.42	2.03
Fog	-113.9	2.6	-2.58	3.09

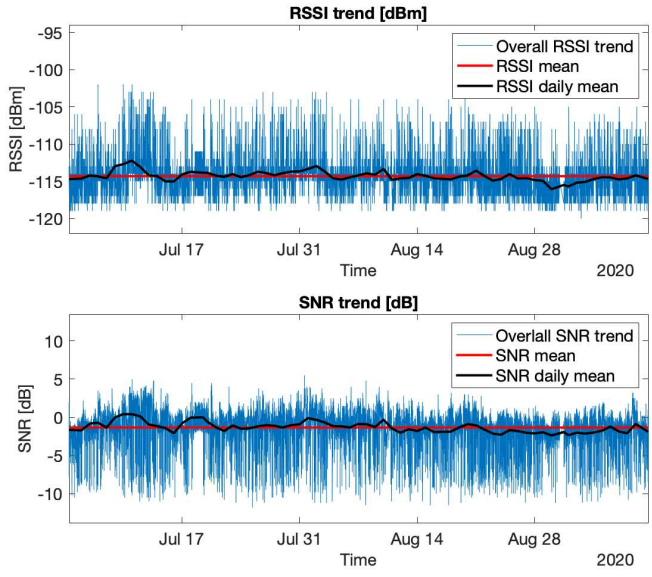

Figure 8.4: Overall trend for RSSIs and SNRs along with total and daily means.

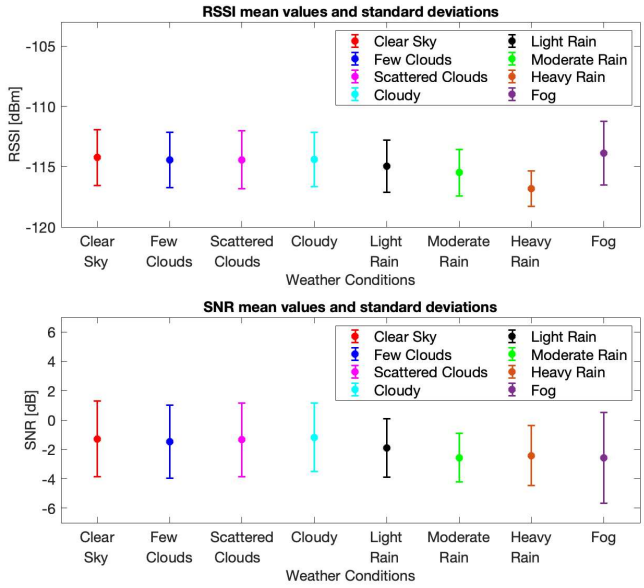

Figure 8.5: RSSIs and SNRs mean values and standard deviations divided by weather conditions.

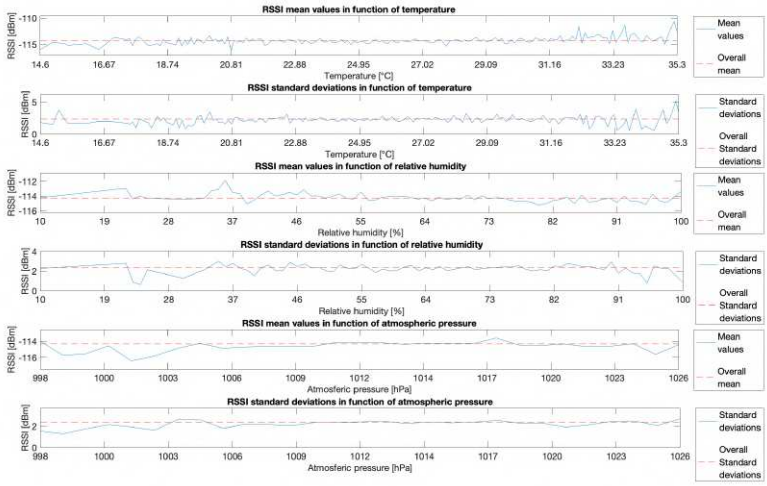

Figure 8.6: RSSIs mean values and standard deviations divided by temperature, relative humidity and atmospheric pressure.

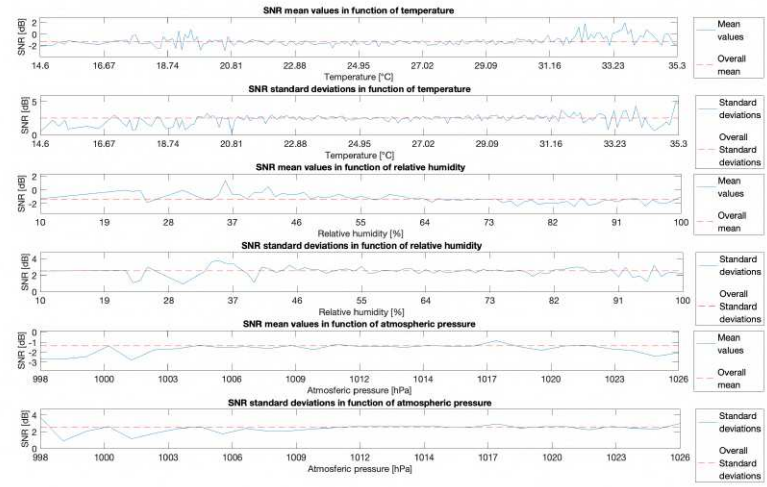

Figure 8.7: SNRs mean values and standard deviations divided by temperature, relative humidity and atmospheric pressure.

According to the collected data throughout the 70-day measurement campaign, interesting considerations about the performances of LoRa transmission channel in sundry meteorological conditions can be drawn. Indeed, during the data collection period, a wide range of different relative humidity values was experienced (i.e., from $10\,\%$ to $100\,\%$). The same occurred for atmospheric pressure, whose values were measured between $998\,\text{hPa}$ and $1026\,\text{hPa}$. Concerning the temperature, the measured range was notably shorter since the measurements took place only in summer (i.e., from 14.6° C to 35.3° C): nevertheless, it is well known that the higher the temperature, the higher the thermal noise, thus SNR values tend to decrease. This means that, since 35.3° C can be assumed as one of the highest achievable temperature values for the deployment site, the transmission channel was analysed in worst case scenario.

Tests results proved that weather affects transmission performances. Indeed, across the testing period, a wide range of different weather conditions were experienced: from clear sky to heavy rain and fog. Unfortunately, all of them were experienced during the same season (i.e., summer), but it is clearly visible from Figure 8.5 that performances worsen in case of rain. As it will be mentioned below, this is in accordance with the signal degradation that is noticeable at high relative humidity levels and makes this parameter the only one that can significantly affect the actual transmission capabilities for the LoRa technology. Performances during fog showed a strange behaviour since the maximum mean value for RSSI was experienced. Such a fact is an oddity because fog is an aerosol made of tiny water droplets. However, this had a limited significance since only 8 samples were collected owing to the fact that in the deployment site fog is infrequent in summer. The restricted importance of this result was also supported by the fact that it had the biggest standard deviation. Another interesting phenomenon that can be noticed from Figure 8.5 is that the performances were slightly better with cloudy sky than with clear sky: this could be due to the fact that clouds may act as a sort of waveguide, leading to a smaller signal dispersion. Moreover, it is reasonable to deem that water salinity together with air stratification just above the sea surface surely degraded the transmitted signals. However, throughout the measurement campaign, no suitable measuring instrument for such detrimental phenomenon was available. Therefore, no quantitative correlation with RSSIs and SNRs can be drawn. In addition, salinity was not measured because it can be considered almost constant as $35\,\text{g/L}$, because the sensor node was deployed just above the sea surface. Therefore, it was not possible to derive a correlation with RSSIs.

Figure 8.6 and 8.7 respectively report within their charts RSSIs and SNR mean values and standard deviations in function of temperature, relative humidity and atmospheric pressure in comparison with the overall mean values and standard deviations computed throughout the whole measurement campaign. Despite the trends of RSSI and SNR

mean values with respect to temperature slightly moved away from the overall mean, they showed an interesting behaviour: although the higher the temperature, the stronger the thermal noise effect, RSSIs and SNRs mean values increased with temperature. It is plausible to conclude that such a fact was the result of the superimposition of two effects taking place outdoor: low temperatures usually occur along with adverse meteorological conditions (e.g., moisture and rain) whose detrimental result has a more prominent extent than the beneficial one owing to low temperatures. As a result, RSSIs and SNRs tend to diminish in such situations. Hence, a similar phenomenon is likely to occur during winter were temperatures are much lower and weather is harsher. Moreover, RSSIs and SNRs were prone to decrease as relative humidity increases, respectively in the order of $2.0 - 3.0$ dB for RSSI and $1.00 - 2.00$ dB for SNR. This is foreseeable since the higher the relative humidity, the denser water vapour in air. This fact was confirmed during field tests even though a modest spike at maximum relative humidity was experienced: it had a little statistical relevance since a limited number of samples for maximum relative humidity were collected. Finally, atmospheric pressure played a minor role since on the whole no significant performances variation can be noticed, apart from a slight decline for low pressure values.

8.1.2 Offshore VSU

8.1.2.1 System Description

Offshore sea farms need to rely on surveillance systems to contrast undesired phenomena like fish poaching as well as breeding cages damages. Therefore, an autonomous remote VSU for offshore sea farms was developed. The system was designed to include off-the-shelf components, and in order to be energy efficient since it was powered via an energy harvesting system (i.e., two photovoltaic panels and a backup battery). Eventually, the system was installed on a cage floating structure, so to take pictures on a hourly basis, and transmitting them ashore by relying on LoRaWAN connectivity.

The block diagram of the VSU is depicted in Figure 8.8, and it was composed of 3 main building blocks (i.e., power supply, control and communications, and camera).

The power supply block, which was only composed of off-the-shelf components, contained 2 photovoltaic panels providing 20 W each, whose task was both to power up the whole system and to recharge a 12 V, 25 Ah lead-acid backup battery through a solar charge controller. The core of the power supply system was the solar charge controller. It was responsible for correctly powering up the control and communications block and the camera in function of both the battery charge level and the power coming from the

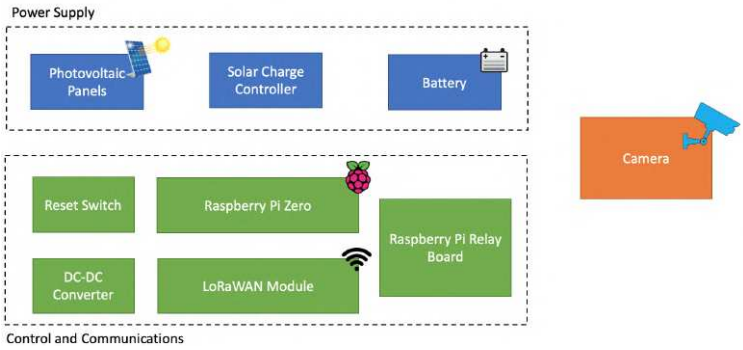

Figure 8.8: VSU block scheme.

photovoltaic panels. Indeed, whenever they were exposed to enough sunlight, the solar charge controller managed the harvested energy for running the whole system as well as for recharging the backup battery. On the contrary, whenever the harvested energy was scant (e.g., during the night), the solar charge controller drew energy from the battery so to supply the system. Photovoltaic panels were fundamental for the long-term functioning of the system. Indeed, such a prototype was offshore installed, and it was supposed to operate for at least a 6-month timespan, while the mere backup battery only ensured a 48-hour autonomy.

The control and communications block was the core of the system since it managed the duty cycling of the camera along with images capturing and transmitting towards a remote server, while minimising power consumption by the activation of the inner elements only for the minimum amount of time needed. Such a working flow was obtained by the following off-the-shelf components:

- DC-DC converter, which filtered out the power supply coming from the appropriate building block so to correctly power each of the system elements;
- Raspberry Pi Zero, which was the control unit of the system due to Python scripts managing both the camera and the duty cycling of all of the other components;
- Raspberry Pi relays board, which contained relay switches that were directly controlled by the Raspberry Pi so to turn on and off the camera and the other system elements whenever they were needed and only for the strictly necessary time in order to limit the overall power consumption;
- LoRaWAN transceiver (i.e., the RFM95 from HopeRF), which provided images

transmission towards the ashore gateway forwarding the information to a remote cloud system by relying to the LoRaWAN network prototype of Figure 3.5;

- Reset switch, which performed a daily hardware reset of the whole system acting as a sort of long-term watchdog timer so to overcome software issues or unexpected behaviours.

The camera was an off-the-shelf outdoor IP one produced by Hikvision, which was especially designed to resist to marine environments. All the elements composing the control and communications block were housed within an IP56 box, while the complete system was mounted on a support pole (see Figure 8.9) which was offshore installed on a breeding cage floating structure (see Figure 8.10).

Figure 8.9: Realisation of the VSU: photovoltaic panels (left) and pole with camera and IP56 box containing the electronics (right).

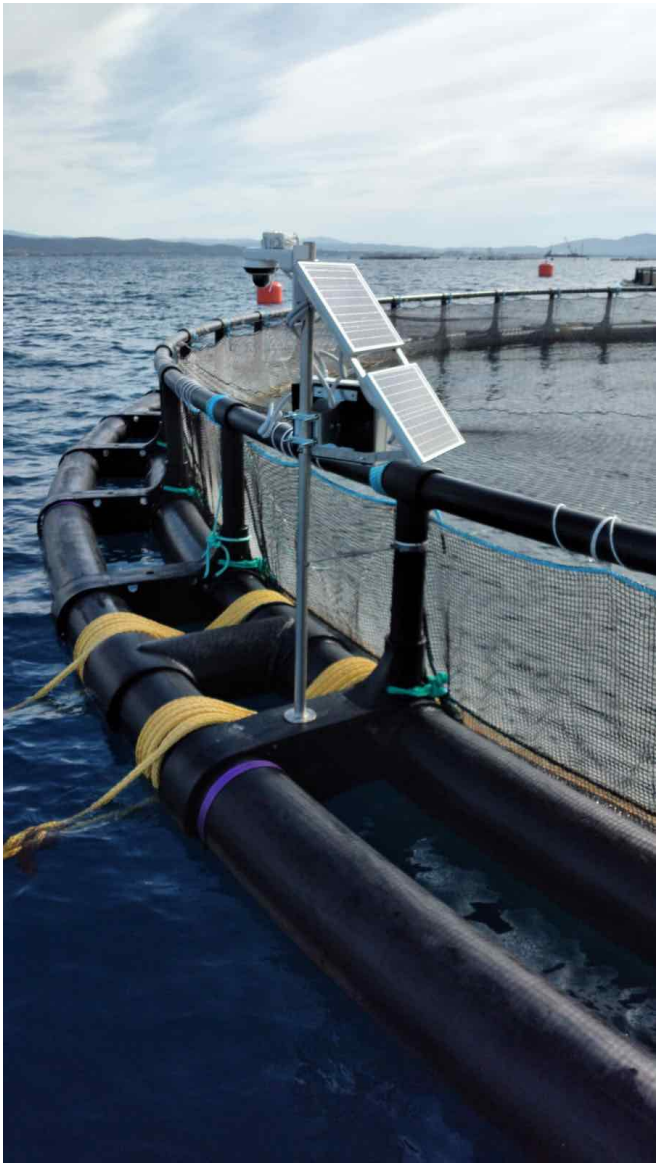

Figure 8.10: VSU prototype offshore installed on a cage floating structure.

8.1.2.2 LoRaWAN Transmission Parameters Selection for Image Transmission

Images require a pre-processing phase to be efficiently sent via LoRaWAN due to the constraints related to regional regulation (i.e., data-rate and duty-cycling concerning temporal occupancy of ISM bands). Indeed, if no pre-processing would be applied, then images could be still successfully broadcast, but in such a way it would take a massive amount of time. The latter is strictly related with the ToA of a LoRaWAN packet. In particular, the packet may be roughly dived into two building blocks: the preamble and the payload. The former requires a time T_p to be sent, while the latter requires the time T_P, therefore

$$ToA = T_p + T_P. \tag{8.1}$$

For a LoRaWAN packet T_p can be evaluated as

$$T_p = 12.25\frac{2^{SF}}{BW} \tag{8.2}$$

where SF is the SF and BW is the bandwidth exploited for the transmission, while T_P is

$$T_P = \left\{8 + max\left(\left\lceil\frac{8PL - 4SF + 44}{4(SF - 2DE)}\right\rceil\left(c_r + 4\right), 0\right)\right\}\frac{2^{SF}}{BW} \tag{8.3}$$

where PL is the number of payload bytes, $c_r \in \{1, 2, 3, 4\}$ respectively expresses the CR of $4/5$, $4/6$, $4/7$ and $4/8$ that is exploited for the Forward Error Correction (FEC) technique at the receiver side for LoRaWAN transmissions, and DE is either equal to 1 if the low data-rate optimisation is enabled or equal to 0 otherwise. The latter parameter is enabled by default whenever LoRaWAN transmissions take place exploiting $BW = 125$ kHz and SF≥ 11, alternatively it is not. Therefore, increasing the SF means augmenting the ToA and, similarly, decreasing the bandwidth and simultaneously increasing c_r results in a slow transmission. For what concerns PL, its maximum value depends on the SF: it ranges from 51 B when SF$= 12$, up to 242 B when SF$= 7$.

In order to assess which transmission parameters allow a reasonable trade-off amid a short ToA and a reduced overall number of packets to be broadcast given that an image necessarily requires more than a single uplink to be sent, due to the fact that its size will be surely greater than 242 B, the following reasoning can be made. LoRaWAN rules for Europe only account for $BW = 125$ kHz and $BW = 250$ kHz for uplinks. However, while the former can be exploited for all SFs, the latter can be solely used for SF$= 7$. Thus, so to decrease the number of involved variables within the problem, suppose to select $BW = 125$ kHz even if it does not provide the minimum ToA. For the same purpose, presume to choose the minimum c_r. Then, assume to transmit packets having the

(a) (b)

Figure 8.11: Image compression algorithms comparison: (a) WebP, (b) JPEG.

maximum PL so to reduce the number of total uplinks to send an image. Therefore, the only left parameter to tune is the SF. If SF= 7 and $PL = 242$ B, then $ToA = 399.62$ ms thus entailing one uplink every 40 s due to the duty-cycling policy. Conversely, if SF= 12 and $PL = 51$ B, then $ToA = 2793.47$ ms thus entailing one uplink every 4 min and 39 s due to the duty-cycling policy. Thus, it is evident that with the same amount of data to transmit (e.g., an image), the best transmission parameters in order to limit latency are SF= 7, $BW = 125\,kHz$ and $c_r = 1$. Moreover, the effectiveness of such parameters was validated for the application scenario in Section 3.

8.1.2.3 Image Capturing, Processing and Transmission

Image pre-processing techniques were kept as simple as possible with the aim of reducing computational burden. Their goal was to reduce image dimension in B, so to decrease the needed number of uplinks for its transmission, while maintaining an acceptable image definition due to the fact that such photos could be exploited for surveillance purposes. In particular, suppose the image coming from the camera had a certain size in pixel, say (x_1, y_1), and that it was a colour one digitalised as RGB without alpha channel. Such image will require an amount of memory in B of $S_1 = 3x_1y_1$ (e.g., a 4K digital picture having size of 4096×2160 may occupy up to 26.5 MB). Sending it as it is would take a huge amount of time. Hence, the straightforward method to speed up the whole process was to firstly resize the image while preserving proportion, and then to compress it while limiting quality losses. Resizing ratio and compression algorithm, along with the relative parameters, may be selected according to system requirements and operation scenario

at hand. However, classic compressed formats like Joint Photographic Experts Group (JPEG) did not suit well since several artefacts spawn whenever high compression factors are exploited. Moreover, if additional size reduction was necessary, the resized image can be brought to greyscale, but a significant quality loss would be experienced. In light of this, WebP compression algorithm was selected since it is an outstanding trade-off between size and quality. Such fact is perceivable by looking at Figure 8.11: it shows the same picture that underwent the same resize process. However, Figure 8.11a was compressed via WebP, while Figure 8.11b was compressed via JPEG, and both the figures occupy 3 kB. The quality of WebP picture was overwhelming since it contained almost no artefact while preserving colours, in contrast with the JPEG one which was in greyscale and heavily affected by artefacts. Therefore, Figure 8.11a may be easily employed for surveillance purposes, unlike Figure 8.11b which was hardly exploitable for the same scope.

After resizing and compression, the image should be encoded prior transmission. A viable alternative is to exploit base64 encoding. Subsequently, the resulting string was divided in several portions that will be the LoRaWAN packets payload whose length was the one selected and discussed earlier on. A header was attached to each of the payloads whose purpose was to mark the packet number at hand as well as the total one in which the image was sent. Such a method was adopted to ease image reconstruction at the LoRaWAN cloud back-end infrastructure. Moreover, a tail was attached to the last payload in which the relative picture shoot timestamp was encoded.

LoRaWAN packets were received by the gateway which forwarded them to the remote LoRaWAN cloud back-end infrastructure. At such stage, the payloads were stored within a database and then the image encoded within the base64 string was reconstructed by resorting to the payloads headers. Finally, the base64 string was decoded in the relative image that was afterwards displayed to users within a web interface.

The VSU was tested in laboratory so to assess the feasibility of the system, especially for what concerns image transmission over LoRaWAN.

8.1.2.4 Preliminary Testbed #1 - Passage of a Person

The simplest testbed is the one in which a person passes in front of the camera. The VSU took a picture (see Figure 8.12a) which occupied 3.1 MB, the relative compressed image occupied 2.9 kB which was then encoded in a base64 string occupying 3.817 kB. Afterwards, the string was sent via LoRaWAN in 17 packets taking 10 min and 50 s. Finally, the image was reconstructed at the LoRaWAN back-end level resulting in Figure 8.12b.

(a) (b)

Figure 8.12: Testbed #1 frames: (a) high quality, (b) compressed and reconstructed at receiver side.

8.1.2.5 Preliminary Testbed #2 - Passage of Two People

The second testbed consisted in two people passing in front of the camera. Once again, the VSU took the relative frames (see Figure 8.13a) which occupied 3 MB, the associated compressed image occupied 2.6 kB which was then encoded in a base64 string occupying 3.477 kB. Subsequently, the string was sent via LoRaWAN in 15 packets taking 9 min and 50 s. Finally, the image was reconstructed at the LoRaWAN back-end level resulting in Figure 8.13b.

(a) (b)

Figure 8.13: Testbed #2 frames: (a) high quality, (b) compressed and reconstructed at receiver side.

8.1.2.6 Results

Preliminary tests results are listed in Table 8.4. At a first glance, the fact that for a given image the relative encoding in the base64 string was averagely one third bigger than the associated frame compressed in WebP can be noticed: this shortcoming is endogenous to base64 encoding algorithm.

Table 8.4: Preliminary tests results for image transmission over LoRaWAN.

	Testbed	
	#1	**#2**
High Quality Frame Size [MB]	3.1	3.0
Resized and Compressed Frame Size [kB]	2.9	2.6
Base64 String Size [kB]	3.817	3.477
# LoRaWAN Packets	17	15
Transmission Time [min:s]	10:50	9:50

A remark on the captured images can be drawn. Albeit the frame was resized and compressed in order to reduce as much as possible latency due to LoRaWAN transmission, the quality of the received image largely suffices for video surveillance purposes. Indeed, by making reference to the pictures (i.e., the taken ones and the received ones), and by examining them side by side, no flaws extensively hindering them were present. Eventually, latency due to LoRaWAN links may be improved by refining VSU image compressing and encoding techniques. Indeed, these times may be surely diminished but not dramatically reduced (e.g., decimated) due to the duty-cycling policy the LoRaWAN protocol accounts for. Nonetheless, the most outstanding result was the capability of employing LoRaWAN protocol to transmit images, albeit it was not devised for such a purpose.

8.2 VWC Effect on LoRaWAN UG2AG Links

The measurement of soil moisture is a key task in a large number of applications in the context of precision agriculture. In fact, autonomous crops watering is included in most of precision agriculture systems, where information concerning to soil moisture is one of the main drivers for the activation of irrigation systems. Despite the wide availability

Figure 8.14: Plastic case with sand that was exploited for laboratory tests on the effect of VWC on LoRaWAN UG2AG links.

of sensors in the market, an accurate measurement or estimation of VWC in soil is still a challenging task which requires expensive devices. Indeed, low cost sensors can be easily found, but they are in practice so raw that are mainly used to distinguish between dry and wet soils. While the latter information may suffice for watering plants in small gardens, it is not enough accurate for precision agriculture applications instead, where water usage needs to be optimised so to improve the overall system efficiency. Indeed, intensive crops may span over thousands of square kms, thus requiring pervasive WUSNs for their remote monitoring. Therefore, VWC can be measured by making use of an augmented sensor, based on Machine Learning (ML), having as input two types of data: the RSSIs related to UG2AG LoRaWAN links; and the low cost, low precision resistive soil moisture sensor raw readings. However, a preliminary study for assessing the effect of VWC on LoRaWAN UG2AG links is needed and presented below.

8.2.1 Test Setup

The aim of this laboratory measurement campaign was to assess losses due to the impact of soil moisture on UG2AG LoRaWAN links. Therefore, the prototype of the LoRaWAN

network infrastructure of Figure 3.5 was exploited. In order to control the experiments and to reduce the number of involved variables within them, trials were sorted out in laboratory. In particular, a plastic case was filled with sand within which an IoUT sensor node was buried (see Figure 8.14).

The IoUT sensor node embedded a microcontroller (i.e., an ATtiny84 produced by Microchip) and a LoRaWAN transceiver (i.e., an RFM95 manufactured by HopeRF) connected to a $\lambda/8$ whip antenna having 2 dBi gain. Such antenna was chosen in view of the results on the antennas selection tests of Section 4. Power supply was provided by a 3600 mAh Li-ion battery supplying 3.7 V: for the sake of convenience, it was placed outside the plastic case and connected to the IoUT sensor node via two cables passing through an IP56 box housing all of the remainder components of the node. The microcontroller executed a firmware implementing a LoRaWAN end device broadcasting packets to a gateway by making use of a frequency diversity paradigm exploiting the 8 different channels in the $863 - 870$ MHz ISM band, and by exploiting the minimum SF (i.e., SF$=7$) and a bandwidth of 125 kHz. Packets payload, having a 16 B-length, only contained a test string.

The plastic case internally measured $55\,\text{cm} \times 40\,\text{cm} \times 30\,\text{cm}$ thus holding up a volume of $66000\,\text{cm}^3$ (which corresponds to 66 L) that was completely filled with sand. The box housing the IoUT node was placed in such a way the antenna was located in the centre of the volume occupied by the sand. In doing so, it had 11 cm of sand above and 11 cm underneath it. At the same time, it was 20 cm-distant from both the lateral sides of the case and 13 cm-distant from both the front and rear sides of the case. From the sedimentological point of view, the soil within the case was entirely sandy (i.e., it had a sand percentage of 100 %) and it had a BD of $1.711\,\text{g/cm}^3$. Once again, regarding SG, this was not measured since standard values can be retrieved in the literature [84]: for sandy soils SG can be chosen as 2.66.

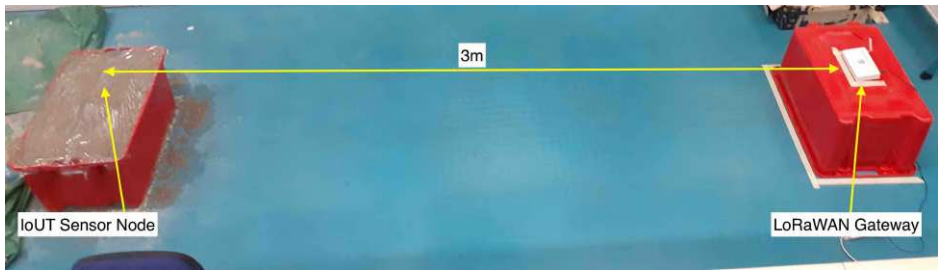

Figure 8.15: Testing setup showing the IoUT sensor node buried in sand within the plastic case and the LoRaWAN gateway.

The IoUT sensor node and the LoRaWAN gateway were 3.00 m apart (see Figure 8.15) to minimise losses that were not caused by soil attenuation. The gateway was the LG308 produced by Dragino, that was connected to a $\lambda/8$ whip antenna having 2 dBi gain, as the one of the sensor node. It behaved as a packet forwarder: at first, it received and demodulated LoRaWAN packets, and simultaneously measured the associated RSSIs; then, it transmitted such data to a remote network server by making use of MQTT protocol.

Experimental tests were carried out according to the following methodology. Several measurement sets were performed, each consisting of three batches during which the IoUT sensor node sent 1000 LoRaWAN packets, and at the same time, RSSIs were recorded. Such choice was selected to average measurements from the three batches of a single set in order to even out undesired disruptive phenomena that were extraneous to soil effects (e.g., fast fading effects). Firstly, the IoUT sensor node underwent a set of measurements, without being buried, 3.00 m apart from the gateway: this set was identified as the control one. Indeed, since these tests only focused on losses due to soil moisture, an effective way to measure them was by following an indirect approach: for each set, losses are equal to the difference amid the RSSIs of the control set and the ones of set at hand. The second set was performed by burying the IoUT sensor node (as it was previously described) within dry sand: thus, this set is characterized by 0 % VWC. From the third set on, the sand was thouroughly watered so to gradually increase VWC with a granularity of 5 %: this was accomplished by pouring 3.3 L of water into the sand and covering the case with clingfilm so to prevent water from evaporation. Then, 15 minutes were awaited before starting with the first batch of transmissions belonging to the measurement set at hand, so to allow water to be equally imbibed by the sand. In so doing, VWC values from 0 % to 20 % were tested. Greater VWCs were not tested since the plastic case reached its maximum capacity. Eventually, with the purpose of speed up the tests, a sandy soil was chosen since sand is able to quickly absorb water while maintaining itself soaked. Finally, Table 8.5 summarises the test settings.

Table 8.5: Summary of the settings related to the field measurement campaign for LoRaWAN IoUT sensor node exploited to assess the effect of VWC on RSSI. A 'None' value for VWC marks the transmissions in which the sensor node was not buried, while a 0 % VWC marks the transmissions in which the sensor node was buried in dry sand.

Transmission Technology	$\mathbf{P}_{TX}$	**SF**	**CR**	**Payload**	**# Packets**	**VWC**
LoRaWAN	14 dBm	7	$4/5$	16 B	3 batches of 1000 packets per VWC value	None, 0 %, 5 %, 10 % 15 %, 20 %

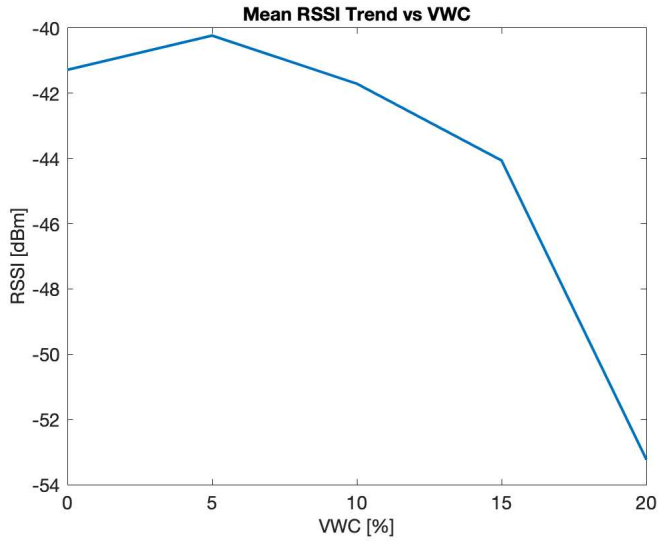

Figure 8.16: Mean RSSI trend for different values of VWC.

8.2.2 Test Results

Figure 8.16 shows the RSSI values during the five measurement sets, in turn for $0\,\%$, $5\,\%$, $10\,\%$, $15\,\%$ and $20\,\%$ VWC, while Table 8.6 reports relative data. Despite a slight increase of RSSI was recorded (i.e., $1.0\,\text{dB}$) at VWC of $5\,\%$ with respect to dry sand, other values were consistent with the well-known detrimental effect of moisture. This could be due to exogenous origins: for instance, the laboratory hosting the tests was inside a building including other research laboratories, therefore it was immersed within a lot of electromagnetic fields coming from the latter ones. In addition, owing to the limited number of transmitted packets, it is highly likely that such phenomenon would be avoided if many more packets were sent. However, this would have been entailed a massive amount of time to be spent for the tests. Moreover, ISM bands are unlicensed ones thus they are intrinsically characterized by noise sources.

Owing to the fact that tests were arranged so to exclusively evaluate soil related losses in dependence on moisture, the only terms of Equation 4.1 to be accounted for are L_{UG}, L_{UG-AG} and $L_{Surface}$ which are respectively computed resorting to Equations 4.2, 4.20 and 4.21. Indeed, within Section 4.1 the model, and the two alternatives for computing the

Table 8.6: RSSI mean values for each measurements set

VWC [%]	0	5	10	15	20
RSSI [dBm]	-41.3	-40.2	-41.7	-44.1	-53.2

real and imaginary part of the effective soil permittivity, were introduced by accounting for the whole link length just for the sake of completeness. Figure 8.17 displays measured losses from experimental data along with loss estimates resulting from the aforesaid methods: MBSDM and ITU. Similarly, Table 8.7 tallies the relative data. Of course, measured soil losses followed the same trend of recorded RSSIs, albeit they exhibited a different tendency with respect to both the methods. In most of the cases, though to a lesser extent, the model was prone to overestimate losses regardless of the exploited method for evaluating soil permittivity constants. Specifically, MBSDM method overvalued losses from a minimum of 0.6 dB at 15 % VWC to a maximum of 0.7 dB at 10 % VWC, while ITU exceeded losses from a minimum of 3.4 dB at 15 % VWC to a maximum of 4.7 dB at 5 % VWC. Conversely, for dry sand and at 20 % VWC both the procedures underrated losses: in the former case, 4.3 dB and 1.4 dB respectively for MBSDM and ITU; while in the latter case, 6.5 dB and 5.0 dB in turn for MBSDM and ITU. Such an odd outcome could be ascribed by the fact that the IoUT sensor node was buried within a sandy soil contained within a plastic case rather than within a whole field. Unfortunately, though, if tests were sorted out that way, it would be barely unfeasible to obtain controlled VWC values. Nevertheless, apart from a minor loss decrease at VWC 5 % in comparison with dry sand, measured losses were consistent with estimates thus remarking both the adverse impact of soil moisture on UG2AG links and the reliability of the path loss model even though, averagely, evaluating complex effective soil permittivity via MBSDM turned out to be an accurate solution.

These preliminary results showed the relationship between RSSI and VWC, thus hinting at the potential feasibility of an augmented sensor for VWC. It relies on ML and Artificial Intelligence (AI) algorithms taking as input the RSSIs so to infer VWC. Moreover, if the IoUT sensor node is equipped with a low cost, low precision resistive soil moisture sensor, then the augmented sensor will be finer, providing more accurate VWC estimates. Indeed, this approach would counteract drawbacks of VWC direct measurement (i.e., expensive probes) that impede the deployment of a pervasive measurement infrastructure, because the involved hardware is low cost, while measurement accuracy is

Table 8.7: Comparison between mean measured soil losses and soil estimates for each measurements set

VWC [%]	Losses [dB]			Relative Difference [%]	
	Experimental Data	MBSDM	ITU	MBSDM	ITU
0	7.9	3.7	6.5	116.4	22.5
5	6.9	6.5	11.6	6.2	−40.8
10	8.3	9.0	13.0	−7.8	−36.1
15	10.7	11.3	14.0	−5.7	−24.0
20	19.8	13.4	14.9	48.3	33.5

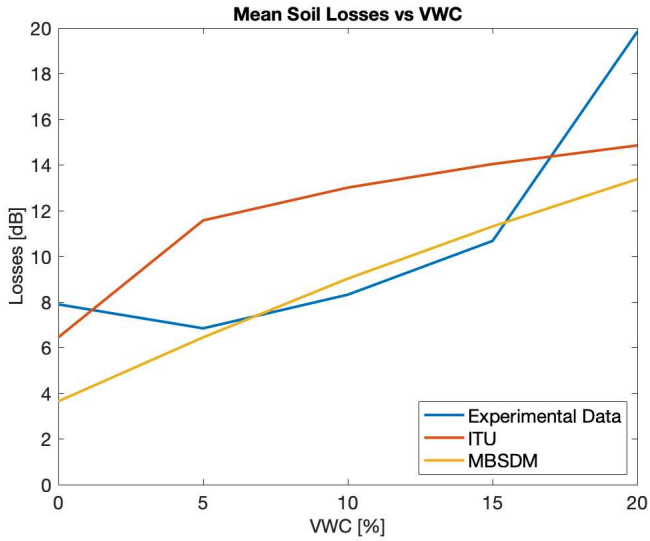

Figure 8.17: Mean soil losses for different values of VWC along with loss estimates coming from the models of Section 4.1.

given by the ML and AI models implementing the augmented sensor. However, and in light of the preliminary results, such approach will be included in future works.

Chapter 9

Conclusions

This Thesis proposed a comparative analysis of IoT transmission technologies enabling distributed measurement systems deployed in critical environments.

Some critical environments were firstly presented, along with providing the relative theoretical analysis modelling path loss in such conditions, and secondly two IoT measurement infrastructures deployed in as many critical contexts were shown. It must be stressed that this Thesis intended neither at finding better path loss models with respect to the existing ones, nor at improving them. Indeed, such models were exploited just to provide estimates of losses in order to better grasp their extent in the considered scenarios, as well as to compare them with measurements coming from field tests. In particular, this is the scientific contribution of the Thesis, since at the moment the literature lacks of such comparative analysis. The most frequent result, that repeatedly occurred throughout the measurement campaigns, is that analytical path loss models should be only considered as a qualitative reference, since they are prone to provide estimates deviating from field measurements. Specifically, the harsher the medium to model, the more significant the discrepancies between loss estimates and measurements. Indeed, whenever the propagation occurs in free space conditions, the associated path loss model provided consistent estimates, meaning that their deviation from measurements was limited. Nonetheless, within the tests taking place above-the-sea, loss estimates and measurements were not concordant owing to the fact that the clearance of the first Fresnel zone was far from being sufficient, thus hindering the assumptions on free space. Such discrepancies were more evident for media like the underground, the underwater, and metallic shields because the associated models do not take into account several parameters helping in better modelling the propagation. A feasible alternative may be to devise empirical path loss models, thus proposing proper fitting curves. However, such approach falls outside the scope of this Thesis, apart from the fact it is particularly time consuming because of the multitude of parameters to account for in order to obtain accurate path loss models. Moreover, it strictly depends on the application scenario at hand, thus being hardly repeatable.

The first application scenario was the marine one, by considering above-the-sea wireless links. Then, the underground and the underwater cases were introduced by

respectively taking into account for UG2AG and UW2AW links. Subsequently, through-metal links were analysed, modelling those circumstances in which a wireless sensor node is housed within a metallic case. Lastly, various harsh environmental conditions typical of IIoT applications (i.e., vibrating machineries, harsh temperature and humidity, and corrosive gaseous atmospheres) were covered. In each of the aforementioned scenarios, field tests were sorted out to validate the performances of wireless measurement systems, in order to show their feasibility in such settings. Finally, two IoT measurement infrastructures in turn deployed above-the-sea and underground were presented thus providing real applications effectively running for a long-term timespan. The former gave the possibility of setting up a LoRaWAN network infrastructure for the remote monitoring of offshore sea farming plants, including the capabilities of performing offshore environmental monitoring along with remote video surveillance. On the other hand, the latter paved the way for the realisation of a system for measuring VWC by relying on RSSIs of UG2AG LoRaWAN links within a context of precision agriculture.

Firstly, a quick overview of the most adopted IoT transmission technologies that can enable wireless measurement systems is given. The bulk of the tests carried out in critical environments were sorted out by making use of LoRaWAN and NB-IoT, in order to compare the most adopted standards belonging to non-cellular and cellular technologies, respectively. Then, the general methodology for performance measurement was presented. Indeed, it was adopted throughout all of the tests. Specifically, performances in terms of RSSIs, SNRs and PLs were assessed by resorting to gateways. Despite these are not proper measuring instruments, they were preferred to spectrum analysers since in wireless measurement systems, deployed in the field, gateways are actually employed. To validate this assumption, a laboratory comparison between a gateway and a spectrum analyser was carried out showing that they provide similar RSSI measurements, thus validating the choice of gateways for field tests. Moreover, since in field tests wireless packets having payload accounting for different lengths were transmitted, a laboratory test assessing the effect of payload length on RSSI was carried out, showing that their correlation is not significant.

The first harsh environment taken into account was the one related to wireless links taking place above-the-sea. After the presentation of a path loss model (i.e., free space path loss model), and of an analysis related to the Earth curvature and the first Fresnel zone clearance, two short-term measurement campaigns were sorted out. Throughout the two measurement campaigns LoRaWAN links over a distance of 8.33 km were tested. Such tests accounted for all the SFs, and for the transmitting and receiving antennas installed at a limited height above-the-sea level to test a worst case scenario. Test results proved the robustness of the modulation, and of the system architecture in general, although

performances were worse than expected because of the limited clearance of the first Fresnel zone (i.e., no more than 20 %) owing to the Earth curvature undermining the LoS assumption.

Underground measurement systems are intrinsically deployed in a harsh environment, therefore UG2AG links were studied. Suitable path loss model were shown, by presenting two methods for evaluating the real and imaginary part of the effective soil permittivity, which are parameters, along with VWC, playing a key role in signal attenuation owing to soil. A preliminary laboratory measurement campaign was carried out, whose aim was to find out the most suitable transmitting antenna (among the available ones) to be employed in such context (and in all those contexts in which sensor nodes require to be housed within protective boxes), along with validating the viability of LoRaWAN and NB-IoT UG2AG links testing several burial depths. The most valuable result was that the links feasibility was validated, although loss measurements were inconsistent with estimates coming from theoretical models owing to the complexity related to the modelling phase of soil attenuating properties. Then, a more detailed measurement campaign testing LoRaWAN UG2AG links in the field was carried out. In particular, three types of soils were considered, modelled and analysed from the point of view of composition and VWC, and several burial depths were tested. Once again, inconsistencies between loss measurements and loss estimates were experienced owing to the same motivations, in spite of the more accurate analyses of the three soil samples, highlighting the complexity of the problems. Nonetheless, the feasibility for both LoRaWAN and NB-IoT infrastructures was proven.

Similarly, UW2AW links were assessed by following an analogous procedure. Appropriate path loss models were presented, by showing two approaches for assessing the real and imaginary part of the effective water permittivity, which are parameters, along with salinity, that are fundamental for attenuating wireless transmissions underwater. Then, a comparative measurement campaign assessing LoRaWAN and NB-IoT UW2AW links was carried out. It underlined the robustness of both the technologies supporting their usage in underwater settings. Moreover, loss measurements and estimates were quite diverging when the effective water permittivity was estimated by resorting to the methods issued by the ITU, while they were more consistent when Debye method was exploited. However, this has not to be considered as a strong result since this measurement campaign was not fully extensive.

Through-metal links represent another instance of wireless transmissions subject to critical contexts. Also for this setup two path loss models were presented. Specifically, one was devised for ideal shields (therefore its assumptions can be hardly met in real application scenarios), and one was devised for shields with apertures (which are the

most diffused in real setups). Then, two measurement campaigns were sorted out. The former compared LoRaWAN, Sigfox and ASK technologies in through-metal links exploiting a decommissioned container. The latter compared LoRaWAN and NB-IoT in through-metal links by making use of a metallic case with apertures. Tests in the container have to be considered as preliminary, and they showed that LoRaWAN protocol definitely outperformed both Sigfox and ASK. Tests in the metallic enclosure proved the effectiveness of both LoRaWAN and NB-IoT for such type of wireless links, but they also underlined the inconsistency between loss measurements and loss estimates provided by the theoretical model. This result was far from being unexpected since, as it was previously stated, the loss model is not rigorous and neglects many variables related to the spatial arrangement of the apertures in the shield surfaces. However, it was nonetheless taken into account since no better models were available.

Industrial environments can be considered as harsh by definition. To this end, the performances of LoRaWAN links in such contexts were investigated. In particular, three testing setups were considered: harsh temperatures and humidity values, corrosive gaseous atmospheres, and vibrating systems. For each of them, performances were assessed by varying the transmitter power output (i.e., specifically by testing -80 dBm, 0 dBm and 14 dBm). The robustness and the effectiveness of the communication protocol was validated in all of the testing setups. Moreover, the detrimental effect of high temperatures and humidity values was confirmed. Then, the exposure to corrosive gaseous atmospheres showed that the performance drop due to such environment is relatively limited, and it can be compared to other disruptive causes which are likely to happen in whichever wireless link. Finally, from tests accounting for vibrations it can be drawn that no significant correlation between RSSI degradation and vibration can be found. However, vibrations do affect RSSI on the whole since a decrease can be perceived with respect to the absence of movement.

Finally, two IoT measurement infrastructures deployed in critical environments were shown. The first harsh environment is the offshore (i.e., 8.33 km distant from the coast), in which a LoRaWAN network infrastructure for the remote monitoring of offshore sea farming plants was set up. It accounted for a sensor node on a seamark buoy, and an offshore VSU installed on the floating breeding cages. The sensor node sampled environmental parameters and broadcast such data offshore via LoRaWAN uplinks. The system was tested for a 70-day timespan, during which the whole system was fully validated. Moreover, this test also aimed at investigating transmission performances variations in function of meteorological parameters (i.e., temperature, humidity, and weather conditions). Tests results proved that weather affects transmission performances: rainy conditions tend to degrade the received signals with respect to clear sky; perfor-

mances were slightly better with cloudy sky than with clear sky owing to the fact that clouds may act as a sort of waveguide, leading to a smaller signal dispersion. On the other hand, the offshore VSU took pictures on a hourly basis. Then, it compressed the pictures and sent them ashore via LoRaWAN packets, proving that the protocol can be exploited for transmitting such type of data (i.e., the one for which it was not designed for). Conversely, an IoUT sensor node was designed and exploited for a laboratory test aiming at finding correlations between RSSI of UG2AG LoRaWAN links and VWC. Such dependence was confirmed, paving the way for a methodology for the gathering of a dataset to be employed for augmented sensing techniques enabling the estimation of VWC without resorting to expensive sensors. In doing so, system like this can be employed in peculiar application scenarios like precision agriculture, in which a low cost pervasive measurement infrastructure can be set up.

The results stemming from this Thesis highlighted the feasibility of the deployment of distributed measurement infrastructures, enabled by suitable IoT transmission technologies, in sundry critical environments. However, they should be considered as the starting point for future works aiming at developing more complex measurement systems in such contexts, meaning that some of the aforementioned scenarios could require finer analysis prior to the system deployment. Nonetheless, since the results of the Thesis can be viewed as a lower bound if a conservative approach is followed, they are at the same time more than promising for future works.

Bibliography

[1] Giacomo Peruzzi and Alessandro Pozzebon. “A review of energy harvesting techniques for Low Power Wide Area Networks (LPWANs)”. In: *Energies* 13.13 (2020), p. 3433.

[2] Alessandro Mecocci, Giacomo Peruzzi, Alessandro Pozzebon, and Pietro Vaccarella. “Architecture of a hydroelectrically powered wireless sensor node for underground environmental monitoring”. In: *IET Wireless Sensor Systems* 7.5 (2017), pp. 123–129.

[3] Christos Milarokostas, Dimitris Tsolkas, Nikos Passas, and Lazaros Merakos. “A Comprehensive Study on LPWANs With a Focus on the Potential of LoRa/LoRaWAN Systems”. In: *IEEE Communications Surveys & Tutorials* (2022).

[4] Alessandra Galli, Giada Giorgi, Claudio Narduzzi, Giacomo Peruzzi, Alessandro Pozzebon, and Sarah Tonello. “IoT technologies for Active Ageing: an Overview of the Elderly Dehydration Case”. In: *2022 IEEE International Symposium on Medical Measurements and Applications (MeMeA)*. IEEE. 2022, pp. 1–6.

[5] Ylli Rama and M Alper Özpmar. “A comparison of long-range licensed and unlicensed LPWAN technologies according to their geolocation services and commercial opportunities”. In: *2018 18th Mediterranean Microwave Symposium (MMS)*. IEEE. 2018, pp. 398–403.

[6] Seung-Hoon Hwang and Shu-Zhi Liu. “Survey on 3GPP low power wide area technologies and its application”. In: *2019 IEEE VTS Asia Pacific Wireless Communications Symposium (APWCS)*. IEEE. 2019, pp. 1–5.

[7] *Bell, Huawei and BeWhere bring new Internet of Things solution to Ontario winery*. http://www.bce.ca/news-and-media/releases/show/Bell-Huawei-and-BeWhere-bring-new-Internet-of-Things-solution-to-Ontario-winery-1. Accessed: October 2022.

[8] Paul Gäbel, Christian Koller, and Elke Hertig. *Development of air quality boxes based on low-cost sensor technology*. Tech. rep. Copernicus Meetings, 2022.

[9] Tao Zhou, Cheng Tao, Sana Salous, Liu Liu, and Zhenhui Tan. "Implementation of an LTE-based channel measurement method for high-speed railway scenarios". In: *IEEE Transactions on Instrumentation and Measurement* 65.1 (2015), pp. 25–36.

[10] Yuya Minami, Akira Idoue, and Eiji Utsunomiya. "Wave Height Measurement Systems Extended a Personal Ocean Observation Buoy". In: *Global Oceans 2020: Singapore–US Gulf Coast*. IEEE. 2020, pp. 1–6.

[11] Emmanuel Migabo, Karim Djouani, and Anish Kurien. "A modelling approach for the narrowband IoT (NB-IoT) physical (PHY) layer performance". In: *IECON 2018-44th Annual Conference of the IEEE Industrial Electronics Society*. IEEE. 2018, pp. 5207–5214.

[12] Y-P Eric Wang, Xingqin Lin, Ansuman Adhikary, Asbjorn Grovlen, Yutao Sui, Yufei Blankenship, Johan Bergman, and Hazhir S Razaghi. "A primer on 3GPP narrowband Internet of Things". In: *IEEE communications magazine* 55.3 (2017), pp. 117–123.

[13] Kishor Krishnan Nair, Adnan M Abu-Mahfouz, and Samuel Lefophane. "Analysis of the narrow band internet of things (NB-IoT) technology". In: *2019 conference on information communications technology and society (ICTAS)*. IEEE. 2019, pp. 1–6.

[14] Stefano Parrino, Giacomo Peruzzi, and Alessandro Pozzebon. "LoPATraN: Low Power Asset Tracking by Means of Narrow Band IoT (NB-IoT) Technology". In: *Sensors* 21.11 (2021), p. 3772.

[15] German Castellanos, Margot Deruyck, Luc Martens, and Wout Joseph. "System assessment of WUSN using NB-IoT UAV-aided networks in potato crops". In: *IEEE Access* 8 (2020), pp. 56823–56836.

[16] Zhou Yan and Hu Gang. "Design of intelligent water metering system for agricultural water based on nb-iot". In: *2019 IEEE 3rd Advanced Information Management, Communicates, Electronic and Automation Control Conference (IMCEC)*. IEEE. 2019, pp. 1665–1669.

[17] Dao-Jiun Wang, Yong-Yi Fanjiang, Chi-Huang Hung, and Yao-Yun Hsiao. “A Low-Cost Brine Level Measurement System for Farmers Through NB-IoT Technology”. In: *2022 IEEE International Conference on Consumer Electronics (ICCE)*. IEEE. 2022, pp. 1–2.

[18] Dong Chen, Nengcheng Chen, Xiang Zhang, Hongliang Ma, and Zeqiang Chen. “Next-Generation Soil Moisture Sensor Web: High-Density In Situ Observation Over NB-IoT”. In: *IEEE Internet of Things Journal* 8.17 (2021), pp. 13367–13383.

[19] Yong Xiao, Marwan Krunz, and Tao Shu. “Multi-operator network sharing for massive IoT”. In: *IEEE Communications Magazine* 57.4 (2019), pp. 96–101.

[20] Kristina Josifović, Stefan Boljević, Vukan Ninković, and Natan Turćinović. “Simulating massive IoT environmental monitoring scenario using OMNeT++”. In: *2019 27th Telecommunications Forum (TELFOR)*. IEEE. 2019, pp. 1–4.

[21] Kia Wiklundh and Peter Stenumgaard. “EMC challenges for the era of massive Internet of Things”. In: *IEEE Electromagnetic Compatibility Magazine* 8.2 (2019), pp. 65–74.

[22] Gabriele Di Renzone, Ada Fort, Marco Mugnaini, Stefano Parrino, Giacomo Peruzzi, and Alessandro Pozzebon. “Interoperability among sub-GHz technologies for metallic assets tracking and monitoring”. In: *2020 IEEE International Workshop on Metrology for Industry 4.0 & IoT*. IEEE. 2020, pp. 131–136.

[23] Laura Joris, François Dupont, Philippe Laurent, Pierre Bellier, Serguei Stoukatch, and Jean-Michel Redouté. “An autonomous sigfox wireless sensor node for environmental monitoring”. In: *IEEE Sensors Letters* 3.7 (2019), pp. 01–04.

[24] Pietro Di Gennaro, Domenico Lofú, Daniele Vitanio, Pietro Tedeschi, and Pietro Boccadoro. “WaterS: A Sigfox-compliant prototype for water monitoring”. In: *Internet Technology Letters* 2.1 (2019), e74.

[25] *Weightless*. http://www.weightless.org. Accessed: October 2022.

[26] *Nwave: the future of smart parking*. https://www.nwave.io/parking-technology/. Accessed: October 2022.

[27] *LoRa Alliance*. https://lora-alliance.or. Accessed: October 2022.

[28] *Andreas Spiess YouTube video: " #120 LoRa / LoRaWAN Range World Record Attempt. Will I succeed?"*. https://www.youtube.com/watch?v=adhWIo-7gr4. Accessed: October 2022.

[29] *Ground breaking world record! LoRaWAN packet received at 702 km (436 miles) distance*. https://www.thethingsnetwork.org/article/ground-breaking-world-record-lorawan-packet-received-at-702-km-436-miles-distance. Accessed: October 2022.

[30] Federico Basili, Stefano Parrino, Giacomo Peruzzi, and Alessandro Pozzebon. "IoT Multi-Hop Facilities via LoRa Modulation and LoRa WanProtocol within Thin Linear Networks". In: *2021 IEEE Sensors Applications Symposium (SAS)*. IEEE. 2021, pp. 1–6.

[31] Giacomo Peruzzi and Alessandro Pozzebon. "Combining LoRaWAN and NB-IoT for Edge-to-Cloud Low Power Connectivity Leveraging on Fog Computing". In: *Applied Sciences* 12.3 (2022), p. 1497.

[32] Matteo Cerchecci, Francesco Luti, Alessandro Mecocci, Stefano Parrino, Giacomo Peruzzi, and Alessandro Pozzebon. "A low power IoT sensor node architecture for waste management within smart cities context". In: *Sensors* 18.4 (2018), p. 1282.

[33] Dimitrios Ziouzios and Minas Dasygenis. "A smart bin implementantion using LoRa". In: *2019 4th South-East Europe Design Automation, Computer Engineering, Computer Networks and Social Media Conference (SEEDA-CECNSM)*. IEEE. 2019, pp. 1–4.

[34] David Baldo, Alessandro Mecocci, Stefano Parrino, Giacomo Peruzzi, and Alessandro Pozzebon. "A multi-layer lorawan infrastructure for smart waste management". In: *Sensors* 21.8 (2021), p. 2600.

[35] Gabriele Di Renzone, Stefano Parrino, Giacomo Peruzzi, and Alessandro Pozzebon. "LoRaWAN in motion: Preliminary tests for real time low power data gathering from vehicles". In: *2021 IEEE International Workshop on Metrology for Automotive (MetroAutomotive)*. IEEE. 2021, pp. 232–236.

[36] VA Velvizhi, G Senbagavalli, M Anbarasan, R Aishwarya, I Harini, et al. "Communication Between Two Vehicles Using LoRa". In: *2021 4th International Conference on Computing and Communications Technologies (ICCCT)*. IEEE. 2021, pp. 453–457.

[37] Ada Fort, Giacomo Peruzzi, and Alessandro Pozzebon. "Quasi-Real Time Remote Video Surveillance Unit for LoRaWAN-based Image Transmission". In: *2021 IEEE International Workshop on Metrology for Industry 4.0 & IoT (MetroInd4.0&IoT)*. IEEE. 2021, pp. 588–593.

[38] Chunlei Fan and Qun Ding. “A novel wireless visual sensor network protocol based on LoRa modulation”. In: *International Journal of Distributed Sensor Networks* 14.3 (2018), p. 1550147718765980.

[39] Giacomo Peruzzi, Alessandra Galli, and Alessandro Pozzebon. “A Novel Methodology to Remotely and Early Diagnose Sleep Bruxism by Leveraging on Audio Signals and Embedded Machine Learning”. In: *2022 IEEE International Symposium on Measurements & Networking (M&N)*. IEEE. 2022, pp. 1–6.

[40] Juha Petäjäjärvi, Konstantin Mikhaylov, Rumana Yasmin, Matti Hämäläinen, and Jari Iinatti. “Evaluation of LoRa LPWAN technology for indoor remote health and wellbeing monitoring”. In: *International Journal of Wireless Information Networks* 24.2 (2017), pp. 153–165.

[41] Hayder Tarab. “Real time performance testing of lora-lpwan based environmental monitoring uav system”. PhD thesis. University of Windsor (Canada), 2018.

[42] Nur Aziemah Azmi Ali and Nurul Adilah Abdul Latiff. “Environmental monitoring system based on LoRa technology in island”. In: *2019 IEEE International Conference on Signals and Systems (ICSigSys)*. IEEE. 2019, pp. 160–166.

[43] Sudha Arvind, S Arvind, and Nitya Nalla. “Intelligent Industrial Monitoring Environment for IoT Application Using LoRa-Based Wireless Sensors”. In: *Smart Intelligent Computing and Applications, Volume 2*. Springer, 2022, pp. 295–303.

[44] Quy Lam Hoang, Woo-Sung Jung, Taehyun Yoon, Daeseung Yoo, and Hoon Oh. “A real-time LoRa protocol for industrial monitoring and control systems”. In: *IEEE Access* 8 (2020), pp. 44727–44738.

[45] Danco Davcev, Kosta Mitreski, Stefan Trajkovic, Viktor Nikolovski, and Nikola Koteli. “IoT agriculture system based on LoRaWAN”. In: *2018 14th IEEE International Workshop on Factory Communication Systems (WFCS)*. IEEE. 2018, pp. 1–4.

[46] Antonio Caruso, Stefano Chessa, Soledad Escolar, Jesús Barba, and Juan Carlos López. “Collection of data with drones in precision agriculture: Analytical model and LoRa case study”. In: *IEEE Internet of Things Journal* 8.22 (2021), pp. 16692–16704.

[47] Yao Cheng, Hendra Saputra, Leng Meng Goh, and Yongdong Wu. “Secure smart metering based on LoRa technology”. In: *2018 IEEE 4th International Conference on Identity, Security, and Behavior Analysis (ISBA)*. IEEE. 2018, pp. 1–8.

[48] Anup Marahatta, Yaju Rajbhandari, Ashish Shrestha, Ajay Singh, Anup Thapa, Francisco Gonzalez-Longatt, Petr Korba, and Seokjoo Shin. “Evaluation of a lora mesh network for smart metering in rural locations”. In: *Electronics* 10.6 (2021), p. 751.

[49] *MIoTy Alliance*. https://mioty-alliance.com. Accessed: October 2022.

[50] Alessandra Galli, Claudio Narduzzi, Giacomo Peruzzi, and Alessandro Pozzebon. “Satellite IoT for Monitoring and Tracking of Athletes in Extreme Environments”. In: *2022 IEEE International Workshop on Sport, Technology and Research (STAR)*. IEEE. 2022, pp. 195–199.

[51] Ada Fort, Marco Mugnaini, Giacomo Peruzzi, and Alessandro Pozzebon. “Reliability Analysis of an IoT Satellite Facility for Remote Monitoring and Asset Tracking within Marine Environments”. In: *2022 IEEE International Workshop on Metrology for the Sea; Learning to Measure Sea Health Parameters (MetroSea)*. IEEE. 2022, pp. 138–142.

[52] John S Seybold. *Introduction to RF propagation*. John Wiley & Sons, 2005.

[53] *LoRa Alliance, LoRaWAN 1.0.3 Regional Parameters*. https://lora-alliance.org/sites/default/files/2018-07/lorawan_regional_parameters_v1.0.3reva_0.pdf. Accessed: October 2022.

[54] *Shenzhen Rakwireless Technology Co., Ltd., RAK831 Lora Gateway Datasheet V1.3*. http://docs.rakwireless.com/en/LoRa/RAK831-LoRa-Gateway/Hardware-Specification/RAK831%20Datasheet%20V1.3.pdf. Accessed: October 2022.

[55] Marco Zennaro, Marco Rainone, and Ermanno Pietrosemoli. “Radio link planning made easy with a telegram bot”. In: *International Conference on Smart Objects and Technologies for Social Good*. Springer. 2016, pp. 295–304.

[56] Juha Petajajarvi, Konstantin Mikhaylov, Antti Roivainen, Tuomo Hanninen, and Marko Pettissalo. “On the coverage of LPWANs: range evaluation and channel attenuation model for LoRa technology”. In: *2015 14th international conference on its telecommunications (itst)*. IEEE. 2015, pp. 55–59.

[57] Nikola Jovalekic, Vujo Drndarevic, Ermanno Pietrosemoli, Iain Darby, and Marco Zennaro. “Experimental study of LoRa transmission over seawater”. In: *Sensors* 18.9 (2018), p. 2853.

[58] Agnelo R Silva and Mehmet Can Vuran. “Communication with aboveground devices in wireless underground sensor networks: An empirical study”. In: *2010 IEEE international conference on communications*. IEEE. 2010, pp. 1–6.

[59] XQ Yu, ZL Zhang, and WT Han. “Evaluation of communication in wireless underground sensor networks”. In: *IOP Conference Series: Earth and Environmental Science*. Vol. 69. 1. IOP Publishing. 2017, p. 012083.

[60] Nasir Saeed, Mohamed-Slim Alouini, and Tareq Y Al-Naffouri. “Toward the internet of underground things: A systematic survey”. In: *IEEE Communications Surveys & Tutorials* 21.4 (2019), pp. 3443–3466.

[61] Nasir Saeed, Mohamed-Slim Alouini, and Tareq Y Al-Naffouri. “3d localization for internet of underground things in oil and gas reservoirs”. In: *IEEE Access* 7 (2019), pp. 121769–121780.

[62] Abdul Salam, Mehmet C Vuran, and Suat Irmak. “Towards internet of underground things in smart lighting: A statistical model of wireless underground channel”. In: *2017 IEEE 14th International Conference on Networking, Sensing and Control (ICNSC)*. IEEE. 2017, pp. 574–579.

[63] Hassan Malik, Nils Kandler, Muhammad Mahtab Alam, Ivar Annus, Yannick Le Moullec, and Alar Kuusik. “Evaluation of low power wide area network technologies for smart urban drainage systems”. In: *2018 IEEE International Conference on Environmental Engineering (EE)*. IEEE. 2018, pp. 1–5.

[64] Sokratis Kartakis, Babu D Choudhary, Alexander D Gluhak, Lambros Lambrinos, and Julie A McCann. “Demystifying low-power wide-area communications for city IoT applications”. In: *Proceedings of the Tenth ACM International Workshop on Wireless Network Testbeds, Experimental Evaluation, and Characterization*. 2016, pp. 2–8.

[65] Dan Du, Heng Zhang, Jirg Yang, and Ping Yang. “Propagation characteristics of the underground-to-aboveground communication link about 2.4 GHz and 433MHz radio wave: An empirical study in the pine forest of Guizhou Province”. In: *2017 3rd IEEE International Conference on Computer and Communications (ICCC)*. IEEE. 2017, pp. 1041–1045.

[66] Xin Dong, Mehmet C Vuran, and Suat Irmak. “Autonomous precision agriculture through integration of wireless underground sensor networks with center pivot irrigation systems”. In: *Ad Hoc Networks* 11.7 (2013), pp. 1975–1987.

[67] Abdul Salam and Syed Shah. “Internet of things in smart agriculture: Enabling technologies”. In: *2019 IEEE 5th World Forum on Internet of Things (WF-IoT)*. IEEE. 2019, pp. 692–695.

[68] Marcus Hardie and Donald Hoyle. “Underground wireless data transmission using 433-MHz LoRa for agriculture”. In: *Sensors* 19.19 (2019), p. 4232.

[69] Stefano Parrino, Giacomo Peruzzi, and Alessandro Pozzebon. “Pilot Analysis on Soil Moisture Impact on Underground to Aboveground LoRaWAN Transmissions for IoUT Contexts”. In: *2021 IEEE International Instrumentation and Measurement Technology Conference (I2MTC)*. IEEE. 2021, pp. 1–6.

[70] Xiaoqing Yu, Pute Wu, Zenglin Zhang, Ning Wang, and Wenting Han. “Electromagnetic wave propagation in soil for wireless underground sensor networks”. In: *Progress In Electromagnetics Research M* 30 (2013), pp. 11–23.

[71] Li Li, Na Dong, and Jianya Chen. “EM wave propagation in non-uniform soil”. In: *Information Technology Journal* 12.19 (2013), p. 5011.

[72] Abdul Salam and Mehmet C Vuran. “Impacts of soil type and moisture on the capacity of multi-carrier modulation in internet of underground things”. In: *2016 25th international conference on computer communication and networks (ICCCN)*. IEEE. 2016, pp. 1–9.

[73] Myron C Dobson, Fawwaz T Ulaby, Martti T Hallikainen, and Mohamed A El-Rayes. “Microwave dielectric behavior of wet soil-Part II: Dielectric mixing models”. In: *IEEE Transactions on geoscience and remote sensing* 1 (1985), pp. 35–46.

[74] Abdul Salam, Mehmet C Vuran, and Suat Irmak. “Pulses in the sand: Impulse response analysis of wireless underground channel”. In: *IEEE INFOCOM 2016-The 35th annual IEEE international conference on computer communications*. IEEE. 2016, pp. 1–9.

[75] Ali M Sadeghioon, David N Chapman, Nicole Metje, and Carl J Anthony. “A new approach to estimating the path loss in underground wireless sensor networks”. In: *Journal of Sensor and Actuator Networks* 6.3 (2017), p. 18.

[76] Xin Dong and Mehmet C Vuran. “Impacts of soil moisture on cognitive radio underground networks”. In: *2013 first international black sea conference on communications and networking (BlackSeaCom)*. IEEE. 2013, pp. 222–227.

[77] Xiaoqing Yu, Wenting Han, and Zenglin Zhang. “Path loss estimation for wireless underground sensor network in agricultural application”. In: *Agricultural Research* 6.1 (2017), pp. 97–102.

[78] Mehmet C Vuran and Ian F Akyildiz. “Channel model and analysis for wireless underground sensor networks in soil medium”. In: *Physical communication* 3.4 (2010), pp. 245–254.

[79] ZHI Sun, Ian F Akyildiz, and Gerhard P Hancke. “Dynamic connectivity in wireless underground sensor networks”. In: *IEEE Transactions on Wireless Communications* 10.12 (2011), pp. 4334–4344.

[80] Damien Wohwe Sambo, Anna Förster, Blaise Omer Yenke, and Idrissa Sarr. “A new approach for path loss prediction in wireless underground sensor networks”. In: *2019 IEEE 44th LCN Symposium on Emerging Topics in Networking (LCN Symposium)*. IEEE. 2019, pp. 50–57.

[81] Valery L Mironov, Lyudmila G Kosolapova, and Sergej V Fomin. “Physically and mineralogically based spectroscopic dielectric model for moist soils”. In: *IEEE Transactions on Geoscience and Remote Sensing* 47.7 (2009), pp. 2059–2070.

[82] *International Telecommunication Union (ITU), Electrical characteristics of the surface of the Earth, August 2019*. https://www.itu.int/dms_pubrec/itu-r/rec/p/R-REC-P.527-4-201706-I!!PDF-E.pdf. Accessed: October 2022.

[83] Chester K Wentworth. “A scale of grade and class terms for clastic sediments”. In: *The journal of geology* 30.5 (1922), pp. 377–392.

[84] K Prakash, A Sridharan, HK Thejas, and HM Swaroop. “A simplified approach of determining the specific gravity of soil solids”. In: *Geotechnical and Geological Engineering* 30.4 (2012), pp. 1063–1067.

[85] Robert Louis Folk and William C Ward. “Brazos River bar [Texas]; a study in the significance of grain size parameters”. In: *Journal of sedimentary research* 27.1 (1957), pp. 3–26.

[86] Giovanni Sarti et al. “Magdala harbour sedimentation (Sea of Galilee, Israel), from natural to anthropogenic control”. In: *Quaternary International* 303 (2013), pp. 120–131.

[87] Erich P Stuntebeck, Dario Pompili, and Tommaso Melodia. “Wireless underground sensor networks using commodity terrestrial motes”. In: *2006 2nd IEEE Workshop on Wireless Mesh Networks*. IEEE. 2006, pp. 112–114.

[88] Bui Van Hieu, Seunghwan Choi, Young Uk Kim, Youngsuk Park, and Taikyeong Jeong. “Wireless transmission of acoustic emission signals for real-time monitoring of leakage in underground pipes”. In: *KSCE Journal of Civil Engineering* 15.5 (2011), pp. 805–812.

[89] Bruno Silva, Roy M Fisher, Anuj Kumar, and Gerhard P Hancke. “Experimental link quality characterization of wireless sensor networks for underground monitoring”. In: *IEEE Transactions on Industrial Informatics* 11.5 (2015), pp. 1099–1110.

[90] Idrees Zaman, J Dede, M Gellhaar, Hartmut Koehler, and Anna Foerster. "Molenet: A new sensor node for underground monitoring". In: *IEEE SenseApp* (2016).

[91] Rachel Cardell-Oliver, Christof Hübner, Matthias Leopold, and Jason Beringer. "Dataset: LoRa underground farm sensor network". In: *Proceedings of the 2nd Workshop on Data Acquisition To Analysis*. 2019, pp. 26–28.

[92] Lorenzo Parri, Stefano Parrino, Giacomo Peruzzi, and Alessandro Pozzebon. "Low power wide area networks (LPWAN) at sea: Performance analysis of offshore data transmission by means of LoRaWAN connectivity for marine monitoring applications". In: *Sensors* 19.14 (2019), p. 3239.

[93] Andrew J Wixted, Peter Kinnaird, Hadi Larijani, Alan Tait, Ali Ahmadinia, and Niall Strachan. "Evaluation of LoRa and LoRaWAN for wireless sensor networks". In: *2016 IEEE SENSORS*. IEEE. 2016, pp. 1–3.

[94] Juha Petäjäjärvi, Konstantin Mikhaylov, Marko Pettissalo, Janne Janhunen, and Jari Iinatti. "Performance of a low-power wide-area network based on LoRa technology: Doppler robustness, scalability, and coverage". In: *International Journal of Distributed Sensor Networks* 13.3 (2017), p. 1550147717699412.

[95] Peter J Radcliffe, Karina Gomez Chavez, Paul Beckett, Justin Spangaro, and Conrad Jakob. "Usability of LoRaWAN technology in a central business district". In: *2017 IEEE 85th Vehicular Technology Conference (VTC Spring)*. IEEE. 2017, pp. 1–5.

[96] Neil R Peplinski, Fawwaz T Ulaby, and Myron C Dobson. "Dielectric properties of soils in the 0.3-1.3-GHz range". In: *IEEE transactions on Geoscience and Remote sensing* 33.3 (1995), pp. 803–807.

[97] *MathWorks, earthSurfacePermittivity MATLAB function*. https://www.mathworks.com/help/comm/ref/earthsurfacepermittivity.html. Accessed: October 2022.

[98] Mari Carmen Domingo. "An overview of the internet of underwater things". In: *Journal of Network and Computer Applications* 35.6 (2012), pp. 1879–1890.

[99] Christian Cardia, Petrika Gjanci, Chiara Petrioli, Gabriele Saturni, Daniele Spaccini, and Domenico Tomaselli. "The Internet of Underwater Things: From nemo to underwater whatsapp". In: *Proceedings of the Twentieth ACM International Symposium on Mobile Ad Hoc Networking and Computing*. 2019, pp. 409–410.

[100] Chien-Chi Kao, Yi-Shan Lin, Geng-De Wu, and Chun-Ju Huang. "A comprehensive study on the internet of underwater things: applications, challenges, and channel models". In: *Sensors* 17.7 (2017), p. 1477.

[101] Kaiqiang Lin, Tong Hao, Zhouwei Yu, Wuan Zheng, and Wenchao He. “A preliminary study of UG2AG link quality in LoRa-based wireless underground sensor networks”. In: *2019 IEEE 44th Conference on Local Computer Networks (LCN)*. IEEE. 2019, pp. 51–59.

[102] Kaiqiang Lin, Tong Hao, Wuan Zheng, and Wenchao He. “Analysis of LoRa link quality for underwater wireless sensor networks: A semi-empirical study”. In: *2019 IEEE Asia-Pacific Microwave Conference (APMC)*. IEEE. 2019, pp. 120–122.

[103] Jaime Lloret, Sandra Sendra, Miguel Ardid, and Joel JPC Rodrigues. “Underwater wireless sensor communications in the 2.4 GHz ISM frequency band”. In: *Sensors* 12.4 (2012), pp. 4237–4264.

[104] Gianni Cario, Alessandro Casavola, Petrika Gjanci, Marco Lupia, Chiara Petrioli, and Daniele Spaccini. “Long lasting underwater wireless sensors network for water quality monitoring in fish farms”. In: *OCEANS 2017-Aberdeen*. IEEE. 2017, pp. 1–6.

[105] Giulio Cossu, Alessandro Sturniolo, Alessandro Messa, Simone Grechi, Daniele Costa, Andrea Bartolini, David Scaradozzi, Andrea Caiti, and Ernesto Ciaramella. “Sea-trial of optical ethernet modems for underwater wireless communications”. In: *Journal of Lightwave Technology* 36.23 (2018), pp. 5371–5380.

[106] Hans J Liebe, George A Hufford, and Takeshi Manabe. “A model for the complex permittivity of water at frequencies below 1 THz”. In: *International Journal of Infrared and Millimeter Waves* 12.7 (1991), pp. 659–675.

[107] Pietro Manzoni, Carlos T Calafate, Juan-Carlos Cano, and Enrique Hernández-Orallo. “Indoor vehicles geolocalization using LoRaWAN”. In: *Future Internet* 11.6 (2019), p. 124.

[108] S Mangal and Ketan Rajawat. “Performance evaluation of LoRaWAN with decreasing RSSI values”. In: *Int. J. Appl. Eng. Res.* 14.2 (2019), pp. 177–182.

[109] Che Cameron, Wasif Naeem, and Kang Li. “Functional Qos metric for lorawan applications in challenging industrial environment”. In: *2020 16th IEEE International Conference on Factory Communication Systems (WFCS)*. IEEE. 2020, pp. 1–6.

[110] Srikanth Kavuri, Dmitri Moltchanov, Aleksandr Ometov, Sergey Andreev, and Yevgeni Koucheryavy. “Performance analysis of onshore NB-IoT for container tracking during near-the-shore vessel navigation”. In: *IEEE Internet of Things Journal* 7.4 (2020), pp. 2928–2943.

[111] Sergei Alexander Schelkunoff. “Electromagnetic waves”. In: (1943).

[112] Henry W Ott. *Electromagnetic compatibility engineering*. John Wiley & Sons, 2011.

[113] *STMicrolectronics, STM32L053R8 Datasheet Rev. 9*. https://www.st.com/resource/en/datasheet/stm32l053r8.pdf. Accessed: May 2023.

[114] *Panasonic, NCR18650B Datasheet*. https://www.batteryspace.com/prod-specs/NCR18650B.pdf. Accessed: May 2023.

[115] *Microchip Technology Inc., MCP1700 Datasheet*. https://www.mouser.it/datasheet/2/268/MCP1700_Data_Sheet_20001826F-737536.pdf. Accessed: May 2023.

[116] *Microchip Technology Inc., MCP1702 Datasheet*. https://eu.mouser.com/datasheet/2/268/MCHPS03366_1-2520572.pdf. Accessed: May 2023.

[117] *HopeRF Electronic, RFM95/96/97/98 Datasheet V 1.0*. https://www.mouser.it/datasheet/2/975/1463993415RFM95_96_97_98W-1858106.pdf. Accessed: May 2023.

[118] *STMicrolectronics, S2-LP Datasheet Rev. 11*. https://www.st.com/resource/en/datasheet/s2-lp.pdf. Accessed: May 2023.

[119] *Summitek Technology Co., Ltd., ST-TX01-ASK Datasheet*. https://components101.com / sites / default / files / component _ datasheet / 433 % 20MHz % 20RF % 20Transmitter%20Module_0.pdf. Accessed: May 2023.

[120] Tommaso Addabbo, Ada Fort, Marco Mugnaini, Lorenzo Parri, Stefano Parrino, Alessandro Pozzebon, and Valerio Vignoli. “An IoT framework for the pervasive monitoring of chemical emissions in industrial plants”. In: *2018 Workshop on Metrology for Industry 4.0 and IoT*. IEEE. 2018, pp. 269–273.

[121] Luca Tessaro, Cristiano Raffaldi, Maurizio Rossi, and Davide Brunelli. “LoRa performance in short range industrial applications”. In: *2018 International Symposium on Power Electronics, Electrical Drives, Automation and Motion (SPEEDAM)*. IEEE. 2018, pp. 1089–1094.

[122] Gabriele Di Renzone, Ada Fort, Marco Mugnaini, Alessandro Pozzebon, Valerio Vignoli, and Alessandro Elmi. “Condition monitoring with LoRaWAN: Preliminary tests on gas turbine exciters”. In: *2021 IEEE International Workshop on Metrology for Industry 4.0 & IoT (MetroInd4. 0&IoT)*. IEEE. 2021, pp. 598–603.

[123] Vibhor Kumar, J Akhtar, Kulwant Singh, and Anup Singh Maan. “Simulation based analysis of temperature effect on breakdown voltage of Ion implanted Co/n-Si Schottky diode”. In: (2012).

[124] SM Mitani, MS Alias, MR Yahya, and AFA Mat. "Temperature effect on gain and threshold current of GaInNAs-based 1.3 μm semiconductor laser". In: *2009 IEEE International Symposium on Industrial Electronics*. IEEE. 2009, pp. 2208–2211.

[125] Jun-quan Chen, Xing Chen, Chang-Jun Liu, Kama Huang, and Xiao-Bang Xu. "Analysis of temperature effect on pin diode circuits by a multiphysics and circuit cosimulation algorithm". In: *IEEE Transactions on Electron Devices* 59.11 (2012), pp. 3069–3077.

[126] Ziming Zhu, Ai Zhang, Gang Ouyang, and Guowei Yang. "Band gap tunability in semiconductor nanocrystals by strain: size and temperature effect". In: *The Journal of Physical Chemistry C* 115.14 (2011), pp. 6462–6466.

[127] TG Abdullah, SA Sami, and MS Omar. "Temperature dependence of the energy band gap of CuSi2P3 semiconductor using PSOPW method". In: *Materials Science-Poland* 36.4 (2018), pp. 553–562.

[128] Vahid Samavatian, Mahmud Fotuhi-Firuzabad, Payman Dehghanian, and Frede Blaabjerg. "Reliability modeling of multistate degraded power electronic converters with simultaneous exposure to dependent competing failure processes". In: *IEEE Access* 9 (2021), pp. 67096–67108.

[129] Pradeep Lall, Vikas Yadav, and David Locker. "Sustained high-temperature vibration reliability of thermally aged leadfree assemblies in automotive environments". In: *2020 Pan Pacific Microelectronics Symposium (Pan Pacific)*. IEEE. 2020, pp. 1–18.

[130] Jitendra Tahalyani, M Jaleel Akhtar, Jayesh Cherusseri, and Kamal K Kar. "Characteristics of capacitor: fundamental aspects". In: *Handbook of Nanocomposite Supercapacitor Materials I*. Springer, 2020, pp. 1–51.

[131] Tommaso Addabbo, Ada Fort, Roberto Biondi, Stefano Cioncolini, Marco Mugnaini, Santina Rocchi, and Valerio Vignoli. "Measurement of angular vibrations in rotating shafts: Effects of the measurement setup nonidealities". In: *IEEE transactions on Instrumentation and Measurement* 62.3 (2012), pp. 532–543.

[132] Tommaso Addabbo, Ada Fort, Elia Landi, Riccardo Moretti, Marco Mugnaini, Lorenzo Parri, and Valerio Vignoli. "A wearable low-cost measurement system for estimation of human exposure to vibrations". In: *2019 IEEE 5th International forum on Research and Technology for Society and Industry (RTSI)*. IEEE. 2019, pp. 442–446.

[133] Tommaso Addabbo, Ada Fort, Elia Landi, Riccardo Moretti, Marco Mugnaini, Lorenzo Parri, and Valerio Vignoli. “A Characterization system for bearing condition monitoring sensors, a case study with a low power wireless Triaxial MEMS based sensor”. In: *2020 IEEE International Workshop on Metrology for Industry 4.0 & IoT*. IEEE. 2020, pp. 11–15.

[134] Malka N Halgamuge, Jayantha P Liyanage, and Priyan Mendis. “Wireless technologies for integrated e-operations in offshore environments”. In: *Electronic Journal of Structural Engineering* 01 (2010), pp. 100–112.

[135] *OpenWeather*. https://openweathermap.org. Accessed: October 2022.

Publications from the Author

[1] Lorenzo Parri, Stefano Parrino, Giacomo Peruzzi, and Alessandro Pozzebon. "Low power wide area networks (LPWAN) at sea: Performance analysis of offshore data transmission by means of LoRaWAN connectivity for marine monitoring applications". In: *Sensors* 19.14 (2019), p. 3239.

[2] David Baldo, Ada Fort, Marco Mugnaini, Giacomo Peruzzi, Alessandro Pozzebon, and Valerio Vignoli. "Reliability and availability evaluation of an autonomous remote video monitoring system for offshore sea farms". In: *Proceedings of 2020 IMEKO TC-19 International Workshop on Metrology for the Sea*. 2020.

[3] Lorenzo Parri, Stefano Parrino, Giacomo Peruzzi, and Alessandro Pozzebon. "A LoRaWAN network infrastructure for the remote monitoring of offshore sea farms". In: *2020 IEEE International Instrumentation and Measurement Technology Conference (I2MTC)*. IEEE. 2020, pp. 1–6.

[4] Matteo Gineprini, Stefano Parrino, Giacomo Peruzzi, and Alessandro Pozzebon. "LoRaWAN performances for underground to aboveground data transmission". In: *2020 IEEE international instrumentation and measurement technology conference (I2MTC)*. IEEE. 2020, pp. 1–6.

[5] Gabriele Di Renzone, Ada Fort, Marco Mugnaini, Stefano Parrino, Giacomo Peruzzi, and Alessandro Pozzebon. "Interoperability among sub-GHz technologies for metallic assets tracking and monitoring". In: *2020 IEEE International Workshop on Metrology for Industry 4.0 & IoT*. IEEE. 2020, pp. 131–136.

[6] Giacomo Peruzzi and Alessandro Pozzebon. "A review of energy harvesting techniques for Low Power Wide Area Networks (LPWANs)". In: *Energies* 13.13 (2020), p. 3433.

[7] Lorenzo Parri, Stefano Parrino, Giacomo Peruzzi, and Alessandro Pozzebon. "Offshore lorawan networking: Transmission performances analysis under different environmental conditions". In: *IEEE Transactions on Instrumentation and Measurement* 70 (2020), pp. 1–10.

[8] Gabriele Di Renzone, Stefano Parrino, Giacomo Peruzzi, Alessandro Pozzebon, and Duccio Bertoni. "LoRaWAN underground to aboveground data transmission performances for different soil compositions". In: *IEEE Transactions on Instrumentation and Measurement* 70 (2021), pp. 1–13.

[9] David Baldo, Alessandro Mecocci, Stefano Parrino, Giacomo Peruzzi, and Alessandro Pozzebon. "A multi-layer lorawan infrastructure for smart waste management". In: *Sensors* 21.8 (2021), p. 2600.

[10] Antonella Lombardo, Stefano Parrino, Giacomo Peruzzi, and Alessandro Pozzebon. "LoRaWAN versus NB-IoT: Transmission performance analysis within critical environments". In: *IEEE Internet of Things Journal* 9.2 (2021), pp. 1068–1081.

[11] Gabriele Di Renzone, Ada Fort, Marco Mugnaini, Giacomo Peruzzi, Alessandro Pozzebon, and Valerio Vignoli. "LoRaWAN transmission system capability assessment in industrial environment under temperature and humidity characterization". In: *2021 IEEE International Instrumentation and Measurement Technology Conference (I2MTC)*. IEEE. 2021, pp. 1–6.

[12] Stefano Parrino, Giacomo Peruzzi, and Alessandro Pozzebon. "Pilot analysis on soil moisture impact on underground to aboveground lorawan transmissions for iout contexts". In: *2021 IEEE International Instrumentation and Measurement Technology Conference (I2MTC)*. IEEE. 2021, pp. 1–6.

[13] Stefano Parrino, Giacomo Peruzzi, and Alessandro Pozzebon. "Lopatran: Low power asset tracking by means of narrow band iot (nb-iot) technology". In: *Sensors* 21.11 (2021), p. 3772.

[14] Ada Fort, Giacomo Peruzzi, and Alessandro Pozzebon. "Quasi-real time remote video surveillance unit for lorawan-based image transmission". In: *2021 IEEE International Workshop on Metrology for Industry 4.0 & IoT (MetroInd4. 0&IoT)*. IEEE. 2021, pp. 588–593.

[15] Gabriele Di Renzone, Stefano Parrino, Giacomo Peruzzi, and Alessandro Pozzebon. "LoRaWAN in motion: Preliminary tests for real time low power data gathering from vehicles". In: *2021 IEEE International Workshop on Metrology for Automotive (MetroAutomotive)*. IEEE. 2021, pp. 232–236.

[16] Federico Basili, Stefano Parrino, Giacomo Peruzzi, and Alessandro Pozzebon. "Iot multi-hop facilities via lora modulation and lora wanprotocol within thin linear networks". In: *2021 IEEE Sensors Applications Symposium (SAS)*. IEEE. 2021, pp. 1–6.

[17] Gabriele Di Renzone, Elia Landi, Marco Mugnaini, Lorenzo Parri, Giacomo Peruzzi, and Alessandro Pozzebon. "Assessment of LoRaWAN Transmission Systems Under Temperature and Humidity, Gas, and Vibration Aging Effects Within IIoT Contexts". In: *IEEE Transactions on Instrumentation and Measurement* 71 (2021), pp. 1–11.

[18] David Baldo, Gabriele Di Renzone, Ada Fort, Marco Mugnaini, Giacomo Peruzzi, Alessandro Pozzebon, and Valerio Vignoli. "Remote video monitoring for offshore sea farms: Reliability and availability evaluation and image quality assessment via laboratory tests". In: *Acta IMEKO* 10.4 (2021), pp. 17–24.

[19] Giacomo Peruzzi and Alessandro Pozzebon. "Combining lorawan and nb-iot for edge-to-cloud low power connectivity leveraging on fog computing". In: *Applied Sciences* 12.3 (2022), p. 1497.

[20] Alessandra Galli, Giada Giorgi, Claudio Narduzzi, Giacomo Peruzzi, Alessandro Pozzebon, and Sarah Tonello. "IoT technologies for Active Ageing: an Overview of the Elderly Dehydration Case". In: *2022 IEEE International Symposium on Medical Measurements and Applications (MeMeA)*. IEEE. 2022, pp. 1–6.

[21] Matteo Bertocco, Ada Fort, Elia Landi, Marco Mugnaini, Lorenzo Parri, Giacomo Peruzzi, and Alessandro Pozzebon. "Roller Bearing Failures Classification with Low Computational Cost Embedded Machine Learning". In: *2022 IEEE International Workshop on Metrology for Automotive (MetroAutomotive)*. IEEE. 2022, pp. 12–17.

[22] Alessandra Galli, Claudio Narduzzi, Giacomo Peruzzi, and Alessandro Pozzebon. "Satellite IoT for Monitoring and Tracking of Athletes in Extreme Environments". In: *2022 IEEE International Workshop on Sport, Technology and Research (STAR)*. IEEE. 2022, pp. 195–199.

[23] Ada Fort, Elia Landi, Riccardo Moretti, Lorenzo Parri, Giacomo Peruzzi, and Alessandro Pozzebon. "Hand-Arm Vibration Monitoring via Embedded Machine Learning on Low Power Wearable Devices". In: *2022 IEEE International Symposium on Measurements & Networking (M&N)*. IEEE. 2022, pp. 1–6.

[24] Giacomo Peruzzi, Alessandra Galli, and Alessandro Pozzebon. “A Novel Methodology to Remotely and Early Diagnose Sleep Bruxism by Leveraging on Audio Signals and Embedded Machine Learning”. In: *2022 IEEE International Symposium on Measurements & Networking (M&N)*. IEEE. 2022, pp. 1–6.

[25] Irene Cappelli, Federico Carli, Matteo Intravaia, Federico Micheletti, and Giacomo Peruzzi. “A Machine Learning Model for Microcontrollers Enabling Low Power Indoor Positioning Systems via Visible Light Communication”. In: *2022 IEEE International Symposium on Measurements & Networking (M&N)*. IEEE. 2022, pp. 1–6.

[26] Ada Fort, Marco Mugnaini, Giacomo Peruzzi, and Alessandro Pozzebon. “Reliability Analysis of an IoT Satellite Facility for Remote Monitoring and Asset Tracking within Marine Environments”. In: *2022 IEEE International Workshop on Metrology for the Sea; Learning to Measure Sea Health Parameters (MetroSea)*. IEEE. 2022, pp. 138–142.